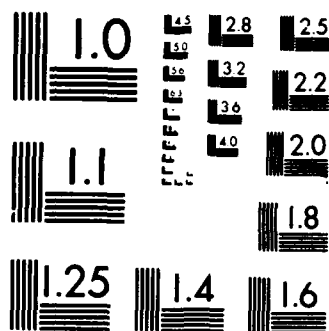


1/2

NL



MICROCOPY RESOLUTION TEST CHART
NATIONAL BUREAU OF STANDARDS 1963 A

AD-A184 986

Advanced Concepts Theory Annual Report 1986

*Plasma Radiation Branch
Plasma Physics Division*

August 12, 1987

This research was sponsored by the Defense Nuclear Agency under Subtask RL RA, work unit 00049, and work unit title "X-Ray Source Development Theory," MIPR No. 86-570.

DTIC
ELECTE
SEP 25 1987
S D
E

Approved for public release; distribution unlimited.

87 9 18 004

SECURITY CLASSIFICATION OF THIS PAGE

AD-1124 186

REPORT DOCUMENTATION PAGE				
1a. REPORT SECURITY CLASSIFICATION UNCLASSIFIED		1b. RESTRICTIVE MARKINGS		
2a. SECURITY CLASSIFICATION AUTHORITY		3. DISTRIBUTION/AVAILABILITY OF REPORT		
2b. DECLASSIFICATION/DOWNGRADING SCHEDULE		Approved for public release; distribution unlimited.		
4. PERFORMING ORGANIZATION REPORT NUMBER(S) NRL Memorandum Report 6051		5. MONITORING ORGANIZATION REPORT NUMBER(S)		
6a. NAME OF PERFORMING ORGANIZATION Naval Research Laboratory	6b. OFFICE SYMBOL (If applicable) Code 4720	7a. NAME OF MONITORING ORGANIZATION Defense Nuclear Agency		
6c. ADDRESS (City, State, and ZIP Code) Washington, DC 20375-5000		7b. ADDRESS (City, State, and ZIP Code) 6801 Telegraph Road Alexandria, VA 22310		
8a. NAME OF FUNDING/SPONSORING ORGANIZATION Defense Nuclear Agency	8b. OFFICE SYMBOL (If applicable) RAEV	9. PROCUREMENT INSTRUMENT IDENTIFICATION NUMBER		
8c. ADDRESS (City, State, and ZIP Code) Alexandria, VA 22310		10. SOURCE OF FUNDING NUMBERS		
		PROGRAM ELEMENT NO. 62715H	PROJECT NO.	TASK NO. WORK UNIT ACCESSION NO. DN880-191
11. TITLE (Include Security Classification) Advanced Concepts Theory Annual Report 1986				
12. PERSONAL AUTHOR(S) Plasma Radiation Branch				
13a. TYPE OF REPORT Annual	13b. TIME COVERED FROM 1/86 TO 12/86	14. DATE OF REPORT (Year, Month, Day) 12 August 1987		15. PAGE COUNT 108
16. SUPPLEMENTARY NOTATION This research was sponsored by the Defense Nuclear Agency under Subtask RL RA, work unit 00049, and work unit title "X-Ray Source Development Theory," MIPR No. 86-570.				
17. COSATI CODES			18. SUBJECT TERMS (Continue on reverse if necessary and identify by block number)	
FIELD	GROUP	SUB-GROUP	Z pinch physics Radiation hydrodynamics Plasma mixtures Gyrokinetic propagation Plasma opening switches	
19. ABSTRACT (Continue on reverse if necessary and identify by block number) ➤ This report details the work of the Plasma Radiation Branch conducted in FY 86 with respect to several critical problems concerning the design of Z pinch implosions and the optimization of their radiative output. Separate sections describe progress in atomic modeling of K shell copper radiation, radiation hydrodynamics, argon implosions, design of anti-zipping nozzles, and analyses of anomalous resistivity and plasma opening switches.				
20. DISTRIBUTION/AVAILABILITY OF ABSTRACT <input checked="" type="checkbox"/> UNCLASSIFIED/UNLIMITED <input type="checkbox"/> SAME AS RPT <input type="checkbox"/> DTIC USERS			21. ABSTRACT SECURITY CLASSIFICATION UNCLASSIFIED	
22a. NAME OF RESPONSIBLE INDIVIDUAL Jack Davis			22b. TELEPHONE (Include Area Code) (202) 767-3278	22c. OFFICE SYMBOL Code 4720

DD FORM 1473, 84 MAR

83 APR edition may be used until exhausted
All other editions are obsolete

SECURITY CLASSIFICATION OF THIS PAGE

CONTENTS

EXECUTIVE SUMMARY	v
A. COPPER ATOMIC MODEL AND APPLICATION TO HARD Z-PINCH X-RAYS	1
B. KRYPTON-TUNGSTEN MIXTURES IN Z-PINCH PLASMA IMPLOSIONS	12
C. K-SHELL YIELD FROM AN ARGON GAS PUFF	21
D. ANTI-ZIPPERING NOZZLE IMPLOSION CHARACTERISTICS AND THEIR IMPORTANCE TO UNIFORMITY IN A Z-PINCH	42
E. OPENING SWITCH AND DIODE MODELING	49
F. APPENDIX — EFFECT OF PULSE SHARPENING ON IMPLODING NEON Z-PINCH PLASMAS	92

Accession For	
NTIS GRA&I	<input checked="" type="checkbox"/>
DTIC TAB	<input checked="" type="checkbox"/>
Unannounced	<input type="checkbox"/>
Justification	
By _____	
Distribution/ _____	
Availability Codes	
Dist	Avail and/or Special
A-1	



Executive Summary

During FY 86 the Plasma Radiation Branch at NRL has focused its resources on several critical problems concerning the design of Z pinches and the fundamental physical processes governing the evolution of their implosions and radiative output. Our 1986 Advanced Concepts Theory Annual Report consists of five self-contained sections, each reporting substantial progress on significant design innovations or Z pinch physics.

The first two of these sections report progress on atomic/hydrodynamic modeling of copper and krypton implosions. Achieving substantial K shell emission with either or both of these high atomic number elements would represent a quantum leap in DNA's simulation capability. The K shell lines in these elements range in energy from 8 to 15 keV. Section A reports on the development of a detailed K shell atomic model for copper ions and the benchmarking of the spectra generated by this theoretical model against published experimental spectra. The temperature-density diagnostics available from the copper K shell spectrum have been identified and in FY 87 will be applied to the copper wire experiments conducted on BLACKJACK 5 at Maxwell Laboratories, Inc.

Section B explores a concept which has appeared frequently in the open Soviet literature and is considered by many Soviet scientists to be an established fact - enhanced compressions of high atomic number plasmas driven by radiative cooling. The idea is that very high densities and hence radiative yields are obtainable by seeding a principal radiating element (krypton gas puff, in our case) with a very effective high atomic number "coolant" (we have chosen tungsten). As the tungsten coolant radiates, the temperature and pressure of the plasma initially remain lower than would be the case with a pure krypton plasma. This permits a greater degree of compression to be achieved, and, ultimately, increases the radiative yield which scales as the square of the density. As the results of Section B demonstrate, the concept appears to be promising and we strongly recommend that DNA invest in additional modeling (in particular improvement of our high Z atomic data base) and some preliminary experiments both with and without high Z coolants included to provide a laboratory test of this yield-enhancing design.

Section C presents detailed one-dimensional self-consistent radiative-hydrodynamic modeling of argon implosions on Gamble-II. It is well known that as the mass injected into a gas puff pinch is increased, the radiative yield at first increases, but reaches a maximum and then falls substantially at high mass loads. The analysis of this section identifies and explains the physics tradeoffs which result in this phenomenon. Even though more kinetic energy can be stored in a lighter mass, there may not be enough radiating ions present to effectively convert this energy. Conversely, at high mass, the smaller kinetic energy which can be imparted to a heavy load prevents high yields from being achieved. When the fields are coupled to the plasma near the time of peak current, full two-dimensional code analysis is required to simulate the formation of the various "hot spots" arising from plasma instabilities. Nevertheless, the 1-D simulations have successfully predicted within experimental limits the mass loading point at which Gamble-II's radiation yields maximize.

One of the most important deleterious effects limiting the peak power achievable by Z pinch implosions is known as "zippering" - the non uniform pinch assembly along the Z axis which spreads the radiation pulse in time. Frequently the total K-shell pulse is nearly an order of magnitude longer than would be the case if the entire length of plasma assembled simultaneously. Section D presents results from hydrodynamic modeling of various nozzle designs intended to counteract the zippering effect by tilting the nozzle to spray the cold gas inward. Results show that certain nozzle designs can result in the simultaneous assembly of a length of 2 cm in the Z direction. The next step in this investigation is the direct simulation of radiative power pulse shapes, using anti-zippering nozzles.

The scaling of radiative yields has been observed to follow approximately the fourth power of peak current (see, for instance, the paper in the Appendix). This implies that a detailed knowledge of plasma resistivity and its effect on current distribution could yield impressive dividends in design of machines and loads to optimize radiation. For instance, a 20% increase in current would boost the yield by a factor of two. Unfortunately, the theory of anomalous resistivity in plasmas is not yet firmly established for Z pinch geometries. However, our gyrokinetic propagation studies (Section E) are providing an increasingly firm base for anomalous resistivity calculations in radiation source plasmas (PRS's) and

in opening switch plasmas (VOS's). In VOS schemes, the power flow in the tenuous magnetized regions will influence the energy transfer efficiency and opening times of the devices.

Simulations of plasma opening switches are confirming the low density, hot electron mode of operation. Mechanisms that produce a wider current channel have been identified. Simple electrostatic diode simulations have proven adequate for treatment of realistic geometries such as ring diodes and a coordinated effort to address design details is proceeding with Maxwell Laboratories.

Finally, the Appendix contains the final version of a paper "Effect of Pulse Sharpening on Imploding Neon Z-Pinch Plasmas" which describes the greater radiating efficiency of Gamble-II when equipped with a plasma erosion opening switch. Some of this material appeared in different form in last year's Advanced Concepts Final Report (NRL Memorandum Report 5759). The published paper is included here for convenient reference.

In addition to the work presented here there have been a number of reports on related activities. They include:

1. NRL Memorandum Report 5765 "Gamble-II Imploding Sodium Plasma. I Calibration of the Heliumlike Resonance Line as a Pump Source and Detection of Fluorescence in Neon", J. Davis, J. E. Rogerson, and J. P. Apruzese, 10 April 1986.
2. NRL Memorandum Report 5771 "Argon Puff Gas Soft X-Ray Laser", J. Davis, J. P. Apruzese, C. Agritellis and P. Kepple, April 1986.
3. NRL Memorandum Report 5776 "Gamble-II Imploding Sodium Plasma. II. Uniformly Filled Z-Pinch", J. Davis, J. E. Rogerson, and J. P. Apruzese, May 1986.
4. NRL Memorandum Report 5871 "A Comparison of Radiation Transport Methods in Axisymmetric Geometries", J. Giuliani, October 1986.
5. "Dynamics of Imploding Neon Gas-Puff Plasmas", R. W. Clark, J. Davis and F. L. Cochran, Phys. of Fluids Vol. 29 (6) p. 1971, June 1986.
6. "X-Ray Lasing in a Na/Ne Plasma Environment", F. L. Cochran, J. Davis and J. P. Apruzese, Journal of Applied Physics 57 p. 27, January 1985.

ADVANCED CONCEPTS THEORY ANNUAL REPORT 1986

Section A. Copper Atomic Model and Application to hard Z-Pinch X-Rays

It has long been considered highly desirable by DNA to obtain a substantial yield of x-rays in the 10 keV region. Copper's chemical and mechanical properties facilitate target fabrication and it is, therefore, an excellent choice of material for exploratory experiments aimed at producing copious K-shell radiation. We have studied the ionization to the K-shell in copper and the resulting high energy radiation as a function of radius, density and temperature for cylindrical geometries using a collisional radiative equilibrium (CRE) model. A simple K-shell copper model, which has been benchmarked against experiment¹, is used to analyze the feasibility of employing copper in Z-pinchs to produce significant amounts of K-shell radiation.

I. MODEL DESCRIPTION

Since we consider copper plasmas of only such temperatures and densities that the K-shell dominates the ionic species, we employ a multistate, multilevel model which includes

¹ The krypton rates were downscaled to copper using a computer code, which has since been modified so that the atomic rates from any element can be hydrogenically downscaled to those of any other element. This means that rate tables (covering the K-shell region) can be constructed fairly quickly for different elements.

This code will be a valuable tool for DNA in analyzing the feasibility of different elements, or combination of elements, as plasma sources for Z-pinchs.

Manuscript approved March 11, 1987

excited levels through principal quantum number $n=5$ for lithiumlike, heliumlike, and hydrogenlike copper in addition to all thirty ground states (neutral through fully stripped). For lithiumlike Cu XXVII, the six excited states included are: $1s^2 2p^2 P$, $1s^2 3s^2 S$, $1s^2 3p^2 P$, $1s^2 3d^2 D$, $n=4$ doublet, and $n=5$ doublet. For heliumlike Cu XXVIII, there are eight excited states: $1s2s^3 S$, $1s2s^1 S$, $1s2p^3 P$, $1s2p^1 P$, the consolidated $n=3$ triplet states, the consolidated $n=3$ singlet states, and the consolidated $n=4$ and $n=5$ levels. Finally, for hydrogenlike Cu XXIX there are four excited states: the $n=2, 3, 4$ and 5 levels, with the sublevels treated as statistically populated.

The copper rates were obtained by hydrogenically downscaling krypton transition rates.¹ The krypton rates themselves, however, were not calculated hydrogenically. For details of the krypton model, the reader may consult Ref. 2 which describes an argon model similar to the krypton model used here. The atomic processes populating and depopulating the levels are: collisional ionization, collisional and radiative recombination, collisional excitation and deexcitation, dielectronic recombination and spontaneous radiative decay.

The rate equations are solved in the steady-state approximation for a homogeneous plasma of constant ion density and uniform temperature. An iterative technique³ is used to obtain self-consistency between the fractional level populations and the radiation field. To account for opacity effects, a detailed frequency grid spanning the region of interest (8 to 11 keV) has been formed by combining fine grids centered on each line in the region. From 8 to 11 keV, radiation is then transported at each grid point; outside of this region, individual lines are transported probabilistically⁴.

The cylindrical geometry considered here is a 1 mm diameter, 3 cm long cylindrical plasma whose temperature and ion density are varied. (Note that the total number of ions is not constant in this case.) This geometry constitutes an approximation of Z-pinch plasmas. In the cylindrical runs, the ion and electron densities are low enough that line shapes can be described adequately by Voigt profiles.

II. COMPARISON WITH EXPERIMENT

Yaakobi and Burek¹ have published a spectrum obtained by imploding a thin copper shell. They imploded a $0.3\text{ }\mu\text{m}$ thick copper shell of diameter $80\text{ }\mu\text{m}$, obtaining the time-integrated spectrum shown in Fig. 1. There was film saturation, so that the He α line is actually more intense than it appears to be. We modeled the plasma conditions by assuming that the spectrum was obtained primarily at peak compression and that, at that time, the plasma was homogeneous, containing a total of 5.14×10^{14} copper ions. By varying the temperature and ion density (equivalent to sphere diameter at peak compression) we obtained a best fit, Fig. 2, for a temperature of 1.3 keV and ion density of $3.64 \times 10^{22}\text{ cm}^{-3}$ (or $30\text{ }\mu\text{m}$ diameter). Since doubly excited levels have not been included in the atomic model, not all of the lines that appear in the experimental spectrum show up in Fig. 2. According to our calculations, at 4 keV, or even at 2 keV, the hydrogenlike Ly α line at 8.727 keV is much too intense to agree with the experimental spectrum. Indeed, at 4 keV the He α and Ly α are of comparable intensity, whereas in Fig. 1, the Ly α line has barely registered.

III. RESULTS

In the cylindrical case, spectra, fractional populations and He α line power outputs were calculated for a 1 mm diameter, 3 cm long homogeneous plasma at various temperatures and densities. The densities assumed in this geometry are around $2 \times 10^{19}\text{ cm}^{-3}$, considerably less than typically reached in a spherical implosion. As a consequence there is less collisional excitation. This means that there will be fewer ions in the excited heliumlike levels, and since these excited levels can be ionized to produce the hydrogenlike ions⁵, there will be fewer hydrogenlike ions. Figures 3 through 6 are theoretical spectra for temperatures of 1.5, 2, 4, and 6 keV, respectively.

Figure 7 displays hydrogenlike and heliumlike copper fractions as a function of temperature for the plasma cylinder described above at ion densities ranging from 2×10^{19} to $5 \times 10^{19} \text{ cm}^{-3}$. An important facet of Fig. 7 is that while heliumlike copper is produced in substantial abundance (45%) at a plasma temperature of 2 keV, the hydrogenlike copper does not appear at even the 10% level until 4.5 keV. Therefore, there will be a regime in which only the heliumlike lines are observed. The relative ease in producing the heliumlike stage relative to the hydrogenlike stage is a straight forward consequence of the ionization potentials. It requires 2.6 keV to ionize a lithiumlike copper ion to heliumlike; but to ionize a heliumlike copper ion to the hydrogenlike stage requires 11 keV.

This phenomenon is reflected in line power outputs. Even at a temperature of 4 keV, the hydrogenlike line power is about an order of magnitude below the heliumlike line output. We have fit the K-shell power output in J/nsec to the following scaling law, good to 10% for temperatures between 1.5 and 3.5 keV, and good to 28% for temperatures up to 5 keV:

$$P(n_i, T) = 130 n_i^2 \exp[-12/T^2] \quad \text{J/nsec},$$

where n_i is the total copper ion density in units of $1 \times 10^{19} \text{ cm}^{-3}$, T is the temperature in keV, and we have assumed a 3 cm long copper plasma of diameter 1 mm. At an ion density of $2 \times 10^{19} \text{ cm}^{-3}$, assuming a 15 ns radiating pulse, a copper K-shell yield of 1 kJ would be attained at a plasma temperature of 2.5 keV.

Figure 8 shows the total power output due to hydrogenlike, heliumlike, and lithiumlike ions for 1 cm long cylinders containing 10 and 100 μg of copper at 2 keV. At large radii the power output follows the $1/r^2$ law. As the radius decreases and the density increases, systematic variations in the ionization stages (here between lithiumlike and berylliumlike ions) cause the power output to fall below the $1/r^2$ line. A more complete model, containing excited levels of beryllium, would follow the $1/r^2$ line for smaller radii more closely.

IV. CONCLUSION

A K-shell copper model has been used to examine the ionization and spectral output of Z-pinchs in the 8-10 keV region. For the densities considered here, it is not until about 7 keV that the hydrogenlike population is half that of the heliumlike fractional population. This means that for temperatures less than 7 keV, there will be only very weak hydrogenlike lines. A large fraction of the ions tend to remain in the heliumlike ground state even at high temperatures, causing the He α power output at line center to be very intense. Yields of a kilojoule are obtainable at temperatures of 2.5 keV. The relative intensities of the hydrogenlike, heliumlike, and any inner shell lines present will provide valuable clues to the conditions achieved in the forthcoming copper wire experiments at Maxwell Laboratories.

References

- ¹ B. Yaakobi and A. J. Burek, IEEE J. Quantum Electron, QE-19, 1841 (1983).
- ² A. Hauer, K. G. Whitney, P. C. Kepple, and J. Davis, Phys. Rev. A 28, 963 (1983).
- ³ J. P. Apruzese, J. Davis, D. Duston, and R. W. Clark, Phys. Rev. A 29, 246 (1984).
- ⁴ J. P. Apruzese, J. Quant Spectrosc. Radiat. Transfer 34, 447 (1985).
- ⁵ J. P. Apruzese and J. Davis, Phys. Rev. A 31, 2976 (1985)

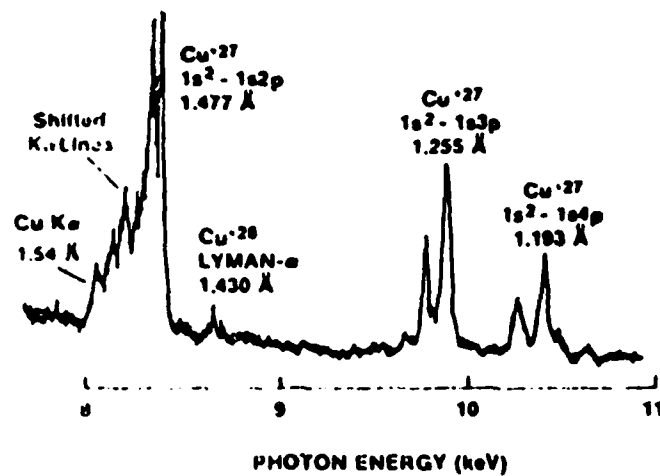


FIG. 1. Experimental copper spectrum obtained by Yaakobi and Burek (Ref. 1) by the laser-driven implosion of a 0.3 μm thick copper shell of initial diameter 80 μm .

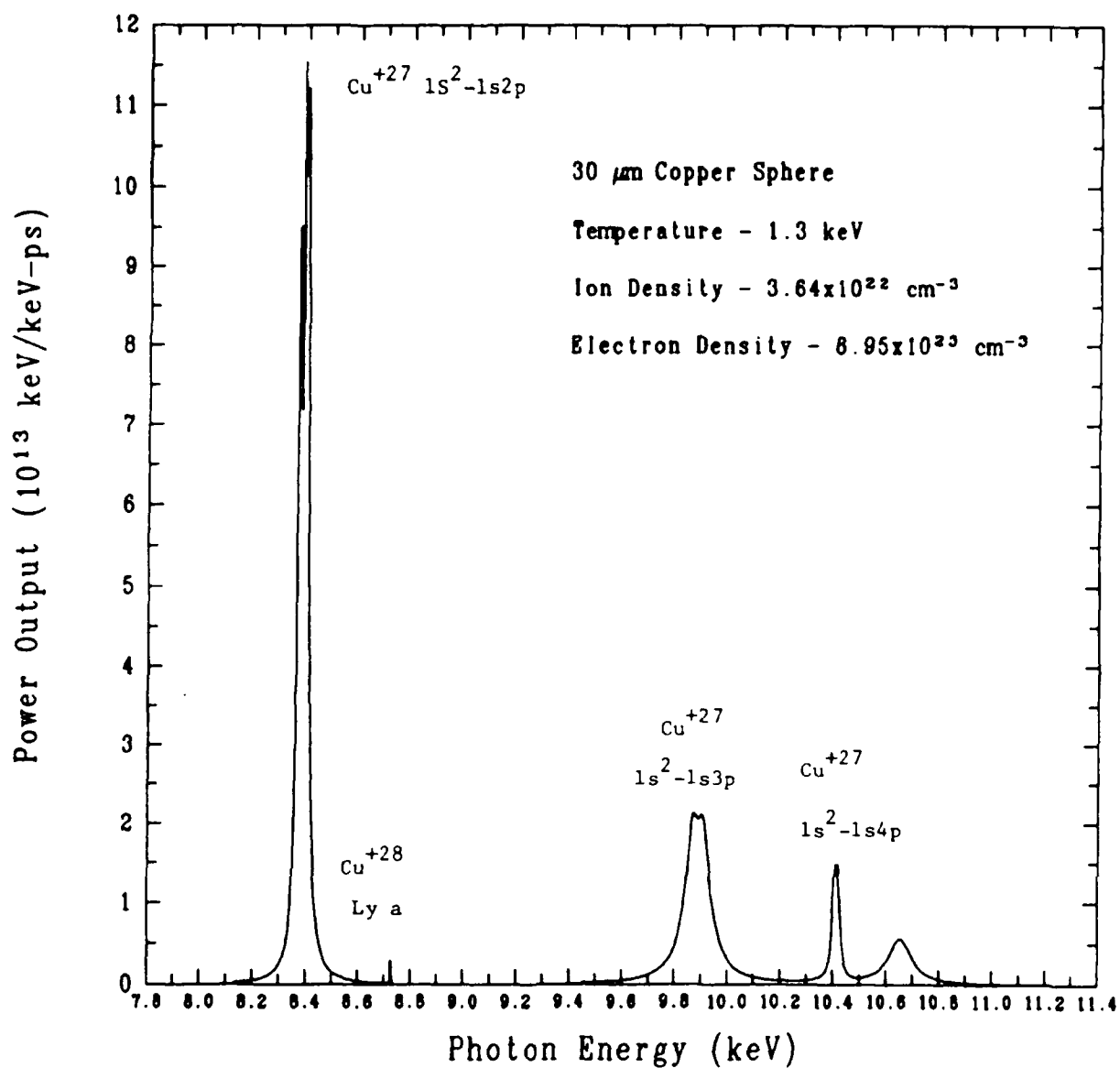


FIG. 2. Copper spectrum obtained with collisional-radiative-equilibrium plasma model at a temperature of 1.3 keV and diameter of 30 μm (ion density is $3.64 \times 10^{22} \text{ cm}^{-3}$). The total number of copper ions is equal to that employed in the experiment of Fig. 1.

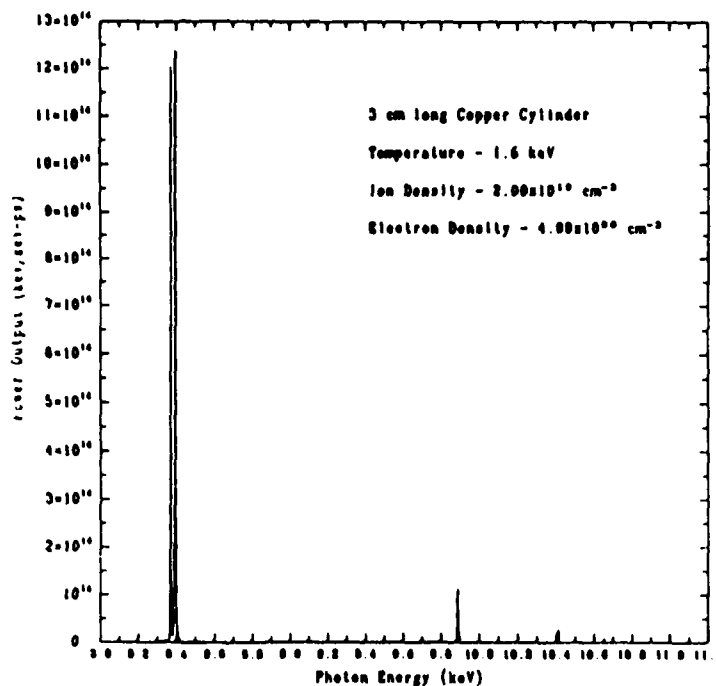


FIG. 3. Copper spectrum obtained with collisional-radiative-equilibrium plasma model for a 3 cm long, 1mm diameter cylinder at a temperature of 1.5 keV and ion density of $2 \times 10^{19} \text{ cm}^{-3}$. (Electron density is $4.99 \times 10^{20} \text{ cm}^{-3}$).

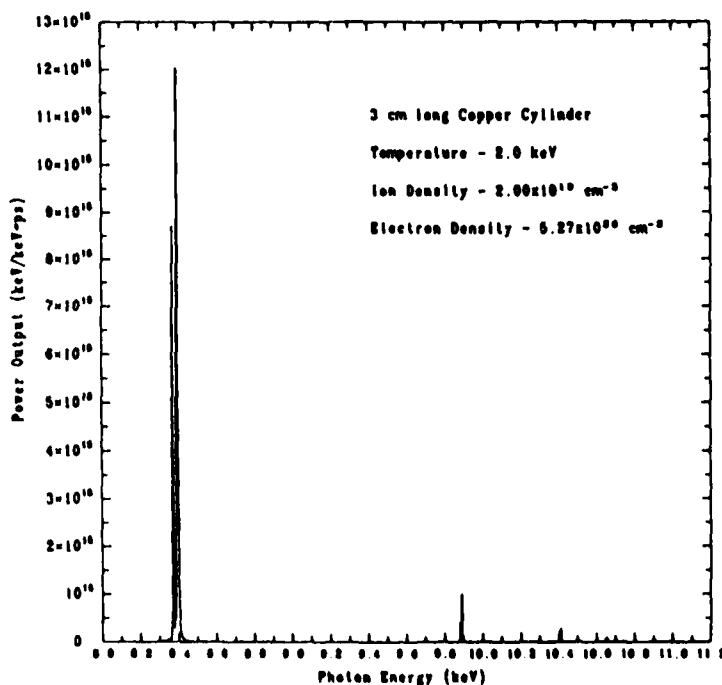


FIG. 4. Same as Fig. 3, except the temperature is 2 keV. (Electron density is $5.27 \times 10^{20} \text{ cm}^{-3}$).

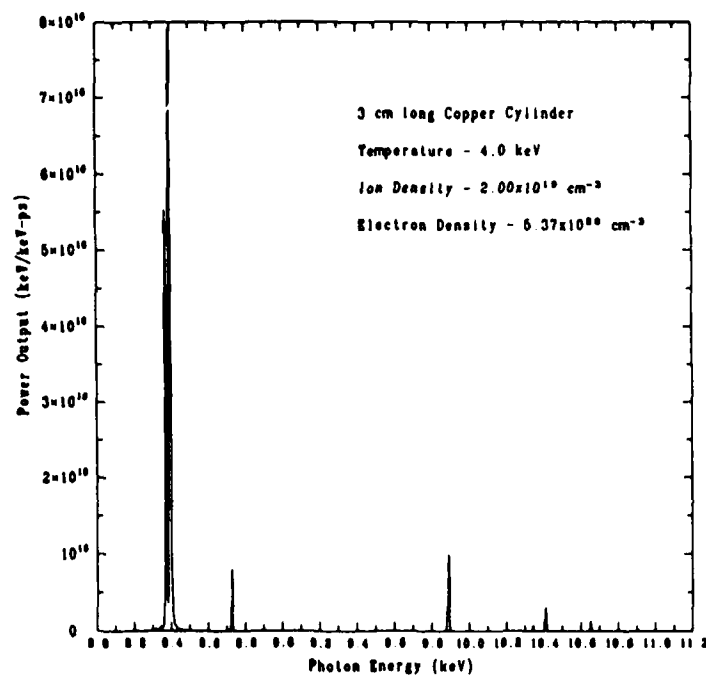


FIG. 5. Same as Fig. 3, except the temperature is 4 keV. (Electron density is $5.37 \times 10^{20} \text{ cm}^{-3}$).

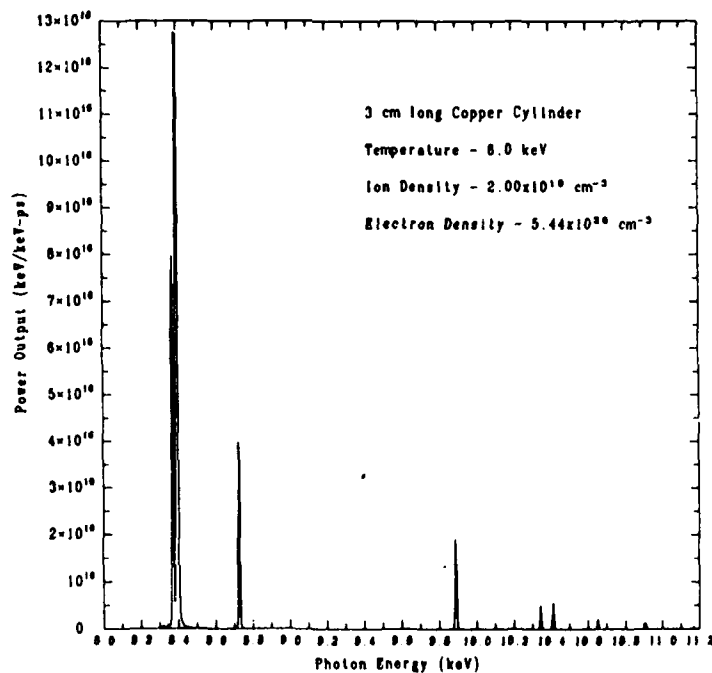


FIG. 6. Same as Fig. 3, except the temperature is 6 keV. (Electron density is $5.44 \times 10^{20} \text{ cm}^{-3}$).

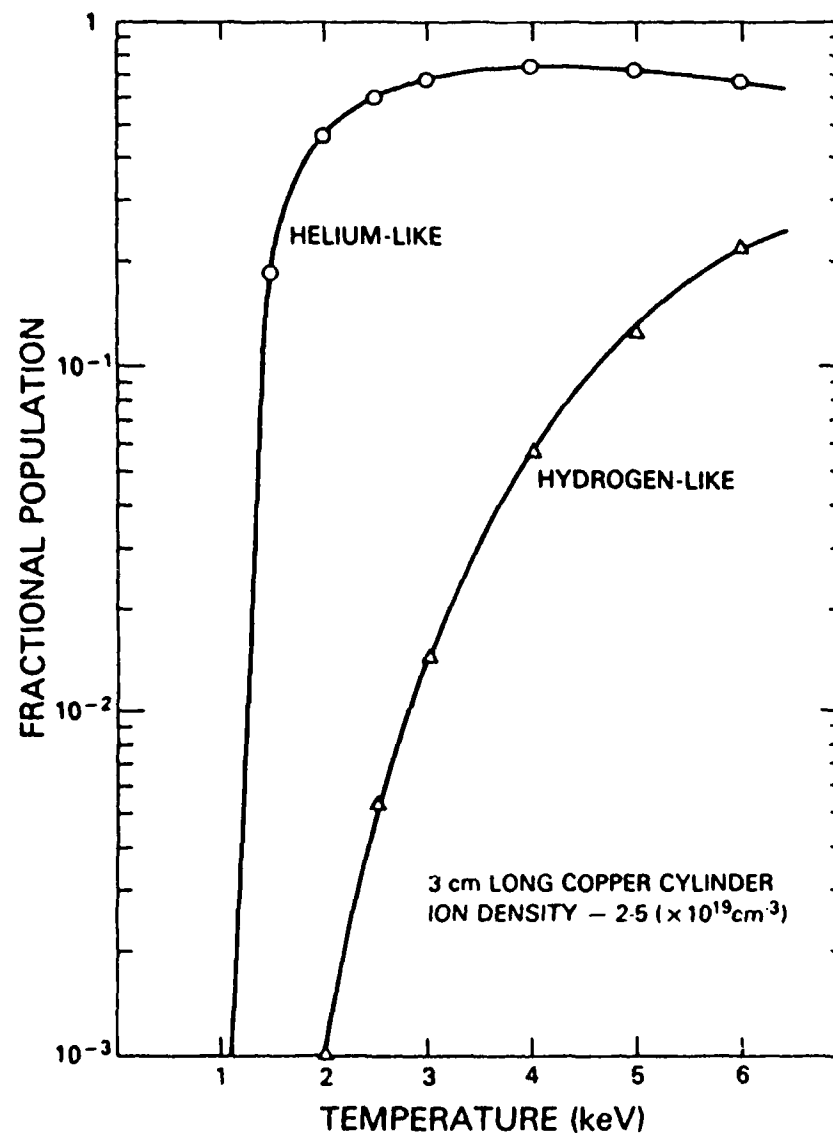


FIG. 7. Heliumlike and hydrogenlike fractional populations versus temperature in a 3 cm long copper cylinder of 1 mm diameter for ion densities between 2×10^{19} and $5 \times 10^{19} \text{ cm}^{-3}$.

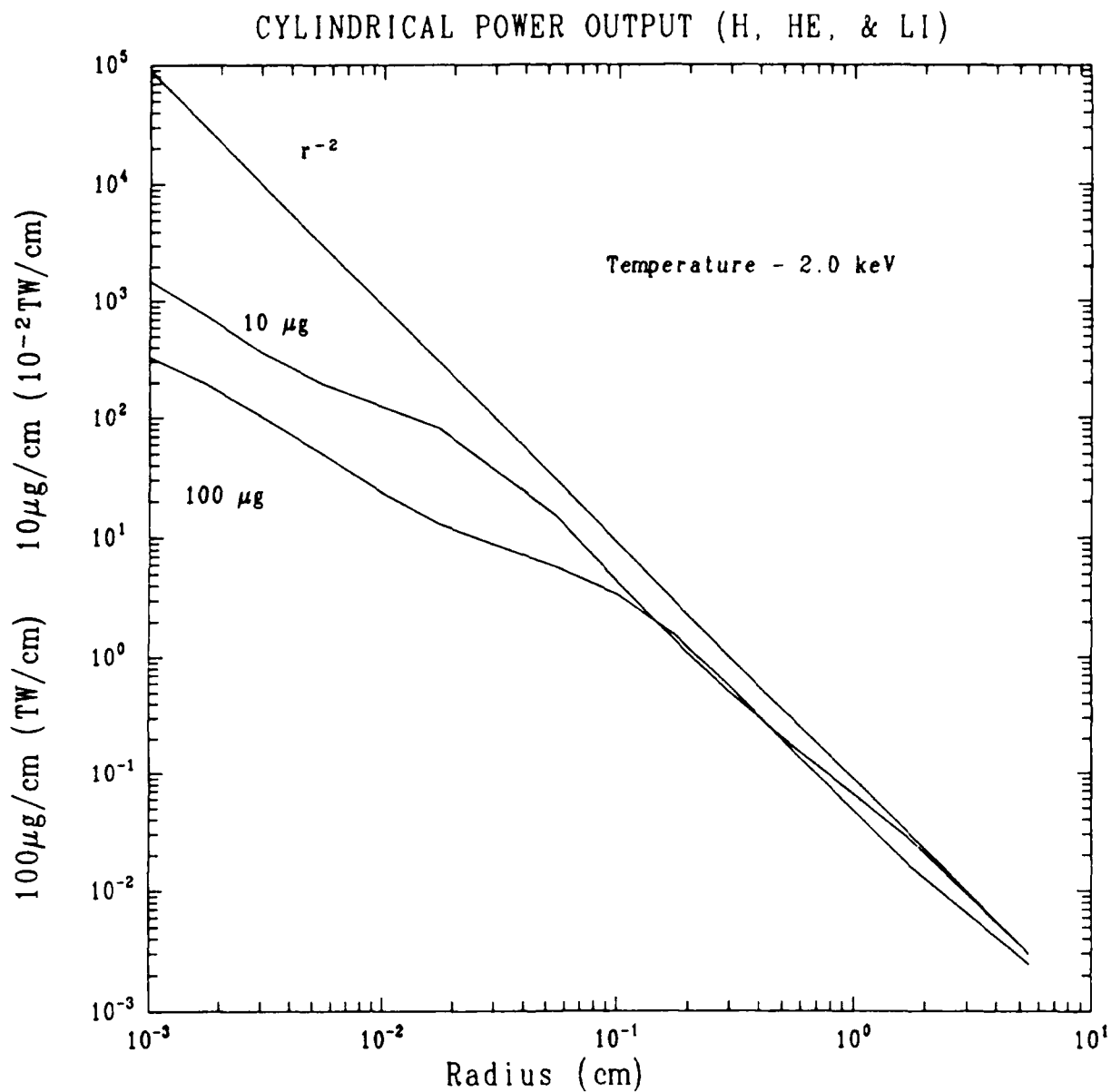


FIG. 8. Power output of hydrogenlike, heliumlike, and lithiumlike ions for 1 cm long cylinders containing 10 and 100 μg copper at 2 keV.

Section B. Krypton-Tungsten Mixtures in Z-Pinch Plasma Implosions

Existing pulse power generators have not yet produced large amounts of line x-rays in the 5-10 keV range. Recently, efforts have been undertaken to explore ways to increase the production of line x-rays in PRS using a variety of approaches. The copper-wire implosion approach is discussed in Section A above. Such approach involves seeding a single wire or gas puff plasma with a high-Z tracer to determine whether the radiative cooling due to the tracer is sufficient to increase the plasma compression in a z-pinch implosion resulting in higher densities and greater radiative yields of high energy photons.

In this study the implosion of a cylindrical annular Krypton (Kr) gas puff plasma seeded with a small amount of tungsten (W) tracer is studied. The theory describing the implosion is based on a dynamic z-pinch model self-consistently coupled to a Collisional Radiative Equilibrium (CRE) ionization dynamics and radiative transport model¹. This model provides a self-consistent picture of the temperature, density, size, and level populations during the plasma evolution. Any pathological behavior, such as instabilities, is ignored in this simplified approach; however, general trends in the plasma behavior should be indicated by this model, and it should serve as a useful guide for more detailed research.

The principal plasma species Kr is comprehensively treated. A low density representation is used for the W impurity². Opacity effects for the W radiation are taken into account in an ad hoc manner by calculating the ratio of total emitted radiation to coronal radiation for Kr², and scaling down the W coronal radiation accordingly.

The implosions modeled in this study are driven by high current discharges, which are based on data obtained from Physics International Company regarding the output of their Double-EAGLE generator³.

The first current profile considered was the triangular shaped pulse shown in Figure 1. Comparisons between the responses of a pure Kr plasma with a mixture of 90% Kr - 10% W by mass were made. Results for different initial cylindrical widths for the plasma were calculated for mass loadings of 175, 200, and 225 $\mu\text{g}/\text{cm}$. The cylinder length was taken to be 3 cm, and the initial outer and inner radii were chosen so that the average plasma radius was initially about 1.5 cm. Figures 2a - 2d shows the variations of the minimum plasma radius and the maximum ion density, temperature, and total radiation with initial plasma shell width and mass.

In each case, the W-seeded plasma gives a better implosion than the pure Kr case. In this model, this effect is due to the enhanced radiative cooling from the W impurity.

A second set of calculations was performed using the current profile shown in Figure 3. The use of the second profile allows for comparing the effect of a flat peak with 25 nsec duration with the initial triangular shaped profile. For these simulations, the mass was kept constant at 225 $\mu\text{g}/\text{cm}$, but calculations for pure Kr, 90% Kr - 10% W, and 80% Kr - 20% W were performed; Figure 4 summarizes these results for the same extremal parameters shown in Figure 2. These curves again indicate that seeding the Kr plasma with a W impurity enhances the implosion, and that the larger the amount of the impurity, the better the implosion.

Comparison of Figures 2 and 4 for the 100% Kr and 90% Kr - 10% W results indicate, as might be expected, that the flat-topped current trace in Figure 3 gives lower minimum radius and higher maximum ion densities and total radiation than the current pulse in Figure 1. For the temperature, however, this trend is only observed at the higher plasma widths. The reasons for this temperature behavior are not clear. Another interesting feature of Figure 2 is the apparent virtual independence of maximum temperature on plasma width, whereas in Figure 4 there is a stronger dependence.

It should be emphasized that the numerical results indicated on these figures are obtained from a zero-dimensional simplified treatment of the dynamics and should be interpreted accordingly. A more sophisticated treatment would involve multi-zone calculations in one or more dimensions with coupled hydrodynamics and radiation transport. Also, the impurity element should be treated on an equal footing with the principal species; i.e., using a full atomic model with radiation transport for both. Such a program could become very costly in terms of computer time and storage.

CONCLUSIONS

Seeding with trace amounts of high-Z elements produces the desirable effects; better compressions, higher densities, and greater radiative yields. This method of enhancing yields appears very promising and will be investigated further. If trace amounts of one element is promising, trace amounts of several elements may be of even greater utility as opacity effects on the radiative cooling may be reduced⁴ in this faction.

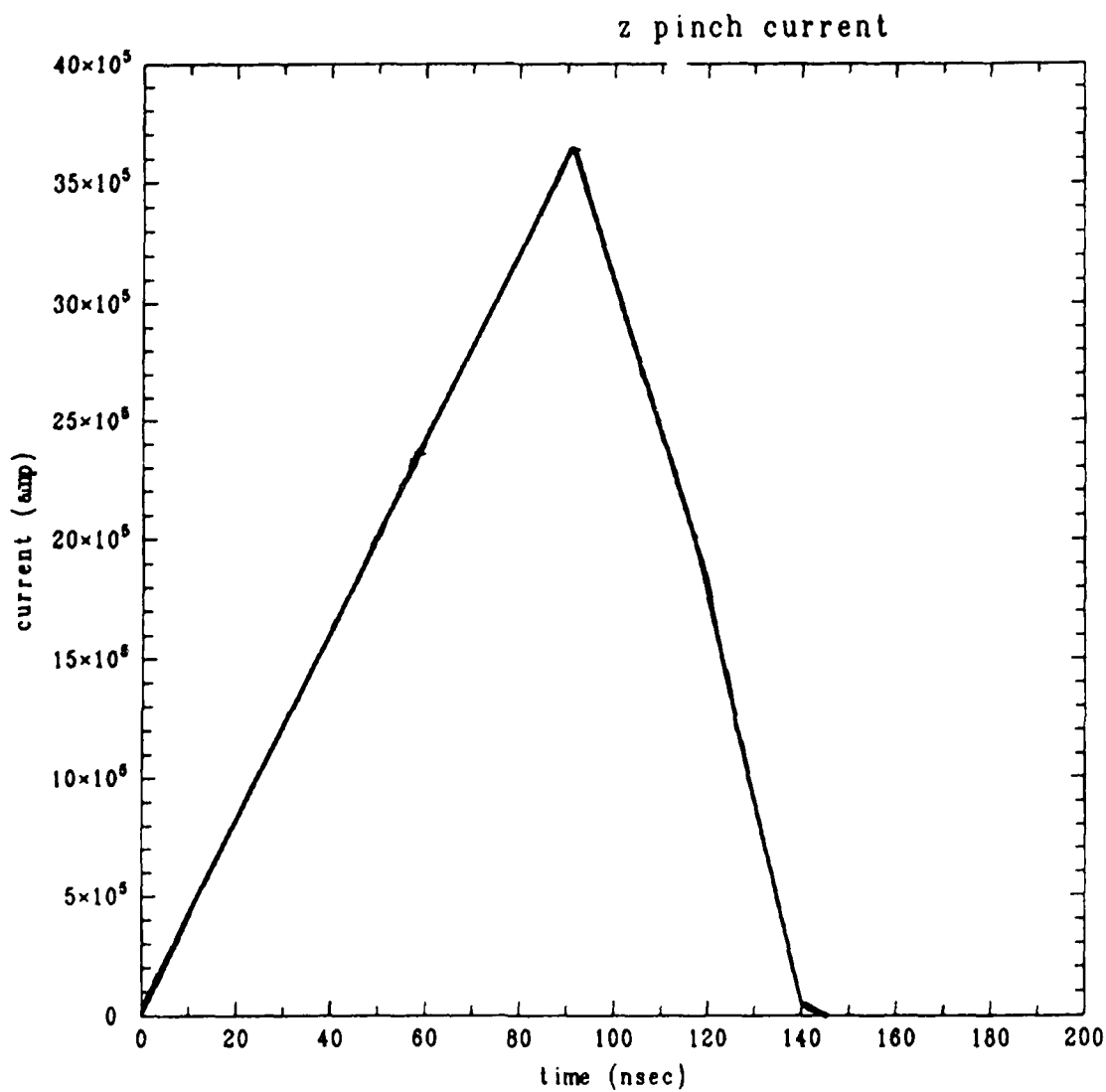


Figure 1

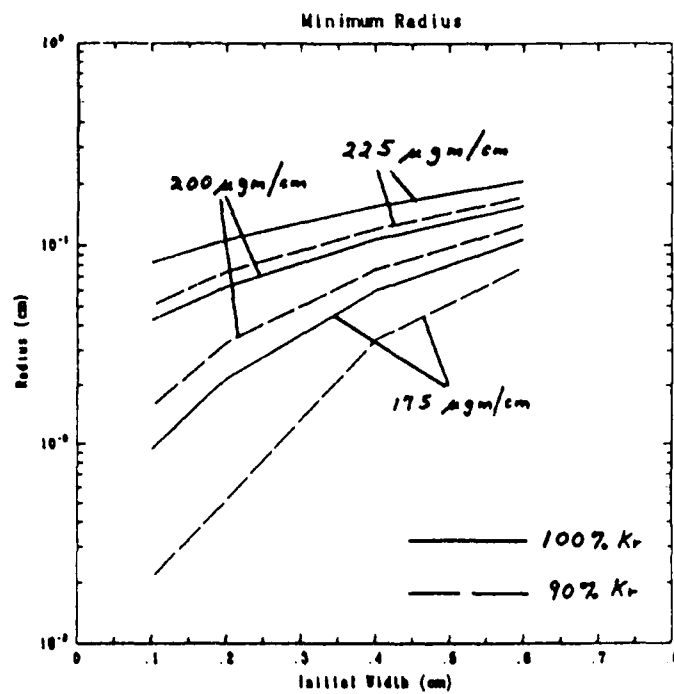


Figure 2a

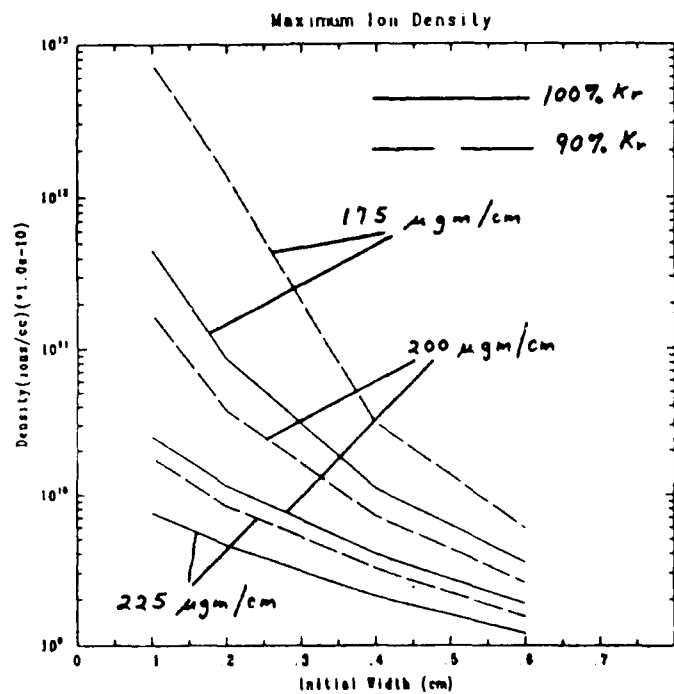


Figure 2b

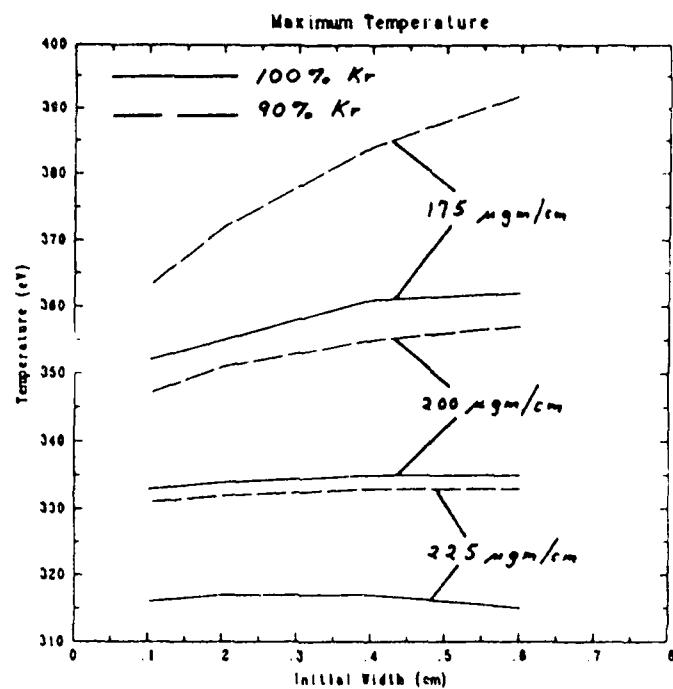


Figure 2c

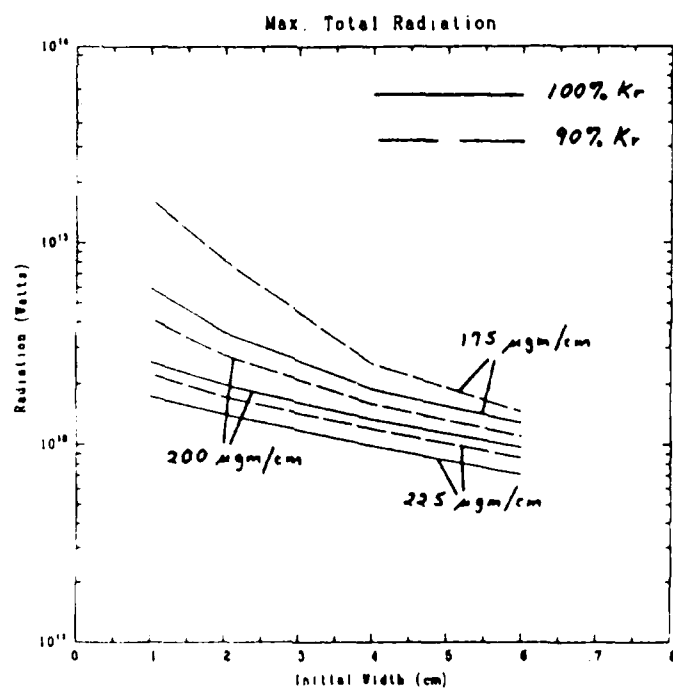


Figure 2d

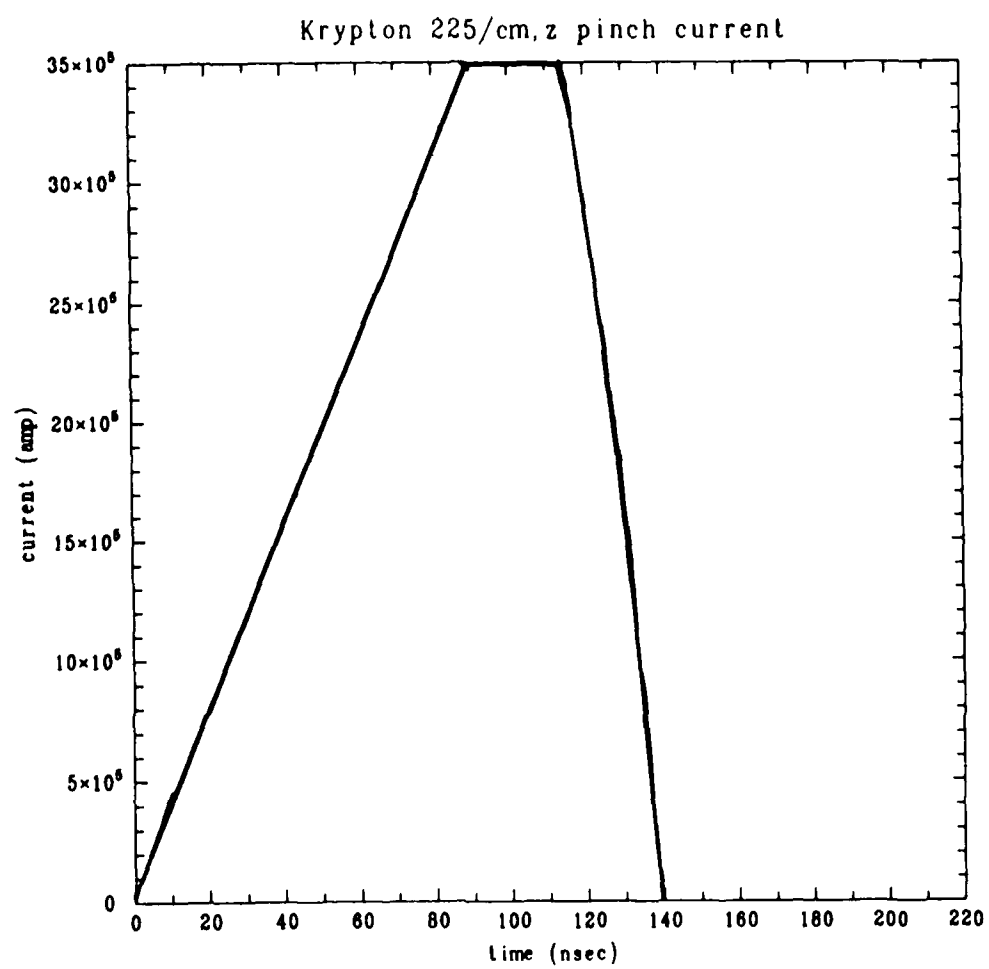


Figure 3

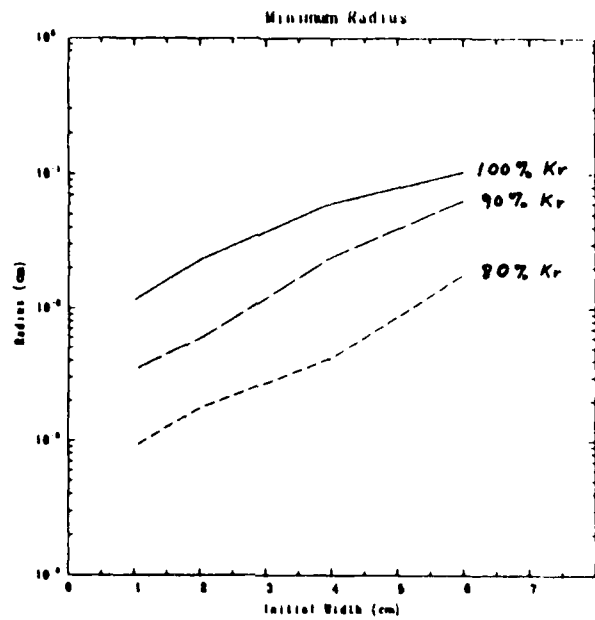


Figure 4a

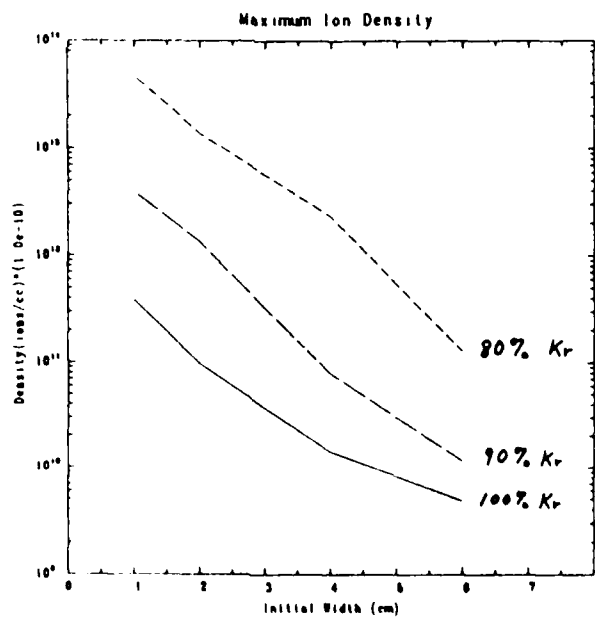


Figure 4b

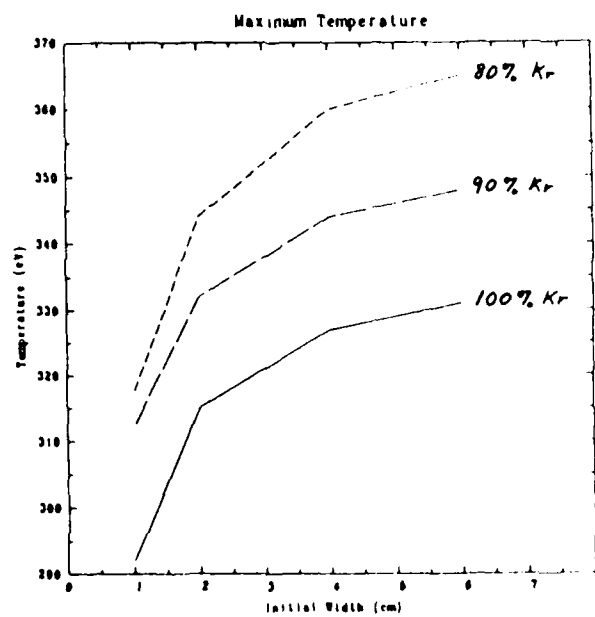


Figure 4c

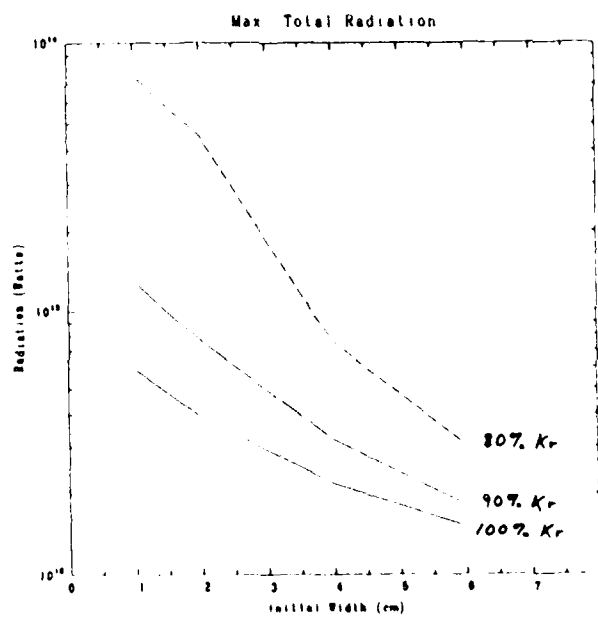


Figure 4d

References

1. J. Davis, C. Agritellis, and D. Duston, NRL Memorandum Report 5615 (1985) Simplode: An Imploding Gas Puff Plasma Model I. Neon (ADA 157456).
2. D. E. Post, R. V. Jensen, C. B. Tarter, W. H. Grasberger, and W. A. Lokke, Atomic Data and Nuclear Data Tables 20, 397 (1977).
3. M. Krishnan, Physics International Company (1986) (private communication).
4. J. P. Apruzese and J. Davis, J. Appl. Phys. 57, 4349 (1985).

Section C. K-Shell Yield from an Argon Gas Puff

This section explores theoretically the determination of the parameter space under which Gamble II - like devices produce maximum K-shell emission. In particular we try to optimize the mass loading and initial radial position of the gas puff.

The work is done by computer simulation using a one-dimensional non-LTE radiation hydrodynamics model. Because the impedance of the plasma can at times influence the electrical characteristics of the machine, we have decided to drive the system with an open circuit voltage profile rather than a current trace.

a. Model

The above parameter study is carried out using a 1-dimensional, 30 zone, 2 temperature, lagrangian hydrodynamics code in which the ionization and radiation dynamics is treated self-consistently using the collisional radiative equilibrium (CRE) radiation and atomic physics models developed and used by the NRL Plasma Radiation Branch¹ over the last several years. In particular the argon model employed utilizes 19 ground states, 44 excited levels and 56 bound-bound transitions. The excited states were chosen to predominantly surround hydrogen-like through lithium-like argon in order to provide good information on K-shell radiative yields, however excited state structure is included for ion levels up to sodium-like argon.

In the subsequent studies we are imploding an annulus of argon gas that is .3 cm between inner and outer radius. The radius R is initially fixed at 1.35 cm and the mass density is varied from 5 to 60 $\mu\text{gm}/\text{cm}$. Once an optimum mass loading is found we fix the mass loading at this value and then vary the initial radial position from .25 to 1.35 cm. The puff is imploded assuming the open circuit voltage profile and machine parameters shown in figure 1. Note, the following results are only valid for those times up until the plasma first rebounds from its central axis. These implosion times will be given and discussed in the results sections.

b. Results for variation of mass loading

In this section we discuss the results for varying the mass loading while keeping the initial radial position at 1.35 cm. The specific loads analyzed are 5, 10, 20, 30, 40 and 60 $\mu\text{gms/cm}$. Except for the lightest mass loadings, the implosion times are long in comparison to the time it takes the current to peak. Therefore, for most of the simulations discussed in this section the electrical circuitry can be assumed to be decoupled from the plasma.

Figure 2 displays total, bound-bound, bound-free and free-free radiative yields. Similarly, figure 3 is almost identical to figure 2, except only radiation which exceeds 1 keV is plotted. From these two plots we find that the components as well as total radiation peaks at around a mass loading of 20 to 30 $\mu\text{gms/cm}$. In particular we find that the radiative yield of interest, i.e. photon energy greater than 1 keV, peaks at 20 $\mu\text{gm/cm}$. At this loading the radiative yield is 2.2 kilojoules for a plasma column of 4 cms length. In the remainder of this section we want to analyze figures 2 and 3 in the hope that we will be able to generalize these results to other materials, mass loadings and circuits.

All of the simulations shown in this section show a $(\text{mass})^{-1}$ dependence of kinetic energy upon mass loading. This result has been noted before², and is due to the fact that the ratio of kinetic energy stored in a small mass to that of a larger mass is inversely proportional to their masses, assuming that the force and the time over which the force is applied are equal. This stored up kinetic energy is transferred to internal and radiative energy as the plasma assembles on axis. This is readily seen in figure 4 where peak values for internal, ionization, kinetic, boundary work and radiative energies are displayed. The values for kinetic energy are taken just before the pinch whereas internal and ionization energies peak right at the pinch. Because radiative yield and boundary work are quantities that are integrated in time, their values are taken just after the implosion. Note, the drop in kinetic energy for the 5 $\mu\text{gm/cm}$ loading is because the mass is so light it implodes before the peak in the open circuit voltage profile, see figure 5.

Just because the lighter masses are able to store more kinetic energy, does not mean that they will be able to transfer this energy to radiation at the time of implosion. One reason this is true is that the $(\text{mass})^{-1}$ dependence also implies that there will be less mass to radiate during

implosion. This is especially true for line radiation which is directly dependent upon the number of ions in an excited state. This point is also made clear in figure 6 where we see that while peak power per unit mass does increase with smaller loadings, the total power eventually decreases. Secondly, because the lighter masses are imploding with much higher velocities, see figure 7, they will be spending much less time near the axis where temperatures and densities are such that radiative power is maximized. This is illustrated in figure 5 where we see that the "dwell" time, i.e. the time between peak values of kinetic energy before and after implosion varies from tens of nanoseconds for the heavier masses to fractions of a nanosecond for the lighter loads.

We therefore find that while it is true that we can couple more energy into a lighter load one eventually reaches a small enough loading that it is no longer possible to extract this energy during assembly on axis because of reduced mass and shorter assembly time. This point is clearly illustrated in figures 8 and 9 where we see the almost total conversion of kinetic energy to radiation for the 30 $\mu\text{gm/cm}$ loading whereas the 10 $\mu\text{gm/cm}$ loading interaction is nearly elastic. Note, how much longer the dwell time of the 30 $\mu\text{gm/cm}$ mass is than the 10 $\mu\text{gm/cm}$ mass.

In the beginning of this section it is mentioned that the heavier mass loadings implode late enough in time that they can be assumed to be decoupled from the fields at the time of implosion. This is seen in figure 8 whereby if one adds up the kinetic and internal energy just before implosion and compares it to the internal energy right at implosion, we find that the two are approximately equal. However, this is not true for the 10 $\mu\text{gm/cm}$ mass depicted in figure 9. There, we discover that the combination of internal and kinetic energy before implosion is significantly less than the peak value of internal energy. The implication is that the lighter loads are imploding early enough in time that there is a lot of magnetic field energy left that can do boundary work on the plasma during assembly on axis. Some of this work will change the internal energy of the plasma and part will be radiated out of the system. For the example in figure 9, we find it predominantly changes the internal energy of the plasma. The consequences of choosing one time of implosion over another will be discussed in the next section.

c. Results for variation of initial radial position

We now fix the mass loading at $20 \mu\text{gm/cm}$ and vary the initial radial position of the puff. The specific values chosen for the following simulations are centered at .25, .5, 1.0 and 1.35 cms.

An examination of figures 10 and 11 show that we can expect an increase in the radiative yield of high energy photons, greater than 1 kev, by a factor of two over the results of the previous section by changing the initial radial position from 1.35 cms to .5 cms. This is an interesting result because we have the same mass and dwell time but less peak kinetic energy for the plasma starting at .5 cms. The dwell time is displayed in figure 12 and the peak kinetic energy is shown in figure 13. Therefore, by the arguments of the previous section, we expect figure 13 to show that radiative yield peaks at the same radial position as kinetic energy, i.e. at an initial position of 1 cm. However, what we find instead is that radiative yield is maximized by starting even closer to the axis at an initial radial position of .5 cm.

The discrepancy lies in the fact that the arguments of the last section are based on the premise that the plasma is decoupled or nearly decoupled from the electrical fields during assembly on axis. We can see from the implosion times, see figure 12, that the only plasmas nearly decoupled from the fields are those with initial positions greater than 1 cm. There is a different phenomenon taking place for plasmas with smaller initial positions because they are still strongly coupled to the fields. What is happening is that the decoupled plasmas encounter only a single shock as they hit the axis whereas the coupled plasmas are multiply shocked. These coupled plasmas are not only shocked by running into the axis but they continue to be shocked by the fields as boundary work is done on the plasma. The situation is similar to inertial confinement fusion (ICF)³ where it is well known that if you want to compress a fluid it should be done by multiple shocking along an isentrope rather than one big shock. The lower the adiabat of the shock the larger the compression for the same imploding pressure. This is the reason that the coupled plasmas having lower peak kinetic energy have correspondingly lower temperatures and higher densities at implosion, see figure 14. The lower kinetic energy means less preheating, therefore the shock adiabat is lower.

The way this relates to an increase in radiation for the smaller radii plasmas is that recombination and bremsstrahlung radiation are

proportional to the square of the density. We therefore expect the radiative yield to increase for plasmas that are more strongly coupled to the fields because they are more compressed. The plasma will be most strongly coupled if it implodes right about the time of maximum voltage which for these simulations corresponds to the .5 cm case. Although the .25 cm simulation is imploding so early in time that the fields have not had time to gain maximum strength. The kinetic energy is low enough, see figure 13, that the preheating it produces is small compared to the other simulations. This allows for compression to much higher densities at the expense of lower temperatures as is illustrated in figure 14. The point is also made in figure 10 where we see that there is only a difference of 600 joules/cm of total radiative yield between the .25 cm and .5 cm simulations, but an examination of figure 11 shows that all of it comes from the high energy component, corresponding to higher temperatures. Another illustration of the density dependence of radiation is again depicted in figures 10 and 11 where one sees a dramatic increase in recombination radiation but a drop in line radiation as the initial plasma radius is moved inward allowing the plasma to be more strongly coupled to the fields.

d. Summary and conclusions

We have shown that imploding gas puffs operate in two regimes, one in which the plasma implodes late enough in time that it can be considered to be decoupled from the electrical fields as it hits the axis and another in which the plasma implodes early in time such that it is still coupled to the fields.

For the plasmas that are decoupled we find that more kinetic energy can be stored in a lighter mass. However this energy is less efficiently converted to radiation not only because of the smaller mass but also because the plasma spends less time in its maximum imploded state. If one is trying to maximize the radiative yield for a plasma that is decoupled from the electrical fields it is a trade off of getting enough energy into the system and then being able to efficiently radiate at implosion. For an argon plasma that starts sufficiently far away from the axis that it is decoupled from the fields at implosion, we found that the best radiative yields were achieved using a mass loading of 20 to 30 $\mu\text{gms/cm}$. At this

setting we obtain total radiative yields of 4.8 kilojoules of which almost half is composed of photons with energies greater than 1 kev.

The coupled plasmas exhibit a different behavior that is similar to ICF in that the fields multiply shock compress the plasma as it implodes. The adiabat upon which the plasma is compressed is dependent upon the kinetic energy of the plasma, the lower the kinetic energy the lower the adiabat and consequently the compression is higher. Because the plasmas starting closer to the axis have less time to gain kinetic energy, they become more compressed. Since recombination and bremsstrahlung radiation are proportional to the square of the density, the radiative yield increases for plasmas starting closer to the axis because of their higher densities. The adiabat upon which the plasma is compressed determines the radiative spectrum. We find for argon that the radiative yields, both total and high energy, are doubled over the results previously mentioned if the initial starting position of the plasma is such that the plasma implodes on axis about the same time as the open circuit voltage profile peaks. Note, more investigation needs to be done on the plasmas that are coupled to the fields because they are in a regime that is susceptible to instabilities.

All of the simulations presented in this work are for a Gamble II - like open circuit voltage profile that corresponds to the absence of a plasma erosion opening switch (PEOS). Since it has been experimentally found that the presence of a switch lowers the peak current, the arguments of this report predict that the peak velocities and radiative yields, for a given peak current, would also be reduced. This prediction is in agreement with "SIMPLODE" ⁴ a 0-D radiation hydrodynamic model developed by the Plasma Radiation Branch that simulates both the switch and non-switch cases. However this prediction is only valid when the fields are decoupled from the plasma at implosion, more analysis needs to be done for the coupled plasmas. Also, this prediction does not include any stability analysis, which needs to be included in order to make a judgement about the merits of a switch versus a non-switch. It is conceivable that the benefits of increased uniformity of the plasma resulting from faster rise times produced by the use of a PEOS far outway the side effects of reducing the plasma current.

Comparisons of the results of this model with SIMPLODE are in excellent agreement when it comes to global comparisons of radiative yield versus mass loading for a fixed initial radius, i.e. assuming that the fields are decoupled at implosion. Although the SIMPLODE results are for neon the trends are almost identical. It is therefore recommended that the 0-D models be utilized for overall scoping of a problem and then for finer details, such as producing a radiative spectrum, the 1-D models should be employed.

References

- 1) The ionization and radiation dynamics models are referenced in D. Duston, R. Clark, J. Davis and J. Apruzese, Phys. Rev. 27, 1441 (1983).
- 2) R. Terry, J. Guillory, DNA REPORT 5926f.
- 3) J. Knuckolls, L. Wood, A. Theissen and G. Zimmerman, Nature Vol. 239 (1972).
- 4) J. Davis, C. Agritellis and D. Duston NRL MEMO REPORT 5515.

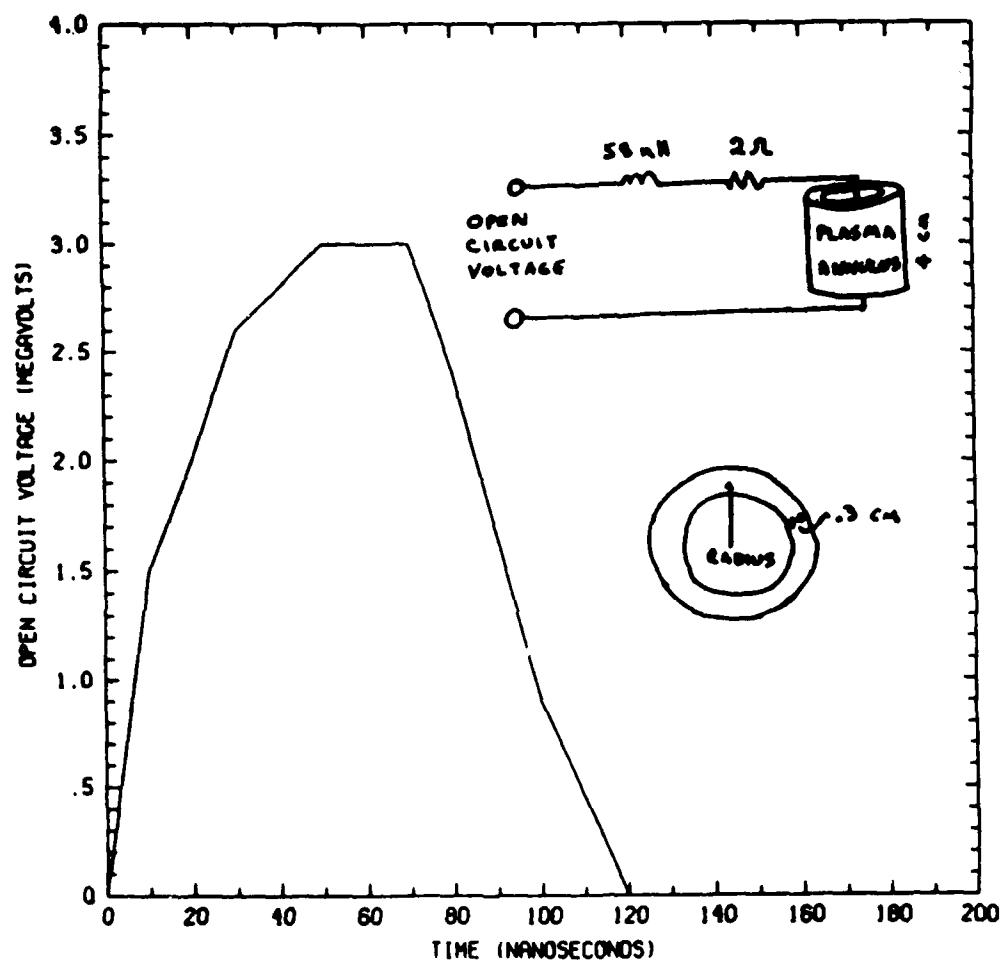


Fig. 1 — Gamble II voltage profile and circuit diagram.

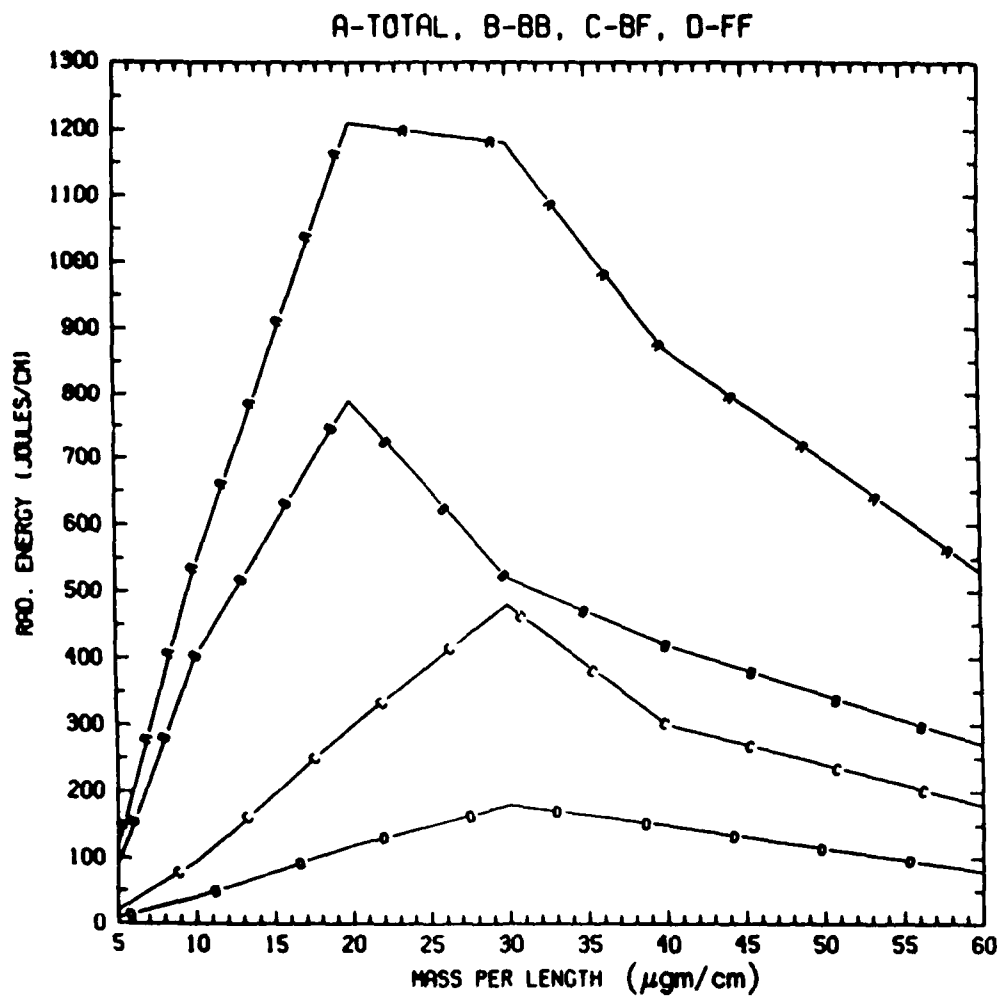


Fig. 2 — Radiative yield as a function of mass loading, A is total, B is bound-bound, C is recombination and D is bremsstrahlung radiation.

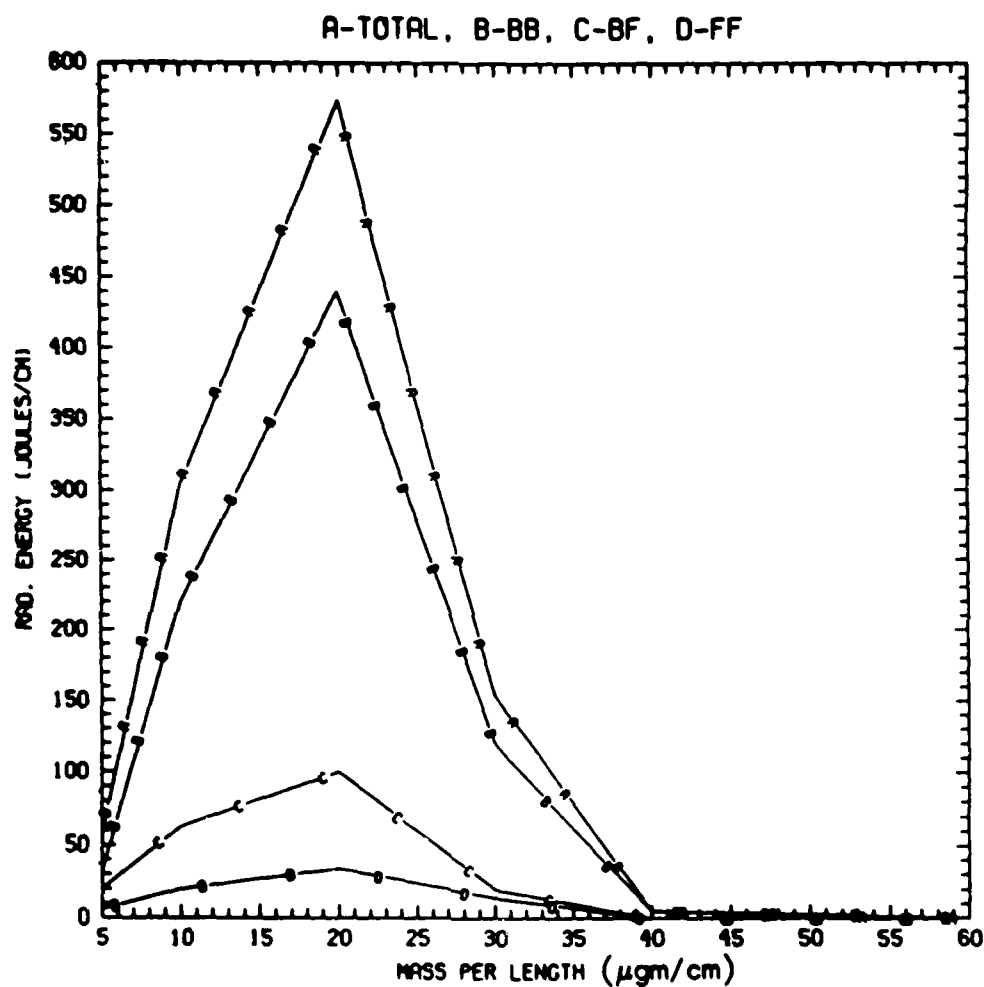


Fig. 3 — K-shell radiative yield ($> 1\text{keV}$) as a function of mass loading. A is total, B is bound-bound, C is recombination and D is bremsstrahlung radiation.

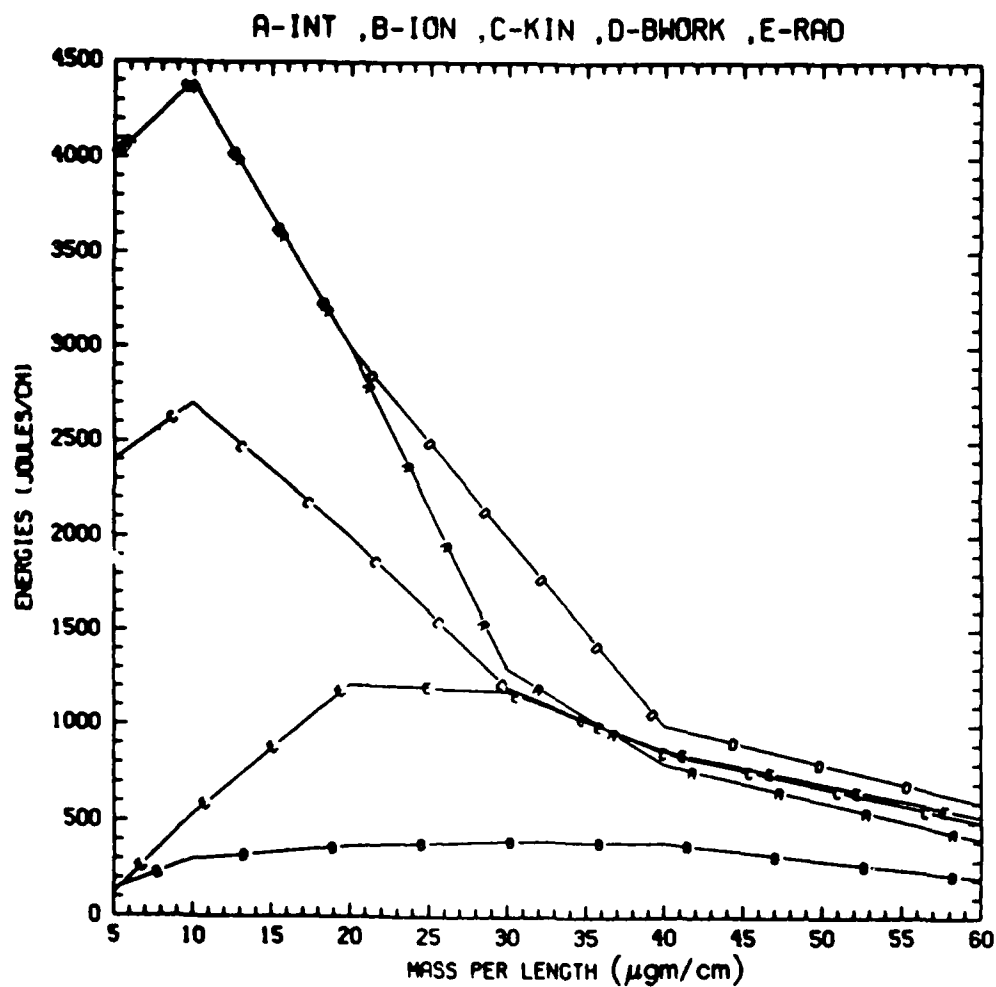


Fig. 4 — Peak values for A - internal, B - ionization, C - kinetic, D - boundary work and E - radiative yield energies as a function of mass loading

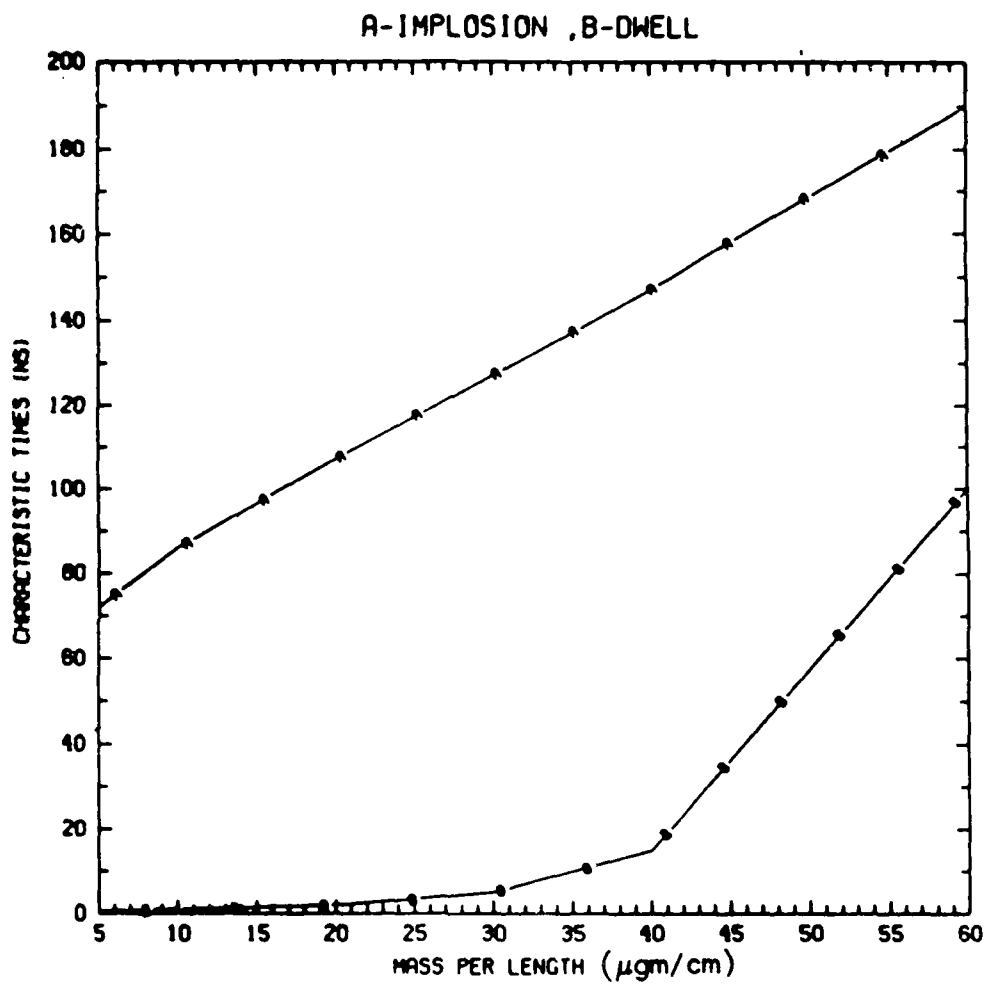


Fig. 5 — Implosion and dwell times versus mass loading, where dwell time is the time the plasma spends in its maximum compressed state.

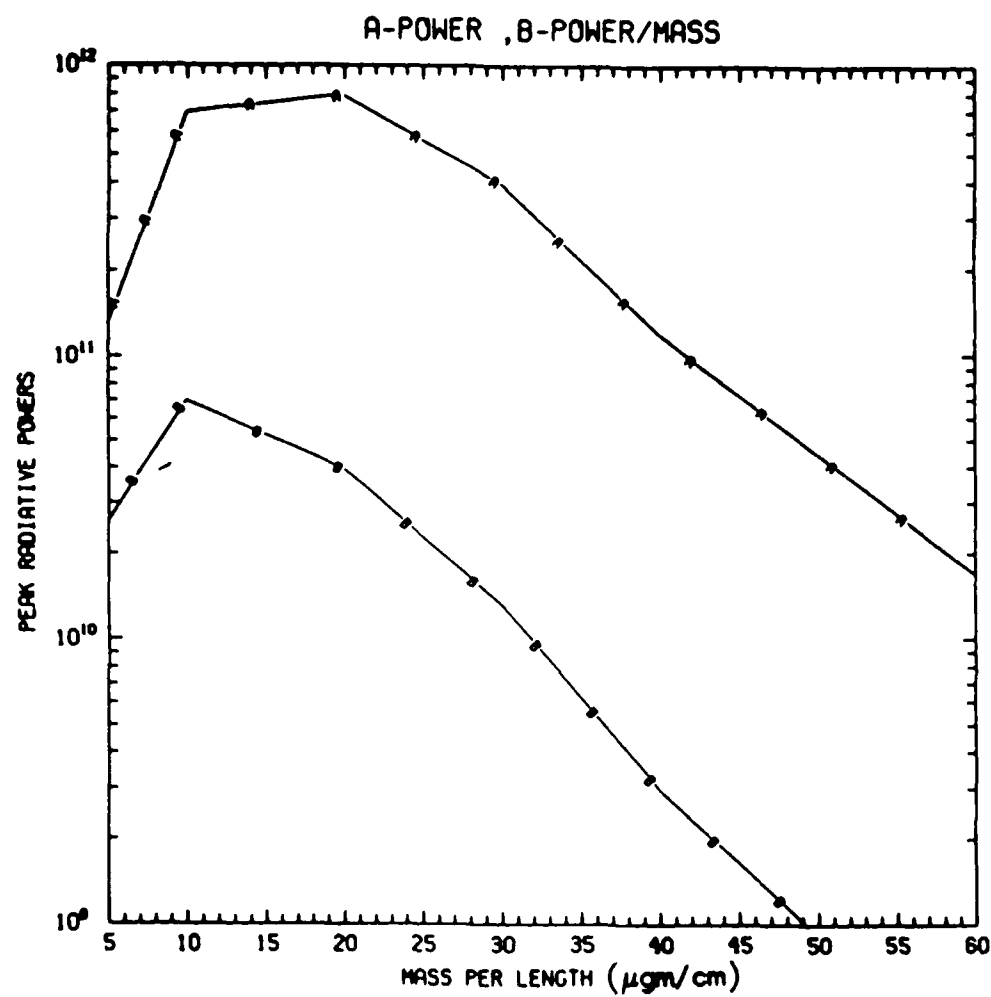


Fig. 6 — Peak power levels versus mass loading.

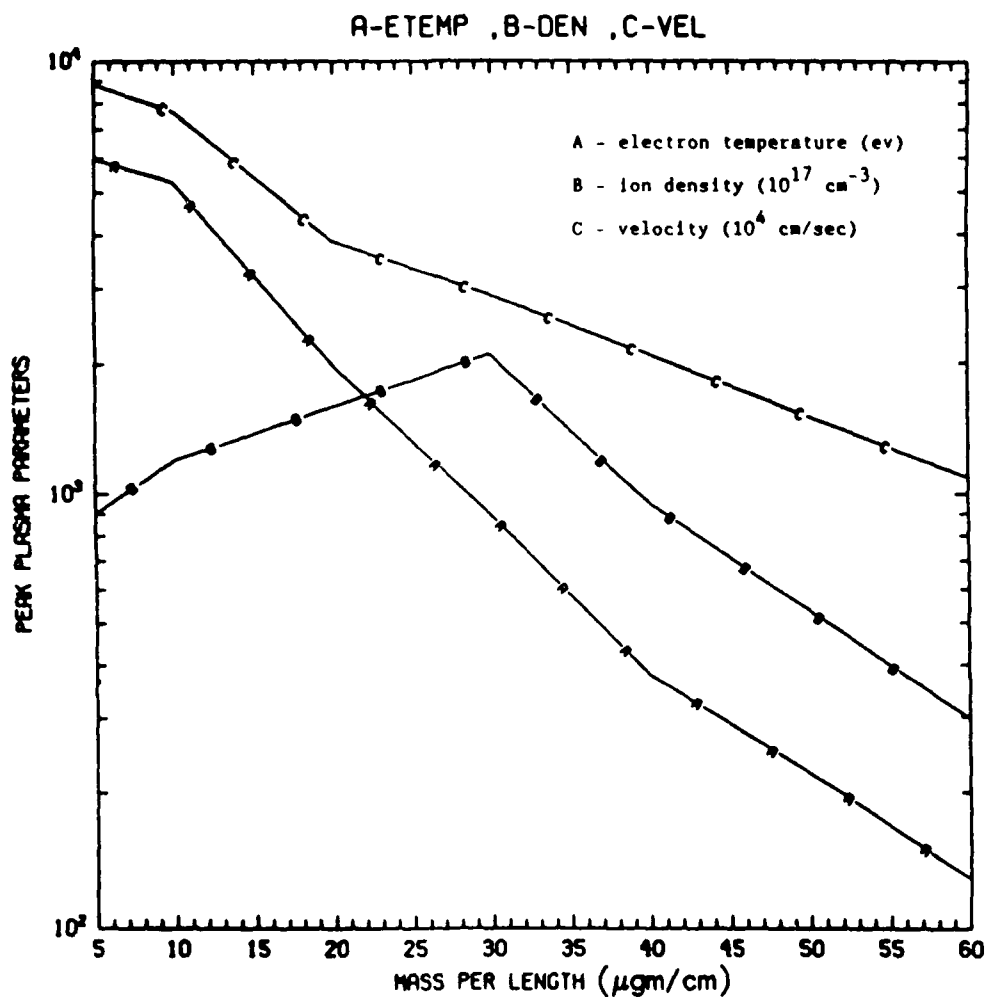


Fig. 7 — Peak A - electron temperature, B - ion density, and C - velocity versus mass loading, temperatures and densities peak at implosion while velocities peak before implosion.

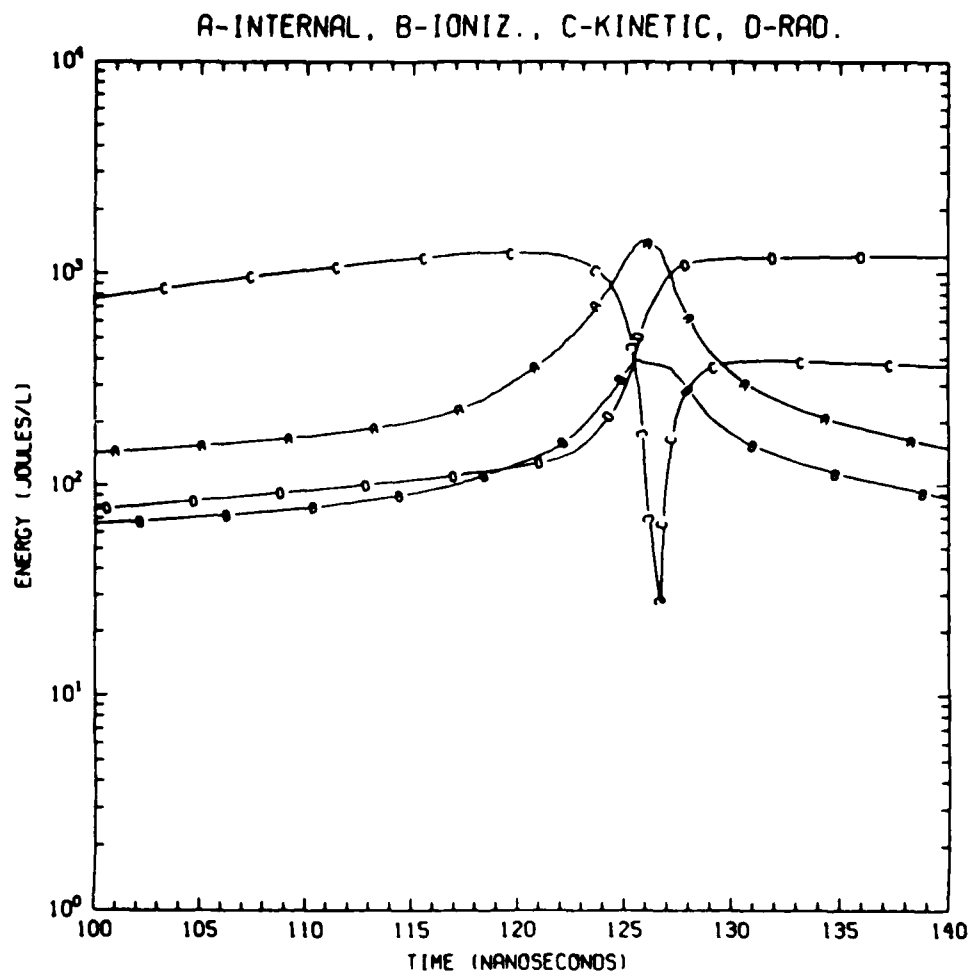


Fig. 8 — A - internal, B - ionization, C - kinetic and D - radiative energies versus time for a $30 \mu\text{gm/cm}$ mass loading with initial radial position of 1.35 cm.

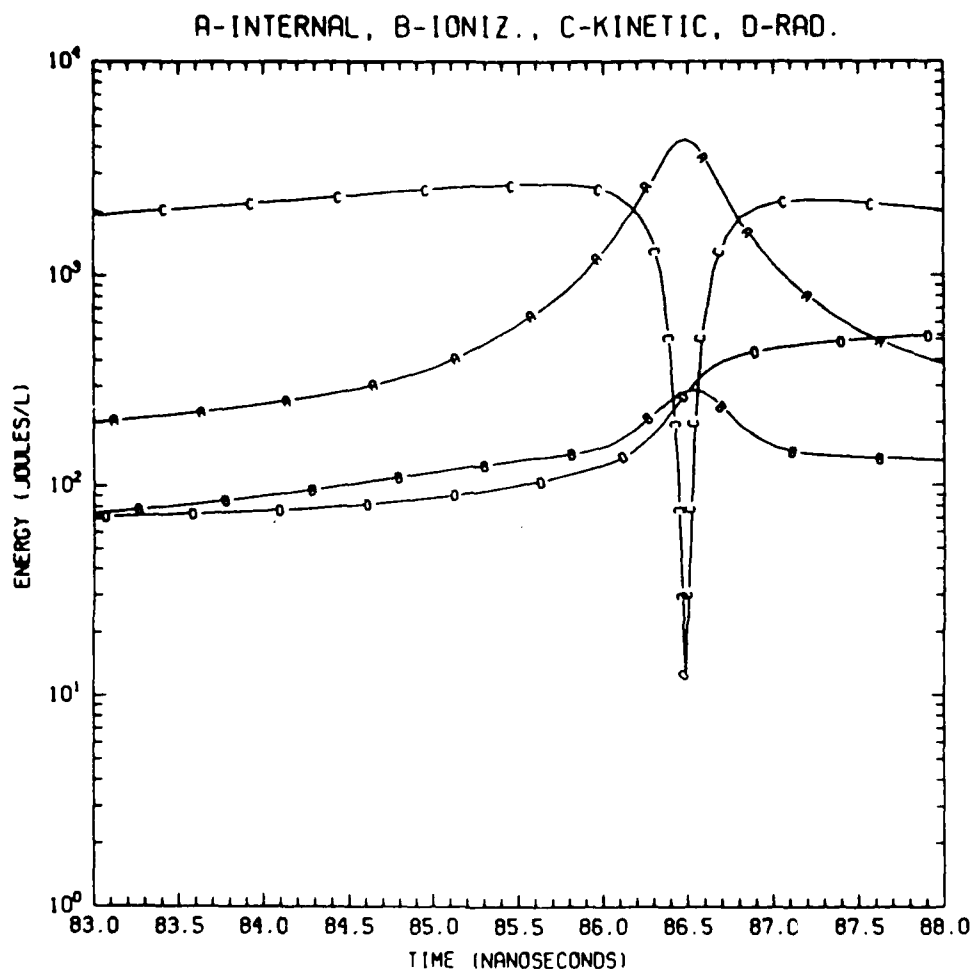


Fig. 9 — A - internal, B - ionization, C - kinetic and D - radiative energies versus time for a $10 \mu\text{gm/cm}$ mass loading with initial radial position of 1.35 cm.

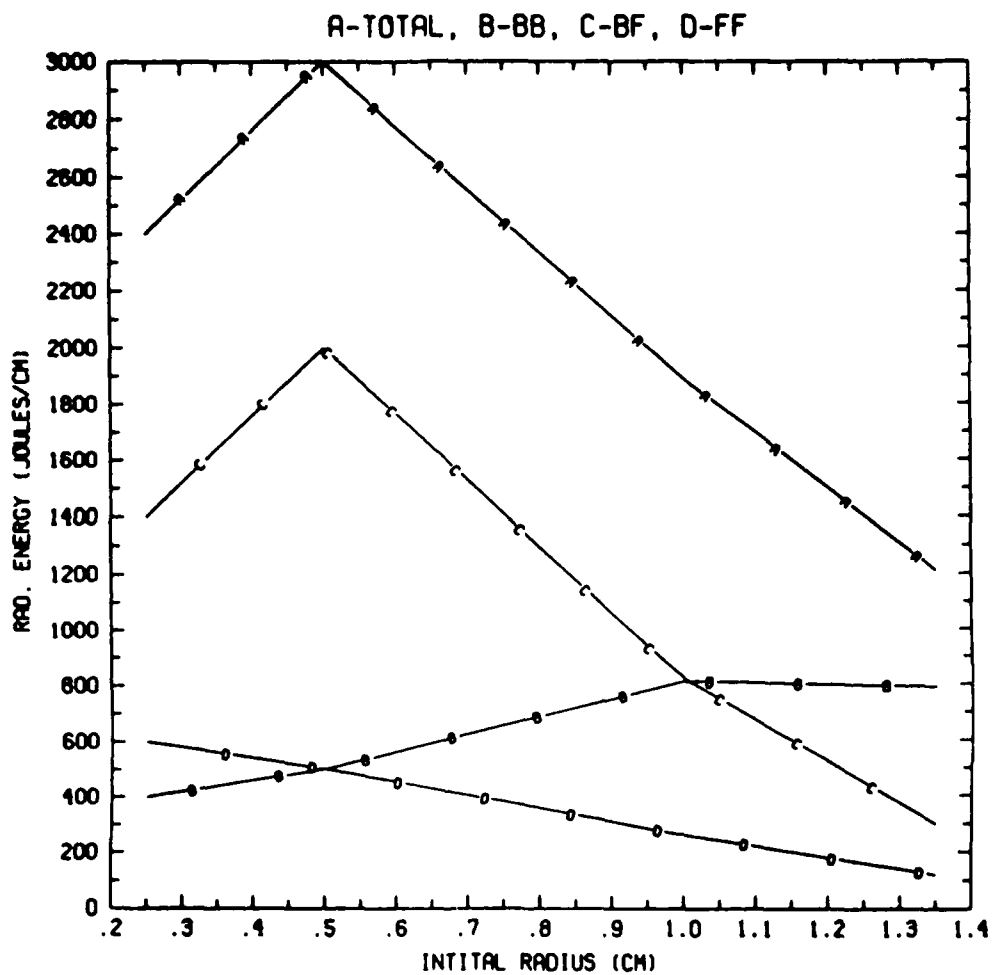


Fig. 10 — Radiative yield versus initial radial position, A is total, B is bound-bound, C is recombination and D is bremsstrahlung radiation.

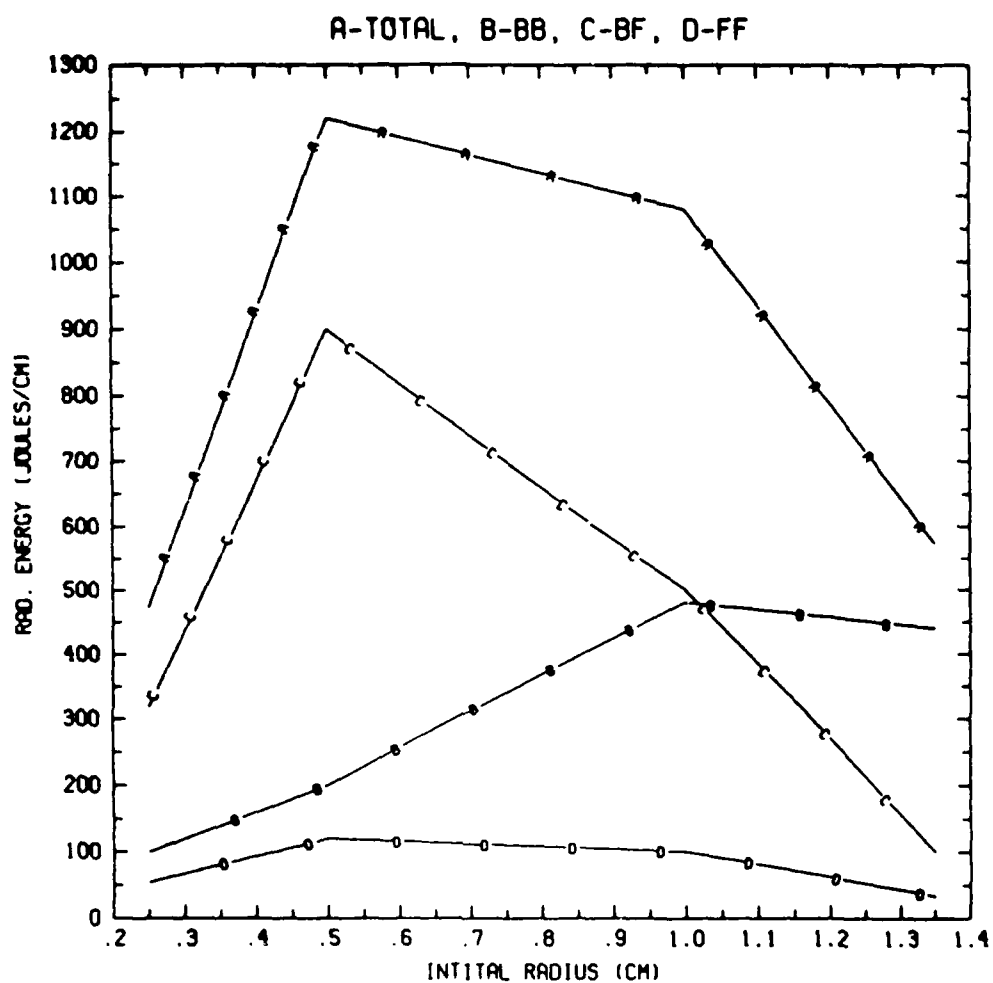


Fig. 11 — K-shell radiative yield versus initial radial position. A is total, B is bound-bound, C is recombination and D is bremsstrahlung radiation.

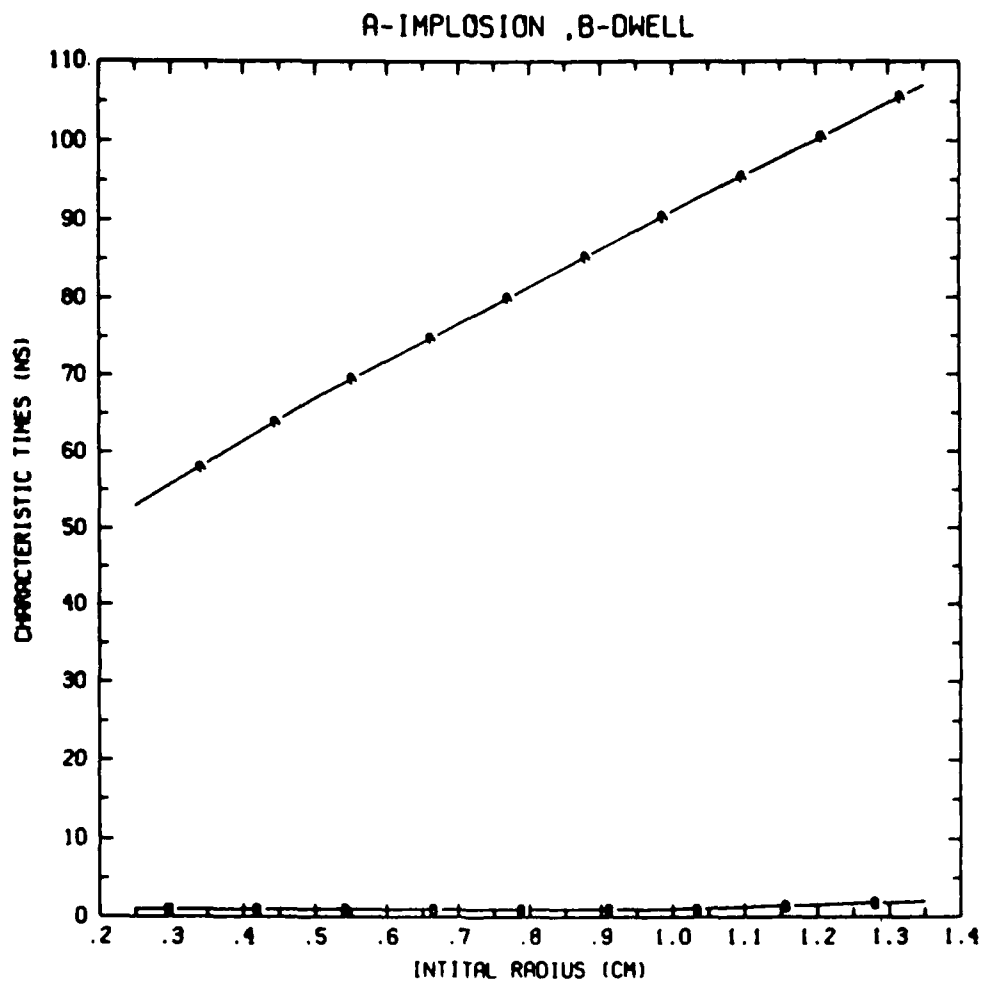


Fig. 12 — Implosion and dwell times versus initial radial position.

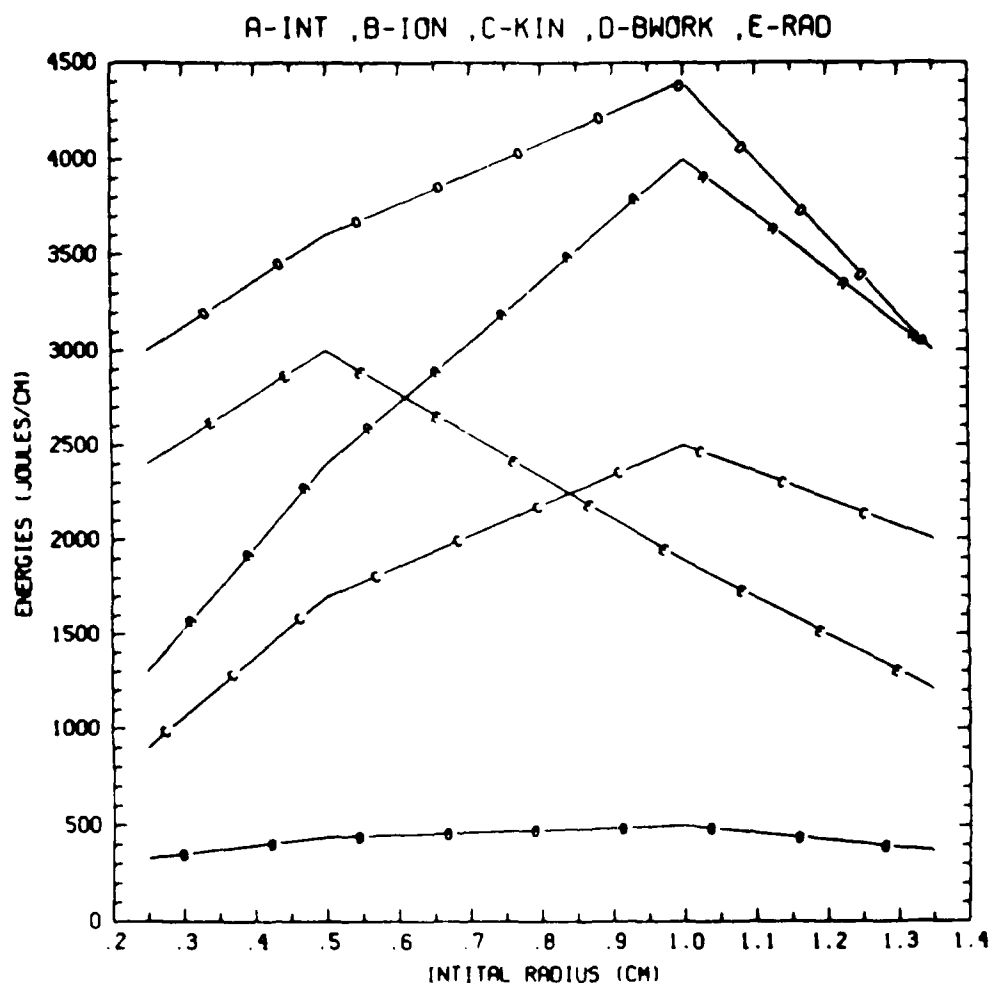


Fig. 13 — Peak values for A - internal, B - ionization, C - kinetic, D - boundary work and E - radiative yield energies versus initial radial position.

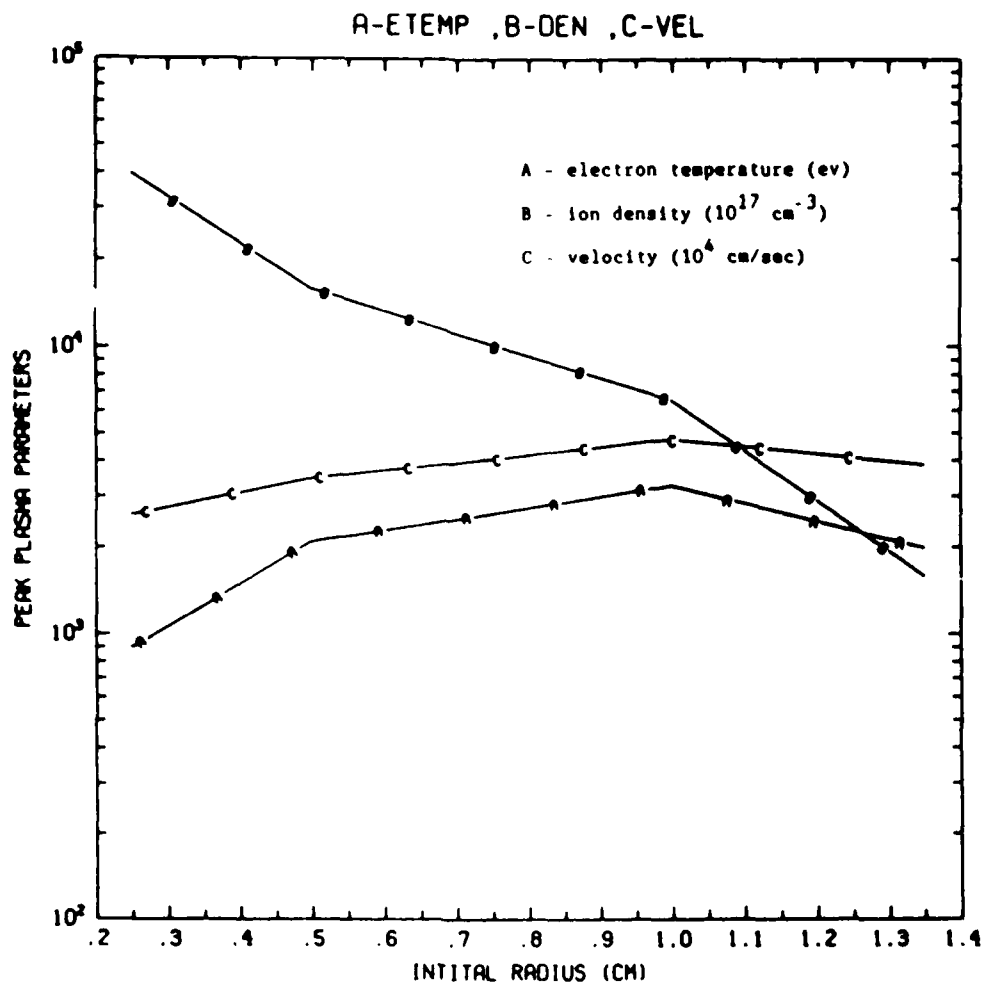


Fig. 14 — Peak values for A - electron temperature, B - ion density and velocity.

In order for a Z-pinch to exhibit a narrow radiation signature in time, the plasma column must be uniform along the Z direction during the time when the optimum implosion conditions are realized. Of particular importance, is the manner in which the hollow cylindrical shell of gas formed by a high Mach number nozzle behaves during the runin phase of the implosion. The spread in the gas due to expansion after exiting the nozzle can make the stagnation time of the implosion nonuniform in Z. This phenomena is often referred to as "zippering". In addition to the annular outside puff, these configurations may also include a central gas puff which can serve as a radiation convertor¹. When the outside puff stagnates on the inner puff, the zippering effect is transferred to the inner puff resulting in density variations along Z at the time of peak compression. In this paper, we will examine representative nozzle designs in use on experiments which are currently being planned and/or conducted at the Physics International Company (hereafter, referred to as PI). Both the outside and central puff are taken to be krypton. The mass of the inside puff is set to a variable fraction of the outside puff mass. The three designs which have been considered are:

- (1) Outside radius of 2.2 cm, inside radius of 0.8 cm, and outside puff centered at a radius of 1.4 cm. Angular spread of 20 degrees on the outside and angular spread of 9 degrees on the inside (i.e., inside meaning on the side closest to the center of the column). The differences in

angular spread have been attributed by PI to interactions with the central gas puff. This gives rise to less of a spread on the inside.

(2) Outside radius of 2.2 cm, inside radius of 1.8 cm, and centered at 2.0 cm. For the outer puff, an outside spread of 25 degrees and an inside spread of 15 degrees. Expansion of the inside puff is 20 degrees.

(3) Same as (2) above but with an overall tilt of the outside puff inward.

The radius of the inner puff is always taken to be 2.5 mm. Unless otherwise stated, the inner puff can be assumed to have an angular expansion of 20 degrees. Figure 1 shows a schematic of the nozzle design and further illustrates the meaning of these values. In this report, we will specifically discuss designs (2) and (3).

Computational Considerations

These simulations were carried out using a two-dimensional Lagrangian hydrodynamics code. Earlier applications and discussions of this code, PRISM, appear in previous annual reports². The one-dimensional version of this code was used to investigate the radiative yields of double puff implosions and was reported on in reference 1.

The typical mesh size was 30x40 with spacing determined by resolution considerations in the two puffs. The nozzle flow itself is neglected except in the initial density profiles. The density variations are given by Gaussian profiles in the radial direction with the full-width-at-half-maximum increasing along Z according to the angular spreads dictated by the

particular nozzle design. The angles chosen are described above. After computing the profiles in both R and Z, the density is normalized to a given mass per unit length for each slice along Z. The mesh is extended at both the top and bottom of the pinch in order to prevent disturbances which propagate in Z from being reflected back into the pinch region (i.e., Z between 0 cm and 3 cm).

In addition to the hydrodynamics, two-temperature thermal transport with an idealized equation of state is used. The magnetic field is advanced according to resistive diffusion and a boundary value given by a temporal current profile.

Discussion of the Results

Several computer runs were made in which the initial nozzle parameters as well as the ratio of inside to outside mass were varied. The parameters are those of designs (2) and (3), which were discussed above. Both the temporal profile and magnitude of the current were fixed. They were provided for these simulations by PI. Our main interest in these runs was to look for regions of uniform density along or near the central axis. For this reason, a graphics contour plotting routine which displayed only the 50% and 25% values of the peak electron density was used. The results from the hydrodynamic simulations are discussed below.

Figure 2(a) shows the density contours near the peak of the implosion of a double-puff design in which the central puff had a mass equal to 80% of the outside mass. In this run, the tilt angle was set at 5 degrees. The 50% of peak density contour is shown with a solid line, while the 25% contour is dashed. The inside contour is seen to have about 1 cm along the central axis. The length of the 25% contour, however, is 1.5 cm.

Both contours are contained within a 1 mm radius (note that the R and Z axis scales are not the same).

Figure 2(b) shows a case in which the inner puff contains 20% of the mass as that of the outer puff. In this example, there is no tilt to the outer puff. It can be seen that the length of the 50% contour is roughly 1.5 cm while the 25% contour is over 2 cm in length. The central portion of the inner contour is also centered lower in Z than the case discussed above. It has been seen in these runs that when the expansion angle of 20 degrees is used in the inside puff, the tilted outside puffs tend to be better centered in Z. However, the overall length along Z does not necessarily correlate with tilt.

In contrast, Fig. 2(c) shows a case in which there is no expansion of the inner puff. Expansion of the inner puff may be controllable with proper nozzle design. The use of no expansion represents a somewhat idealized case. All other parameters are the same as those of Fig. 2(a). Without the expansion, the central puff is more elongated and uniform along Z providing for a more uniform density distribution. In fact, the length of the inner contour extends well over 2 cm along the center of the pinch.

Finally, Fig. 2(d) shows temperature contours corresponding to the example shown in Fig. 2(b). In this particular instance, temperatures of only 300-500 eV were reached during the implosion in the regions shown in Fig. 2(b). In other cases, temperatures as high as 800 eV have been seen but not under the optimal density conditions displayed in Fig. 2. In any case, the temperature may be somewhat suspect because of the crude ionization and thermal energy partition employed in these 2D runs. What can be seen in the plots is that the temperature gradient is at least as smooth as the density gradient. This implies that the radiative output

should be nearly uniform in this region. Whether this produces increased yields of hard K-shell radiation is yet to be determined. It may increase the total yield, however.

Conclusion

The hydrodynamic simulations presented here indicate that regions of relative uniformity can be produced in Z-pinch implosions. Lengths of up to 2 cm in the Z direction at a density equal to 50% of the peak implosion density have been demonstrated within the context of these simulations. Temperature gradients are also seen to have long scale lengths in these regions.

Although radiative yields were not themselves investigated in this study, the implication is that certain nozzle designs can produce large spatial regions at implosion which would lead to radiative outputs more peaked in time. Hence, higher radiative power levels can be produced for a given total yield. It is also probable that greater total yields will result from the more uniform implosions.

REFERENCES

1. R. W. Clark, J. Davis, and F. L. Cochran, Phys. Fluids 20, 1071 (1986).
2. Advanced Concepts Theory Annual Reports 1983, 1984, 1985. NRL Memorandum Reports 5094, 5330, 5590.

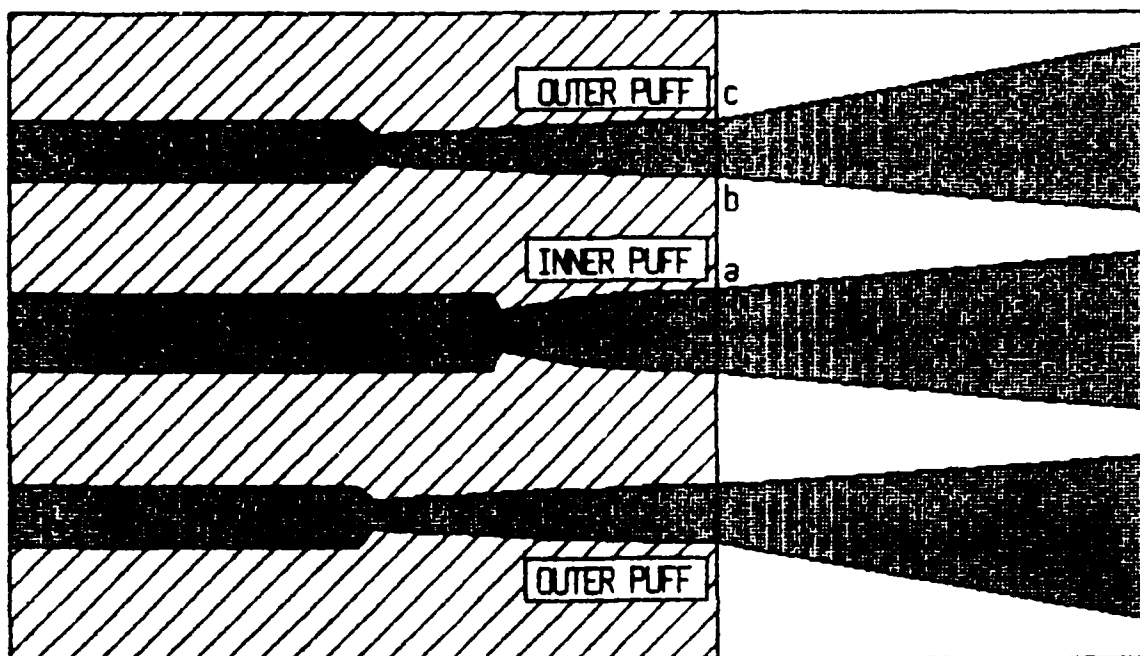
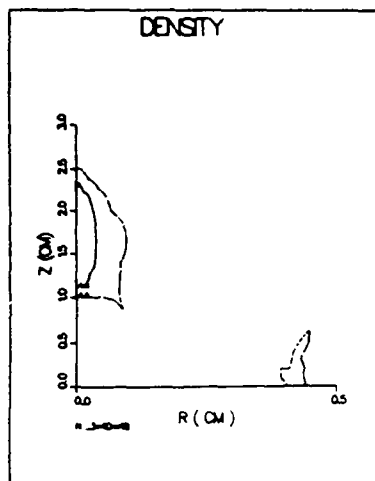
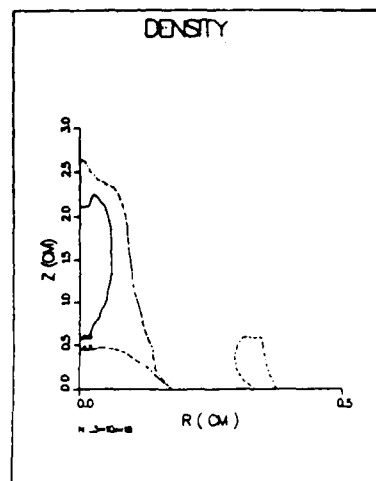


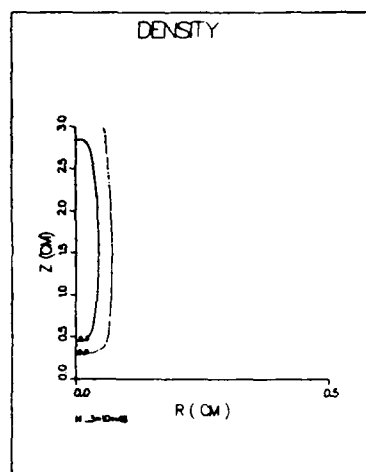
Figure 1. Schematic of the double-puff nozzle design. (a) radius of the inner puff, (b) inside radius of the outer puff, and (c) outside radius of the outer puff. The angular expansions are shown by the lines drawn from points a, b, and c to the anode (right hand side of the figure). In this figure no tilt is shown for the outside puff.



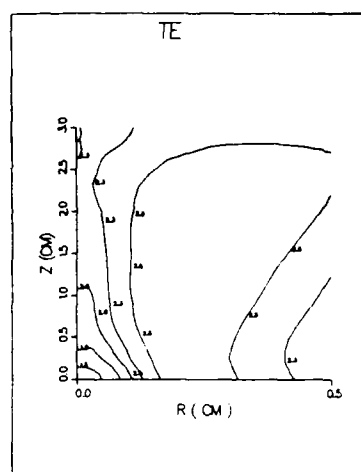
a



b



c



d

Figure 2. Density contours for double-puff configurations near the time of implosion. (a) Inside mass 80% of the outside mass and initial tilt of 5 degrees of the outside puff. The total outside mass is 375 gm. (b) Inside mass 20% of the outside puff and no tilt of the outside puff. The total outside mass is 390 gm. (c) Same as (a) but with no expansion of the inside puff. (d) Temperature contours for the case shown in (b). Density contours for the case shown in Fig. 2, but with no expansion along Z for the inside puff.

Section E. Opening Switch and Diode Modeling

Gyrokinetic Propagation Studies

The behavior of collisionless peripheral plasma around PRS loads or in the highly magnetized regions of VOS devices represents a crucial area in one's physical understanding of the power flow in such devices. In the radial transmission line, particularly, the existence of a tensor pressure, and the rapid radial acceleration and compression of guiding centers forces a very complex "Ohms Law" on the plasma medium in the collisionless limit. As a prelude to examining the detailed microstability of such plasmas, a one dimensional radial propagation study has been undertaken in 1986.

The propagation calculation has two major goals:

- (i) to assess the transmission, reflection, and absorption properties of collisionless gyrokinetic plasmas in a radial transmission line, and,
- (ii) to determine the situations where microinstabilities are likely modes of plasma turbulence in the tenuous regions.

The propagation computation is summarized below and in prior work. Owing to the virulently nonlinear character of the current density in the gyrokinetic limit, the studies required to reach the first of these goals are still ongoing. However those results fall into place, the qualitative behavior of the field profiles which thereby emerge has begun to shed some light on the second objective.

This calculation rests on four major elements:

- (i) a smooth set of radial mass density, magnetic and electric field profiles; consistent with
- (ii) a profile of mean perpendicular kinetic energy density determined by a Fokker-Planck calculation of the "driftaway" process;
- (iii) an exterior and interior circuit model delivering energy to the annular gyrokinetic plasma; and
- (iv) a fully implicit, fully electromagnetic, 1-D Lagrangian method of lines solver for the field and fluid equations which advances the guiding center drift speed and the fluid Jacobian equivalent to Ampere's and Faraday's Laws in the collisionless gyrokinetic system.

Each of these elements will be discussed and some general, but preliminary conclusions reported.

Exact separable implosion with $p_{\perp} \neq p_{\parallel}$.

For special initial conditions there exist exact solutions to the gyrokinetic moment equations that describe strongly magnetized plasma in the periphery of a z-pinch. An isotropic pressure implies that the collisions are sufficient to keep the velocity components randomized. This, then, implies a finite conductivity, in contrast to the assumption of infinite conductivity which demands a collisionless plasma. However, as the plasma gets closer to the axis in a cylindrical geometry the pressure $p_{||}$ parallel to the magnetic field $B = B_\theta(r)$ increases as $1/r^2$, while the perpendicular pressure p_\perp increases as $1/r$. In fact, in any curvilinear magnetic field an isotropic pressure is strictly speaking inconsistent with infinite conductivity.

The fluid equation of motion in the radial direction, for an anisotropic pressure, includes an centrifugal force $L_{||}^2/r^3$ that reflects the conservation of angular momentum,

$$\rho \frac{DU}{Dt} = \frac{\rho L_{||}^2}{r^3} - \frac{1}{r} \frac{\partial(r\rho B W_\perp)}{\partial r} - J_z B. \quad (1)$$

The macroscopic quantities that enter into the moment equations are averages over the particle distribution function. Without collisions the distributions are not necessarily maxwellian, but the exact functional form is unknown. Instead of the distribution in terms of the velocity components in cylindrical geometry $f(r, \mathbf{v}, t)$ it is better to use the distribution function in terms of the dynamical invariants, the magnetic moment μ and the angular momentum P_θ . The two equivalent forms of the distribution function are connected by

$$f(r, \mathbf{v}, t) = \left[\frac{m^2 r}{2\pi B(r, t)} \right] n(r, t) F(\mu, P_\theta, r).$$

The factor in $[\dots]$ is the Jacobian in the velocity space transformation to μ and P_θ . Without collisions the invariants for each particle do not change, and the distribution function F is constant in time. The particle density $n(r, t)$ is no longer part of F , which is normalised as

$$\left[\frac{m^2 r}{2\pi B(r, t)} \right] \int d\mu dP_\theta F(\mu, P_\theta, r) = 1,$$

for both electrons and ions. With the assumption of quasineutrality the mass density ρ is $\rho = (m_{\text{electrons}} + m_{\text{ions}})n(r, t)$.

The parallel pressure is

$$\rho L_{||}^2 = \int d\mu dP_\theta F P_\theta^2 / m^2,$$

and the perpendicular pressure becomes

$$\rho W_\perp = \int d\mu dP_\theta F \mu / m,$$

with a summation over species implied.

Equation (1) with vanishing angular momentum, $L_{||} = 0$, yields¹ a selfsimilar solution, but it turns out that even for non-zero $L_{||}$ a whole class of self-similar solutions are possible. The one highlighted here is relevant for electromagnetic propagation modeling.

Henceforth the dependent variables $B, \rho, L_{||}, W_{\perp}$ and their derivatives are functions of the single selfsimilar variable $\xi = r/a(t)$, where $a(t)$ is a typical scale length that contains the sole time dependence. Then Eq. (1) becomes

$$\frac{d^2\alpha}{dt^2} = \frac{\omega_{||}^2}{\alpha^3} + \frac{\omega_{\perp}^2}{\alpha^2} - \frac{\omega_A^2}{\alpha}, \quad (2)$$

where $\alpha(t)$ is the normalized scale length $\alpha(t) = a(t)/a_0$.

Here $\omega_{||}^2(\xi) = L_{||}(\xi)/\xi^4$ depends in general on the spatial variable ξ , and Eq. (2) does not separate. Separation is feasible only when the initial angular momentum is proportional to (radius)⁴, i.e. $\omega_{||}^2$ is constant. Recall that $L_{||}^2$ is an average of $P_{||}^2$, where $P_{\theta} \sim v_{\theta}r$ is the particle angular momentum. Since $v_{\theta} \sim \omega_{\theta}r$ also $P_{\theta} \sim \omega_{\theta}r^2$: constant $\omega_{||}^2$ then implies a parallel temperature $\propto r^2$.

The perpendicular pressure term gives rise to

$$\omega_{\perp}^2 = -\frac{1}{\xi^2\rho} \frac{\partial [H_{\perp}(\xi)\xi\rho]}{\partial \xi},$$

which should no longer be a function of ξ . In this term the spatial dependence of the density $\rho(\xi)$ can be played off against the perpendicular thermal energy $H_{\perp}(\xi) = B(\xi)W_{\perp}(\xi)$. Either ρ or H_{\perp} can be chosen freely. It is easiest to separate the spatial dependence in H_{\perp} by setting $H_{\perp}(\xi) = H_0/g(\xi)$. The mass density is then

$$\rho = \rho_0 \frac{g(\xi)}{\xi} \exp \left[- \int_1^{\xi} dx x g(x) \right].$$

The acceleration term contains the magnetic field through ω_A , which is the transit frequency of an Alfvén wave through the pinch' scale size a_0 , $\omega_A^2 = B^2/4\pi\rho a_0^2$. A constant ω_A^2 then implies a specific magnetic field, in terms of $g(\xi)$:

$$\frac{d(\xi B)^2}{d\xi} = (B_{\infty}^2 \xi^2 g(\xi)) \exp \left[- \int_1^{\xi} dx x g(x) \right],$$

where $B_{\infty}^2 = 4\pi a_0^2 \omega_A^2 \rho_0$, the magnetic field at the characteristic distance a_0 . This equation also defines the total current enclosed by the pinch within a distance ξ , because $\xi B = 2I(\xi)/ca_0$.

The function $g(\xi)$ is arbitrary within restrictions defined by certain physical requirements. One is that the density ρ be positive and finite everywhere, another is that the various ω^2 's be positive. The choice here is $g(\xi) = \xi^2$, which satisfies all these requirements. With this special form for $g(\xi)$ the various integrations give rise to known functions. For example, the density becomes

$$\rho = \rho_0 e^{1/4} \xi \exp(-\xi^4/4),$$

where ρ_0 is given by the mass per unit length within ξ , $\lambda(\xi)$, through

$$\lambda = 2\pi a_0^2 \rho_0 W_{1/4}(\xi),$$

where $W_{1/4}(\xi)$ is the incomplete gamma-function of order $1/4$. Likewise, the current carried by the corona enclosed within ξ becomes

$$I^2(\xi) - I^2(0) = B_\infty^2 e^{1/4} \int_0^\xi dx x^4 \exp(-x^4/4),$$

where $I(0)$ represents the current carried by a collisional pinch located on axis.

In any particular circuit characterized by the current risetime and the interior resistance of the bulk plasma load, one can use the results of the Fokker-Planck calculation to establish a scale sound speed H_o for the selfsimilar startup profiles, using the initial voltage and normalized magnetic field Ω implied in any circuit model.

Shown in Figure 1 is the variation of $H_o = H_\perp / H_{\perp,init}$ with the parameter $(E/E_D)/(\Omega t_o)$ at $30 t_o$ (collision times) for some 190 combinations of E/E_D and Ωt_o . The clearly one dimensional variation of the Fokker-Planck result is not manifest *a priori*, but it certainly helps reduce the effort in scanning initial conditions. Shown in Figure 2 is an initial condition profile derived from these considerations.

Collisionless current density.

In a collisional plasma the collisions are the dominant influence that balances the motion of the plasma electrons against the acceleration by the electric field. The resulting collisional electron drift, and thus the current density j , is proportional to the electric field E , $j = \sigma E$. The electrical power input into the plasma ends up in increased random velocities of the plasma particles, Ohmic heating.

Even in the absence of collisions the magnetized plasma in the z-pinch' periphery can absorb energy from the electrical pulse. In this case the energy does not go into random motion of the plasma particles, but instead is put into organized motion. A strongly magnetized plasma in an electric field is not accelerated by the field, but drifts with a

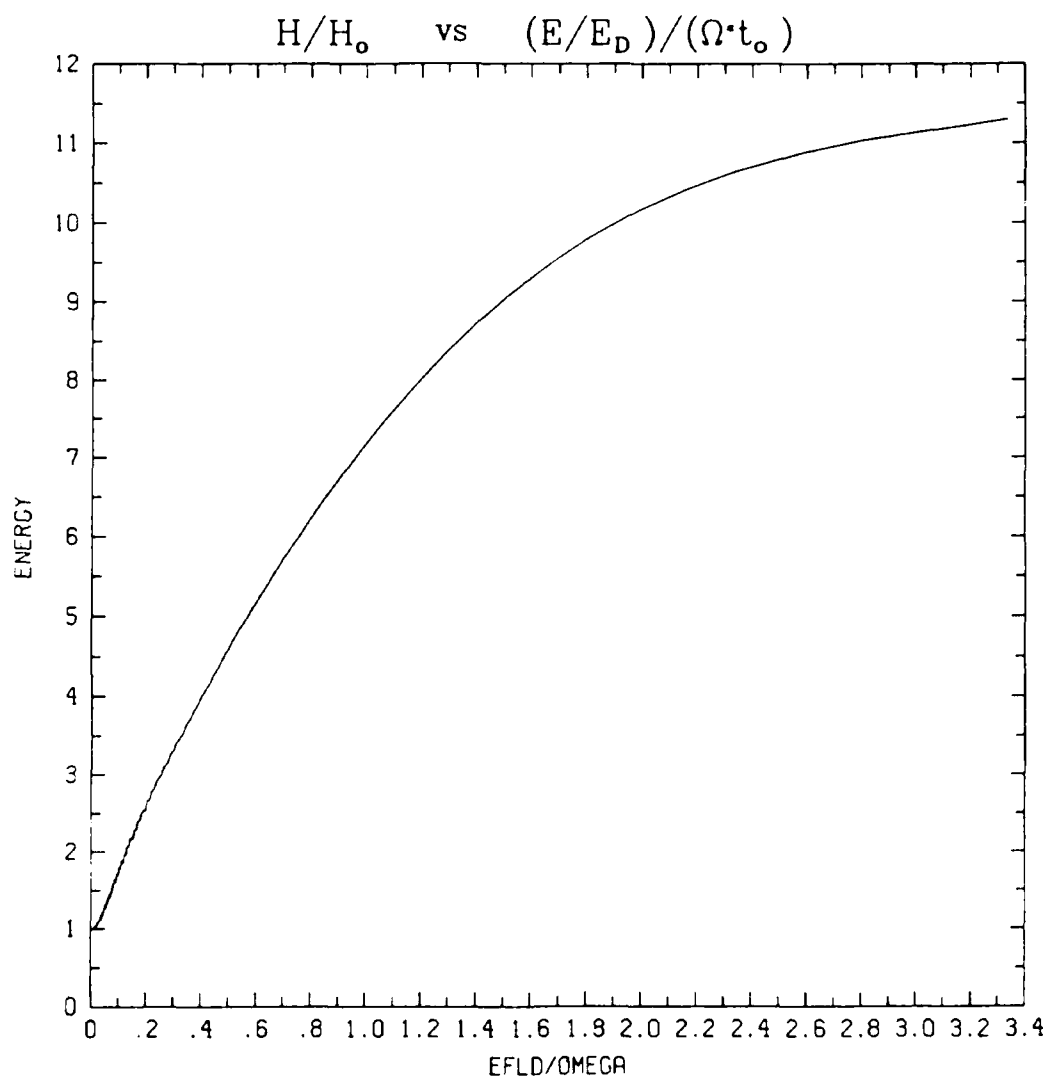


Figure 1. Energy vs. E/Ω .

U B N E

R 7.15E-03 G 6.64E+03 M 0.78 C 14.

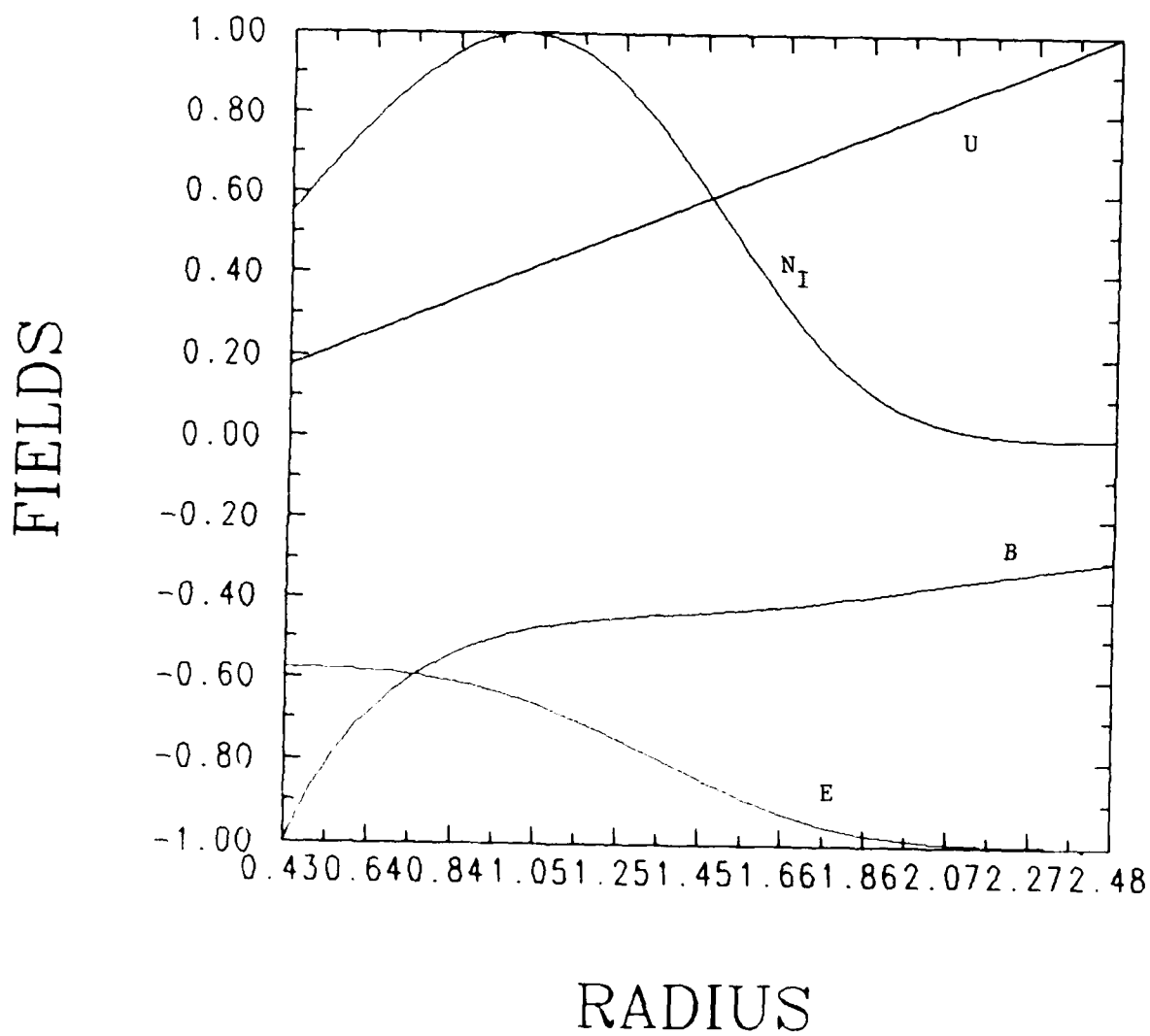


Fig. 2. Typical initial conditions.

velocity $v = E/B$. For constant E the energy remains constant, but when the electric field increases in time the plasma accelerates. The kinetic energy density ρv^2 increases also (ρ is the plasma's mass density), and electrical power is absorbed. Likewise, electrons that $E \times B$ drift into a region of increased magnetic field spin up, increasing their perpendicular energy w_\perp in their effort to keep the magnetic moment $\mu \sim w_\perp/B$ constant. The increase in w_\perp , or the increased magnetization, is another power sink. In a cylindrically symmetric geometry with $B \sim 1/r$ the particle's angular momentum about the axis, $P_\theta = mrv_\theta$, is conserved: a drift toward the axis increases the kinetic energy parallel to the magnetic field w_\parallel as $1/r^2$.

The axial current density, calculated either by momentum balance or by averaging of nev_z , is then

$$j = \frac{\rho c^2}{B} \frac{D(E/B)}{Dt} + \frac{c}{B} \left[\frac{\rho L_\parallel^2}{r^3} - \frac{1}{r} \frac{\partial(r\rho B W_\perp)}{\partial r} \right]. \quad (3)$$

The first term is related to the acceleration of the $E \times B$ drift motion, the second comes from angular momentum conservation, or p_\perp , and the third is the magnetization contribution, from p_\parallel . In the acceleration term the ions dominate; the electrons are more important for the two pressure-derived terms, particularly in the general case without thermal equilibrium between electrons and ions.

Electromagnetic energy transport through the corona.

What fraction of the input power pulse passes through the collisionless but energy-absorbing plasma corona? The transmission coefficient T is the power reaching the central, collisional load at some inner boundary, $S_i = 2\pi r_i(\mathbf{E}_i \times \mathbf{B}_i)$, and the power coming in through the outer boundary, S_b , i.e.

$$T = S_i/S_b = \frac{E_i B_i r_i}{E_b B_b r_b};$$

the absorption coefficient is $A = 1 - T$. While the inner boundary is nearly stationary, the outer boundary is moving with the plasma, $r_b = r_b(t)$. Motion of the plasma's outer boundary changes the volume of the vacuum between the plasma and the power inlet. The magnetic field energy in this vacuum changes correspondingly. The transmission efficiency of the corona plasma including the outside vacuum is then defined as $\epsilon = S_i/S$, where S is the total power transmitted through the inlet.

Toward the inlet the corona plasma goes over smoothly into hard vacuum, while on the other side the plasma becomes denser until the collisions begin to dominate. This is where the central pinch starts. The inductive approximation, $\partial E/\partial t \ll 4\pi j$, is invalid in the outer region without plasma; a proper transition between regimes then demands that this term be kept also in the corona regime. The current density in Eq. (3) implies that the magnetic field moves with the plasma, suggesting that a Lagrangian coordinate system fixed in the fluid may simplify the computations.

The Lagrangian radial coordinate $R = R(\xi, \tau)$ evolves from the coordinate ξ at time $\tau = 0$ according to the implicit relation $dR/d\tau = -U(R, \tau)$, and R is

$$R(\xi, \tau) = \xi - \int_0^\tau d\tau' U(R, \tau'),$$

A fluid element $d\xi$ changes according to the Jacobian $J = dR/d\xi$, where $DJ/D\tau = -\partial U(R, \tau)/\partial \xi$.

Magnetic flux conservation requires $\int B \xi d\xi$,

$$B(R, \tau) = B(\xi) d\xi/dR,$$

The mass in a shell ($\rho R dR$) is conserved, whence

$$R\rho(R, \tau) = \xi\rho(\xi) d\xi/dR.$$

From these relations the Alfvén speed $c_A^2 = B^2/4\pi\rho$ transforms as

$$c_A^2(R, \tau) = c_A^2(\xi) d(\ln \xi)/d(\ln R).$$

In terms of the normalized plasma velocity $U = E/B$ Ampere's law becomes

$$\frac{D U}{D \tau} = \left[\frac{B}{R} + \frac{\partial B(1 - U^2)}{\partial R} - j_p \right] / K_A^2 B.$$

Here $K_A^2 = 1 + c^2/c_A^2(R, \tau)$ determines the wave speed c/K_A : without plasma, $c_A \rightarrow \infty$, and K_A becomes unity, for a wave speed c . K_A becomes c/c_A in the opposite case, the wave speed is c_A , and the inductive approximation is valid.

The current density j_p is the part of the current density in Eq. (3) coming from the particle pressure, i.e. the current density without the contribution from accelerating the plasma drift:

$$j_p = \frac{B}{R^3} \frac{W_{||}}{c_A^2} - \frac{B W_{\perp}}{W_{||}} \frac{\partial [\rho B W_{\perp} (d\xi/dR)]^2}{\xi \rho B W_{\perp}} \frac{\xi}{R} \frac{dR}{d\xi}.$$

The particle pressure-related terms $W_{||}(\xi)$ and $W_{\perp}(\xi)$ are determined by the selfsimilar solutions at $\tau = 0$ (cf. Fig. 2), and these are used as initial conditions.

The exterior boundary condition comes from the electromagnetic wave driving the plasma. Typically the electric field is connected to some pulse power device, cf. Figure 3, which should in principle be influenced by the load. The interior boundary condition is determined completely by the axial resistance, viz.

$$U_{<} = R_{<} \frac{R_{Load} l_o^2}{2 Z_D t_o};$$

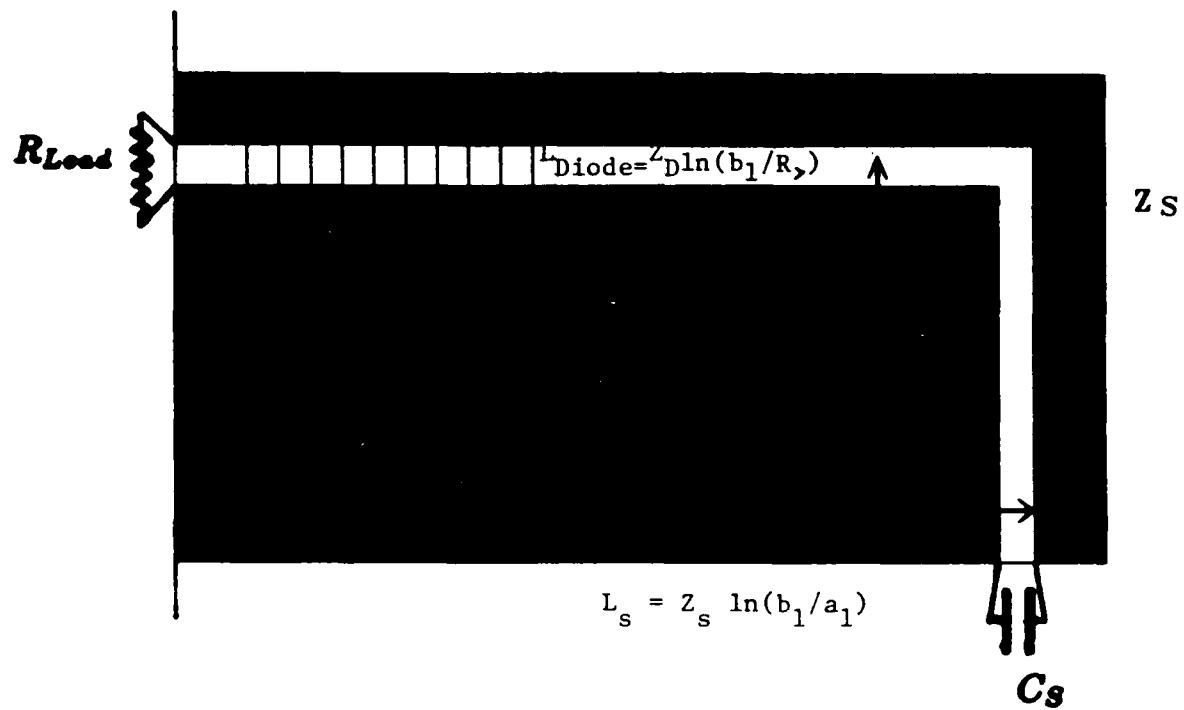


Figure 3. Diode, Transmission Line and Circuit Geometry

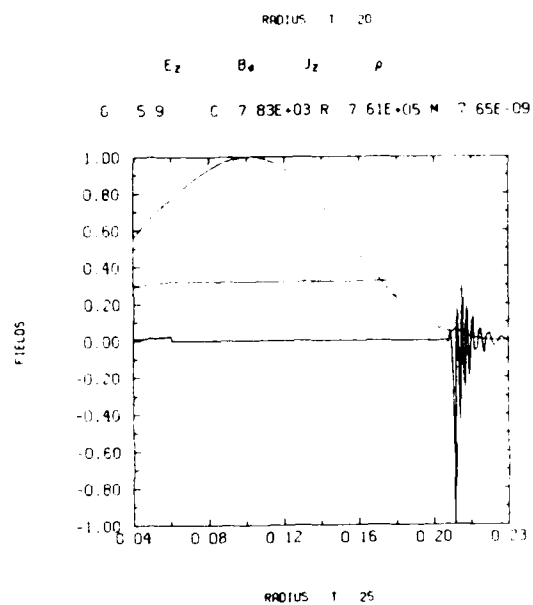
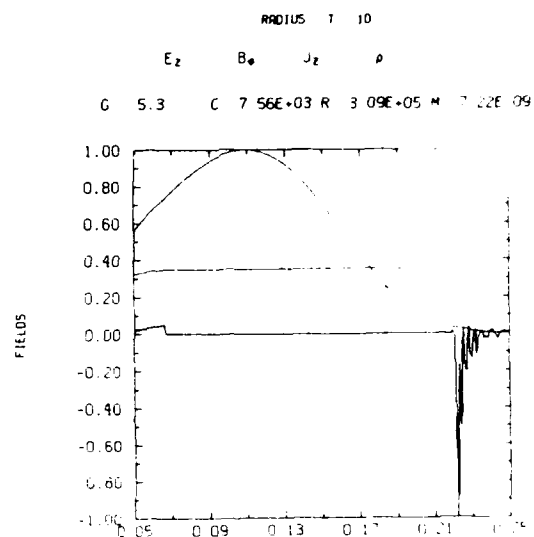
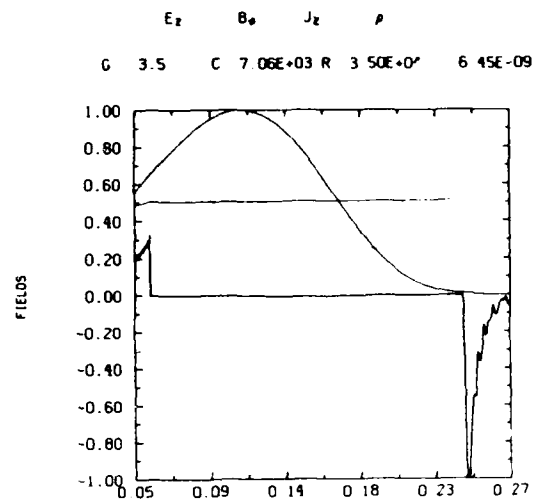


Figure 4. Gyrokinetic Field Evolution

while the exterior condition is posed as an alternative acceleration formula,

$$K_A^2 \frac{D U}{D \tau} = f(V_S, L_{Diode}, L_S, R_>, Z_D),$$

with the circuit current I_S and voltage V_S determined in the usual way. The derivation of this circuit equation presumes continuity in the line impedance at the plasma vacuum interface; the next level of approximation is to relax this constraint and go to a transmission line model. The capacitance and inductance of the circuit model then set the circuit risetime; a reasonable risetime domain is $t_0 = (10, 50) \text{ ns}$.

Shown in Figure 4 is a typical time development of the plasma electric field, magnetic field, and current density as a 50 ns risetime pulse is impressed on the gyrokinetic corona. The energy is not absorbed gracefully; the plasma current density in Fig. 4c shows wiggles, which are TEM waves (apparently analogous to magnetosonic MHD modes) that are excited by the relatively sudden application of the electric field. For low values of H_0 the profiles change little over time, and the electric field is easily transmitted. For larger values, e.g. $H_0 = (7.0 \cdot 10^6)^2 \rightarrow T_e = 20 \text{ eV}$, the electric field is heavily modified and the input power is substantially attenuated by the corona.

Summary and conclusions.

Current can be lost in the periphery of a z-pinch by various mechanisms. Initially the z-pinch carries no current, and the inductive voltage at the edge of the cathode away from the pinch material can drive a current in free electrons. The free electrons can be the bulk of the current at the very start, but this current is cut off rapidly once the current starts flowing through the z-pinch.

The tenuous plasma outside the z-pinch can also carry current. As a remnant of background gas or perhaps the edge of the injected gas column in a puff-gas z-pinch, this plasma is not well-specified either experimentally or theoretically. How much current is shunted through this plasma depends linearly on the plasma density, and also on parameters such as the temperature and the magnetic field in the periphery, i.e. the current in the main z-pinch.

The plasma temperature in the periphery at the end of "driftaway" is computed from a simplified Fokker-Planck analysis, assuming that the electron velocity remains isotropic through collisions with the ions. Plasma heating proceeds until the electron collision time is comparable to the pulse time, resulting in an upper temperature limit of about 50 eV (weakly dependent on plasma density).

The pressure of the collisionless plasma in the periphery becomes anisotropic as the plasma contracts toward the axis, due to the separate conservation of the electron's magnetic moment, and the electron's angular momentum about the axis. Under these conditions the plasma can still oscillate in a self-similar manner, and for constant z-pinch

current and balanced oscillation frequencies ($\omega_{\parallel}, \omega_{\perp}, \omega_A$) the periphery can be in an exact equilibrium.

As the current increases in the power pulse part of its energy is siphoned off by the periphery. Exactly what fraction is lost depends upon the detailed structure of the low density plasma corona, which is as yet poorly understood. For a tenuous periphery, $n \leq 10^{13}/cm^3$, with the corresponding temperature, $T \sim 5.0eV$, little power is diverted from the z-pinch. For densities appropriate to edge gas, $n \sim 10^{15}/cm^3$, or higher temperatures $T \sim 50eV$, the power loss is substantial.

References.

1. F. S. Felber, Phys. Fluids **25** 643 (1982).
2. I. B. Bernstein and P. J. Catto, Phys. Fluids **28** 1342 (1985)

PEOS Simulations with MAGIC.

Particle simulations^{1,2} of erosion switches have been notably divergent from the laboratory experience in several respects. The primary objectives of the work described here are: (i) to substantiate, modify or critique the earlier and contemporary simulations (in Ref. 1,2) in the context of the DNA e/m PIC code MAGIC; (ii) extend the parameter domain of the simulations in order to document fully the implications of e/m PIC codes for PEOs; and (iii) to provide a comparison basis for evaluating the newer simulation codes, and novel algorithms e.g. the magneto-inductive PIC code, or particle collision schemes. To these ends a sequential upgrade of the PEOs study due to Grossman¹ has been undertaken with MAGIC. The progression has been (i) planar transmission line with H^+ ions at 10^{12} cm^{-3} and no radial drift, (ii) cylindrical geometry, and C^+ ions at 10^{12} cm^{-3} , and (iii) C^+ ions with a radial drift $\sim 2 \times 10^8 \text{ cm/sec}$. The planned continuation is to vary the density drift-velocity product, diagnose the axial momentum deposition and the electron temperature, and explore more realistic (BJ5- like) downstream loads.

A useful comparison of the MAGIC simulation to date with those of Grossman, et. al (his fig. 2,3,4) can be drawn between the second and third cases above. For these comparisons the geometry of the region is shown in Fig. 5. The peak current input to the switch is 156 kA over 5 ns, and the opening time (saturated load current) for case (ii) is larger than 10 ns. This is a somewhat slower opening, and the ion mass distribution is more snowplowed when the anode influx is shut off. The current channel remains narrow, however, and the anode end leads the cathode end, in a manner similar to the Grossman calculation. A sequence of MAGIC plots is shown in Fig. 6,7. Figure 6 shows the rB_θ contours, while Figure 7 displays the ion distribution in space at 2.5, 5.0, 7.5, and 10.0 ns during the switching action.

The mechanism of current channel formation and switch opening shown here is thus quite similar to that depicted by Grossman et. al although the interpretation is subject to some honest controversy. A central point is the $E \times B$ drift and its relation to the current channel, and also the role of ion drift in determining the opening time and peak current. A fair summary of the case (ii) MAGIC simulation, in which ion drift and regeneration at the anode are absent, is that the incoming axial momentum of the power pulse is coupled to a small fraction of the plasma load ions through a shock-like structure of charge separation, a momentum transfer front. At this charge separation, the confluence of the charge density ρ and the $E \cdot B$ drift produces the current density in the switch, c.f. Fig. 8. The opening is forced when the momentum transfer front runs downstream of the switch plasma, causing the active, charge carrying $E \cdot B$ contours to be only those nearest the cathode. One can view this process as representing the completion of the magnetic insulation process in the cathode sheath. The downstream E_r still peaks near the anode rather than near the cathode as occurs upstream, due to the neutralizing sheath space charge. The erosion of ion density upstream of the momentum transfer front plays a very weak role in the process here, when the radial ion drift is set to zero; and the opening time is notably slower than for the Grossman computation.

When the ion drift ($\sim 2 \times 10^8 \text{ cm/s}$) is now turned on, case (iii) the opening time is cut by 40% to about 6 ns as shown in Fig. 9, 10. This drifted 10^{12} cm^{-3} carbon plasma is thus opening almost as fast as Grossman's more slowly drifting ($1.89 \times 10^8 \text{ cm/s}$) hydrogen plasma at a somewhat lower current level (100kA).

It is common in experiment³ to see a wider current sheath, but the MAGIC run gives a possible clue to a partial resolution of this problem when current density streamline plots and range plots are examined. One finds circulating currents upstream of the momentum transfer front, such that an axial B_θ profile at fixed r would see a slightly non-monotone decay in B_θ with increasing z . Experimental probe measures also hint at such behavior, but no claim is yet made as to whether or not such reversals are in fact resolved by the experiment. If vortices of current density are in fact present, e.g. through gyrokinetic modes upstream of the momentum transfer front, then an apparent broadening of the current sheath would occur – even though such current is not connected to the driving circuit.

The theory of operation of PEOS devices is thus somewhat confused and likely to remain so for a time. If the e/m PIC method can show its relevance in accounting for the observed coupling of ion drift speed and opening time⁴, and if better resolution of the current channel structure can be obtained, then a detailed theoretical accounting of the required collisionality to broaden the current channel properly would be a logical step. The means to this assessment and the application of more appropriate magnetoinductive simulation methods for long time scale conduction phase operation are therefore among our primary near term goals.

References

1. Numerical Simulation of a Low Density Plasma Erosion Opening Switch, J.M. Grossman, *et. al.* NRL Memo Rep. **5724**, 1986
2. E.M. Waisman, *et. al.* Appl. Phys. Lett. **46** (11), 1985
3. D.D. Hinshewood, *et. al.* Appl. Phys. Lett. **49** (1635) 1986
4. R. J. Commisso, *et. al.* NRL M.R. **5560**, May 1985

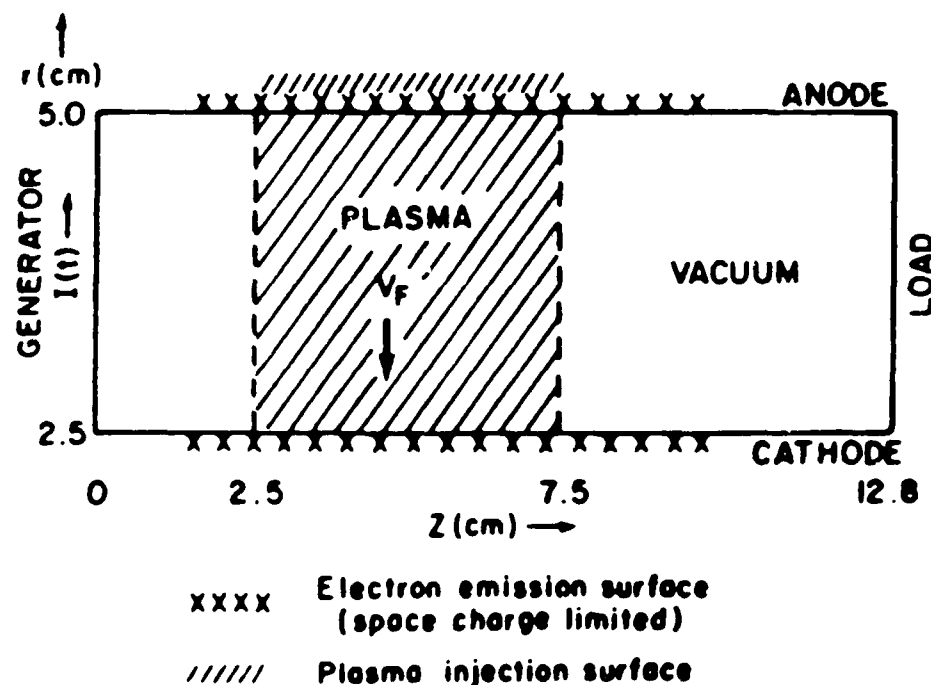
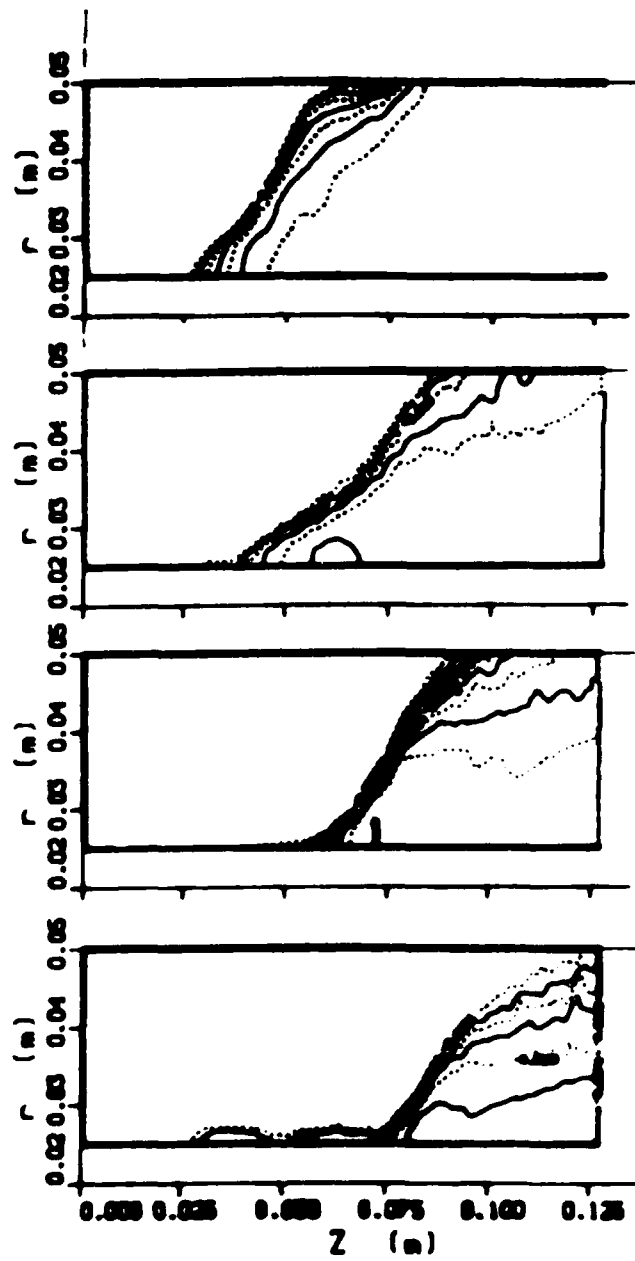


Figure 5. Geometry for the MAGIC PIC Simulations of the PEOS



6. Contours of rB_0 for drift velocity $v_D = 0$

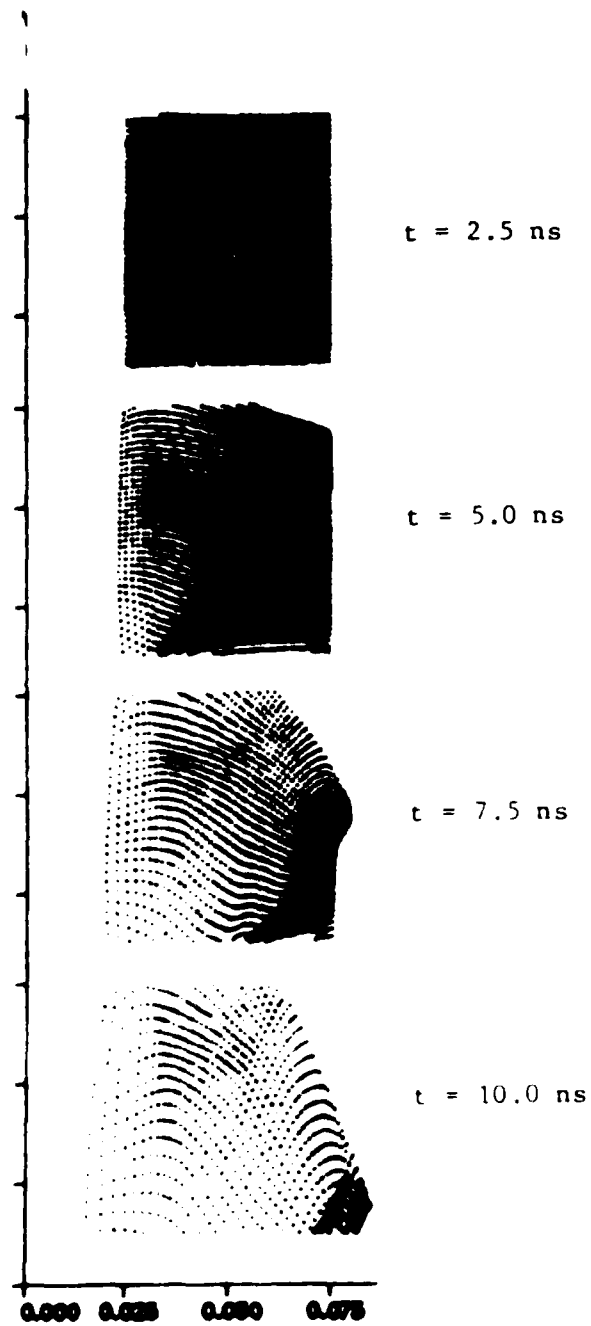


Fig. 7. Ion distribution for drift velocity $v_D=0$.

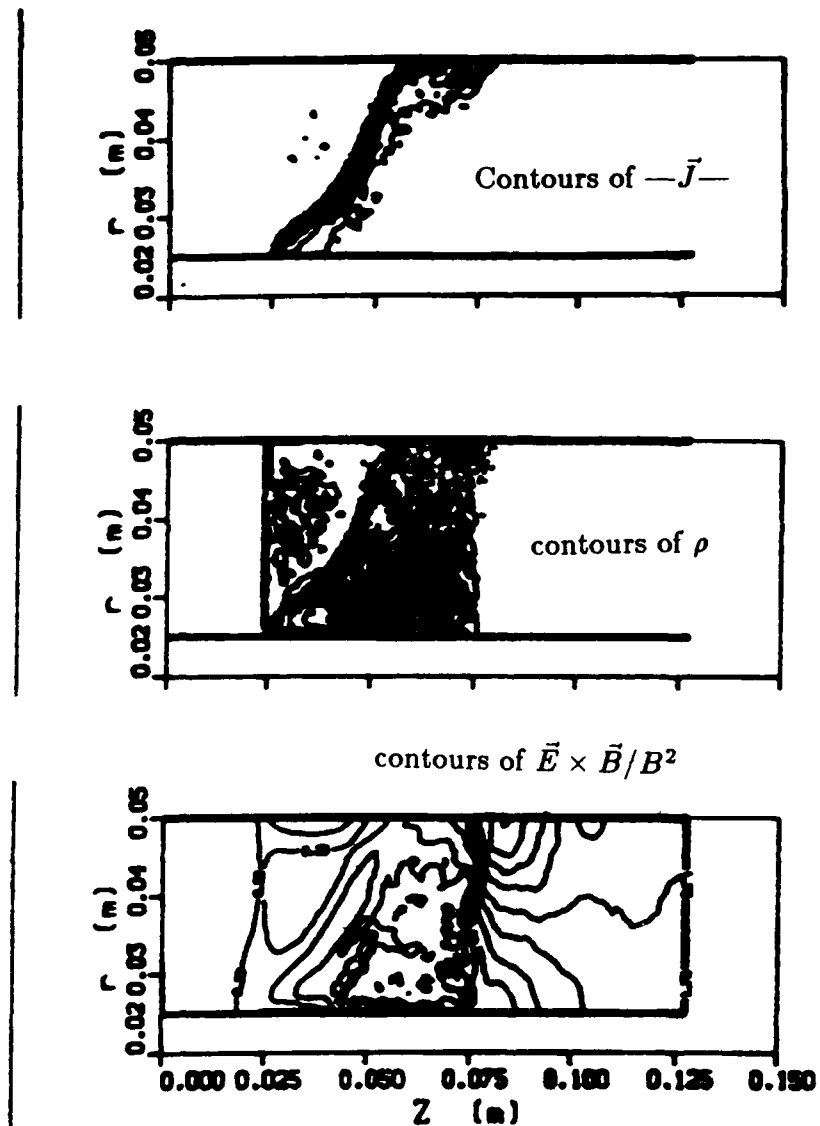


Fig. 8. Momentum transfer front at 2.5 ns for drift velocity $v_D=0$.

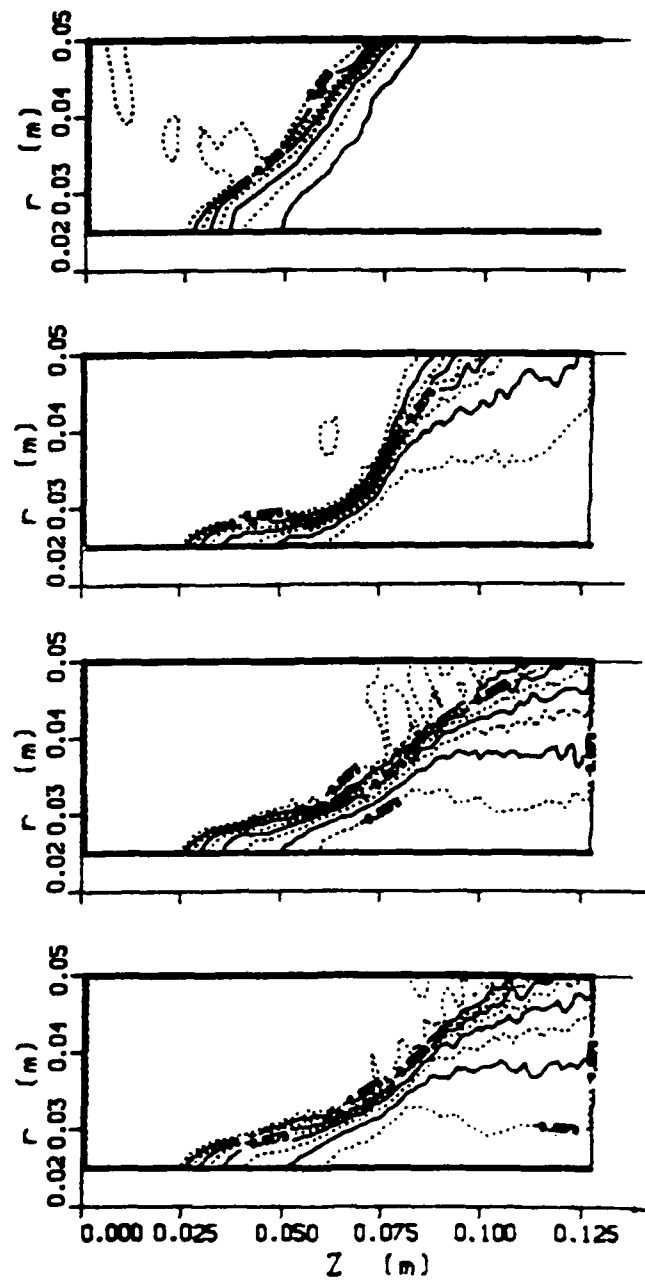


Fig. 9. Contours of $rB\theta$ for drift
velocity $V_D = 2.0 \times 10^8 \text{ cm/s}$

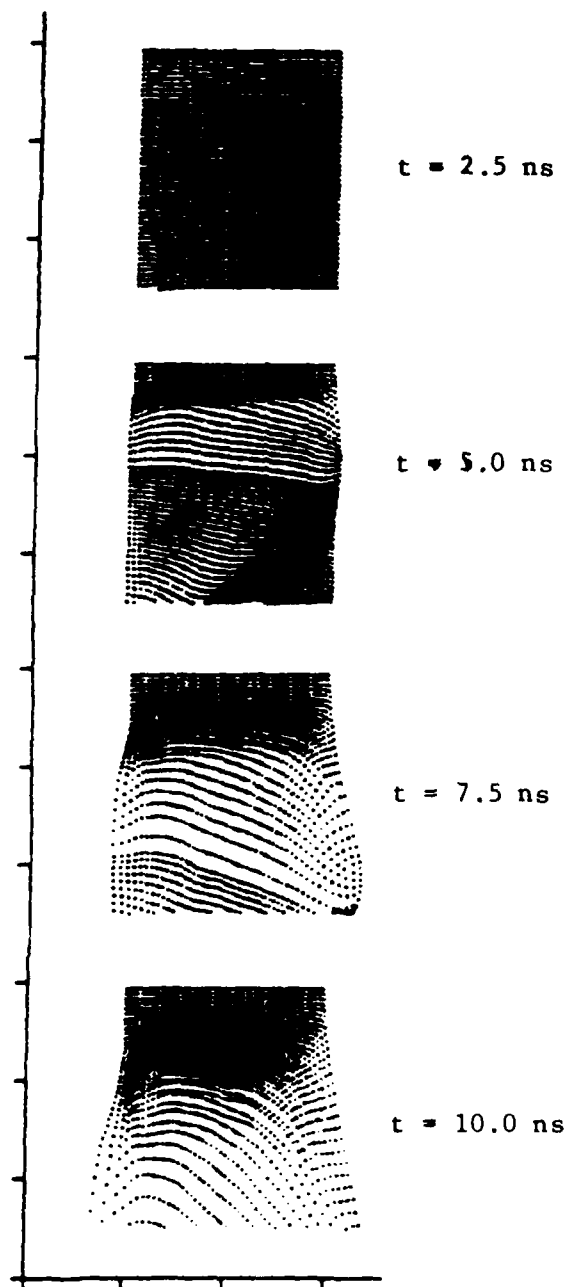


Fig. 10. Ion distribution for drift
velocity $V_D = 2.0 \times 10^8 \text{ cm/s}$.

I. Magnetoinductive Particle-in-Cell Code Development

This past year's report describes the progress towards the utilization of Darwin's¹ magnetoinductive model for a particle simulation code. The magnetoinductive model is desirable because it retains an induced electric field while not including light waves. This approximation relaxes what can be a severe constraint on the time step and must be examined in pulsed-power applications like the VOS. The intent of any VOS is the storage of energy over a long time frame (as measured in electromagnetic signal transit times) and then the release of this energy over much shorter times, more like the electromagnetic transit time, through the interruption of a current path. Under such conditions the displacement current cannot be neglected at the time of opening, but it cannot be allowed dominance during the conduction phase because it makes the calculation too stiff. The Darwin limit retains that part of the displacement current needed to resolve the interruption and also removes the primary source of stiffness - the traveling waves.

However solving for the magnetic and the electric fields becomes more difficult in this limit. The magnetoinductive model requires knowledge of more information at the boundaries. Substantial progress has been achieved but difficulties still remain. The next section describes the magnetoinductive formulation and two different schemes for its implementation. Results from testing the model are described in Section III. The primary problems encountered relate to the specification and/or convergence of boundary conditions.

II. The Magnetoinductive Formulation

Particle-in-cell codes have proven themselves to be valuable tools in examining problems where the details of individual particle motion are important. Among the most useful and versatile of these tools are the fully electromagnetic particle codes. These codes feature a complete classical description of the electromagnetics and particle motion. The stability and accuracy of the codes require the time step to be sufficiently small to accurately resolve the propagation of light waves, the fastest cyclotron motion, and the fastest plasma waves. However there are numerous examples in the pulsed-power field where the vacuum wavelengths associated with a given electromagnetic pulse are much larger than the machine dimensions. For these cases, Darwin's magnetoinductive model of the electric and magnetic fields may be useful. The Darwin model neglects retardation effects in the transmission of information which has the effect of eliminating purely electromagnetic modes. It is no longer necessary to restrict the time step such that light cannot propagate more than the smallest computational cell in a time step. Another advantage of the magnetoinductive model is a decrease in the level of electromagnetic fluctuations. The enhanced particle fluctuations existing in a particle simulation can drive anomalously large fluctuations (and) of the electromagnetic fields. These fluctuations can dominate over the phenomena of interest.

A disadvantage of the Darwin model is that the solution for the electromagnetic fields requires solving the problem for the full set of Maxwell's equations. The approximation reduces the full Maxwell's equations to two coupled elliptic equations, i.e., elliptic equations for the magnetic vector potential and the electric and magnetic fields coupled to the particle equations. In the magnetoinductive model, the components of the electric and magnetic fields must be completely respected each time step. In contrast to the full set of Maxwell's equations a vector decomposition into longitudinal and transverse parts of the electromagnetic equations for the magnetoinductive model

$$\nabla \cdot \vec{B} = 0, \quad (1)$$

$$\nabla \cdot \vec{E} = \rho/\epsilon_0, \quad (2)$$

$$\nabla \times \vec{B} = \mu_0 \vec{J} + \frac{1}{c^2} \partial \vec{E}_L / \partial t = \mu_0 \vec{J}_T, \quad (3)$$

$$\nabla \times \vec{E}_T = -\partial \vec{B} / \partial t, \quad (4)$$

where the transverse and longitudinal fields by definition satisfy

$$\nabla \cdot \vec{E}_T = 0,$$

$$\nabla \times \vec{E}_L = 0.$$

This set of equations automatically satisfies the charge continuity equation

$$\partial \rho / \partial t + \nabla \cdot \vec{J} = 0.$$

The field equations in the magnetoinductive model differ only in the neglect of the partial time derivative of the transverse electric field in equation 3 from the full set of Maxwell's equations.

The solution for the transverse electric fields proves to be the most difficult task for the implementation of this model. An explicit time differencing of Faraday's law leads to violent numerical instabilities. This time differencing tries to propagate information at a finite speed which is inconsistent with the instantaneous Darwin model. The magnetic field is eliminated between equations 3 and 4 to obtain

$$\nabla^2 \vec{E}_T = \mu_0 \left(\frac{\partial \vec{J}}{\partial t} \right)_T. \quad (5)$$

where for nonrelativistic particles of species α :

$$\frac{\partial \vec{J}_\alpha}{\partial t} = \epsilon_0 \omega_{p\alpha}^2 \vec{E} + \frac{q_\alpha}{m_\alpha} \vec{J}_\alpha \times \vec{B} - q_\alpha \nabla \cdot \vec{P}_\alpha, \quad (6)$$

and where

$$\vec{P}_\alpha(x) = \langle n_\alpha \vec{v}_\alpha \vec{v}_\alpha \rangle.$$

Inspection of equation 6 exhibits the difficulty in solving for the transverse electric field. The time derivative of the current is also a function of the transverse electric field that we are trying to solve. The combination of equations 5 and 6 yields an equation of the form.

$$\nabla^2 \vec{E}_T = \left[\frac{\omega_p^2(x)}{c^2} \vec{E}_T + \mu_0 \vec{S} \right]_T. \quad (7)$$

It is important to notice that equation 7 features a vector decomposition on the right hand side of the equation. This vector decomposition is analytically performed by a volume integration of the vector (c.f. Jackson²). Equation 7 forms an integrodifferential equation that is very difficult to solve directly. Instead we resort to iterative methods.

A standard way of solving equation 7 suggested by Nielson and Lewis³ incorporates the subtraction of a constant times \vec{E}_T from both sides. This constant is chosen as some mean value of the term multiplying \vec{E}_T on the right side of equation 7.

$$\left(\nabla^2 - \mu_0 \frac{\bar{\omega}_p^2}{c^2} \right) \vec{E}_T = \left[\frac{(\omega_p^2(x) - \bar{\omega}_p^2)}{c^2} \vec{E}_T + \mu_0 \vec{S} \right]_T, \quad (8)$$

where $\bar{\omega}_p^2$ is a constant. An iterative procedure is followed in which the previous iteration value of \vec{E}_T is used on the right hand side of equation 8 to find the current iteration value of \vec{E}_T . The transverse projection in equation 8 is performed with the aid of the continuity equation in the following way:

$$\nabla \cdot \frac{\partial \vec{J}}{\partial t} = -\frac{\partial^2 \rho}{\partial t^2} = \epsilon_0 \nabla^2 \vec{\phi}, \quad (9)$$

whence

$$\left(\frac{\partial \vec{J}}{\partial t} \right)_T = \frac{\partial \vec{J}}{\partial t} - \epsilon_0 \nabla \vec{\phi}. \quad (10)$$

Boundary conditions on the second time derivative of ϕ must be specified. This proves difficult for an arbitrary configuration. This scheme can have problems converging if there are large variations in $\omega_p^2(x)$ caused by large density gradients.

As suggested by Boyd and Hewett⁴, an alternative formulation to equation 8 solves the equation

$$\nabla^2 \vec{\xi} = \mu_0 \frac{\partial \vec{J}}{\partial t}, \quad (11)$$

with

$$\vec{\xi} = \vec{E}_T - \nabla \chi.$$

Replacement of \vec{E}_T by $\vec{\xi} + \nabla \chi$ in equation 7 gives

$$\left[\nabla^2 - \frac{\omega_p^2(x)}{c^2} \right] \vec{\xi} = \frac{\omega_p^2}{c^2} \nabla \chi + \mu_0 \vec{S}, \quad (12)$$

with

$$\nabla^2 \chi = -\nabla \cdot \vec{\xi}.$$

The transverse projection is performed on the quantity $\vec{\xi}$ to obtain \vec{E}_T in this scheme. An elliptic equation is solved for χ to There exists a great deal of freedom in specifying the boundary conditions for χ . Boundary conditions on $\vec{\xi}$ are determined by the boundary conditions on \vec{E}_T and on the first and second derivatives of χ normal to the boundary. A disadvantage is that the boundary conditions on $\vec{\xi}$ are changed with each iteration.

III. Tests

The magnetoinductive code that has been developed is benchmarked in a series of tests described in this section. The first such test which directly compares the two schemes is presented first. An initially quasineutral plasma with an equal number of protons and electrons is placed in a box. The box is positioned in an azimuthally symmetric cylindrical geometry. The walls of the box are assumed to be conducting and are set to zero potential. Particles within the box elastically rebound off the walls. There are not any external sources of energy so there should not be any energy flow in or out of box. The plasma is initialized in an equilibrium configuration where the plasma density is uniform and the electron and ion temperatures are equal and constant. For the test presented here the plasma is placed in the center half of the box with vacuum in the remainder as approximately shown in Fig. 1. The inner box radius is 2.5 cm and the outer radius is 5.0 cm. The box is 10.0 cm long in the z-direction. The grid is 20 cells by 20 cells. The plasma is assigned a temperature of 1 keV and the plasma density is $1.0 \times 10^{12} \text{ cm}^{-3}$. The time step is 4.0×10^{-12} seconds.

The results from Nielson and Lewis scheme are physically reasonable. The simulation is followed forward in time for 2.0 ns. Electrons expand faster into the vacuum region because their thermal velocities are larger. Local charge imbalances are created with a negative charge density occurring in what was originally the vacuum and a positive charge density occurring in the main body of the plasma. The contours of the electrostatic potential in Fig. 2 highlight this behavior. The maximum of the electric potential is in the same range as the plasma temperature. It is unlikely that potentials much larger than the temperature would become established since the plasma is initialized in a thermal equilibrium. Towards the beginning as electrons stream out of the plasma, a current towards both walls of constant z builds up. This creates a buildup of magnetic flux. Later in time, electrons that hit the wall are reflected reversing their direction of motion. As these electrons come counterstreaming back, the net current starts decreasing and the magnetic flux decreases. This decrease in the magnetic flux is seen in the plot E_{Tz} in Fig. 2. Considering the coarseness of the grid, it is seen in Fig. 3 that energy is quite well conserved increasing by only 0.7% over the length of the run. In runs where the plasma completely filled the computational volume and the other parameters remained constant, energy is conserved to 0.2%.

In contrast the formulation of Boyd and Hewett was unstable quickly and stopped after a few tens of time steps. The results in Fig's. 4 and 5 show informations after 10 time steps or .04 ns. In Fig. 4, the plots of the electrostatic potential have the wrong sign in the vacuum and plasma regions. The maximum value of 30 kilovolts is much larger than what is expected. Similarly the maximum value of the transverse electric field is much larger. As can be seen from Fig. 5 the conservation of energy is badly degraded in this example after the simulation has progressed forwards only 10 time steps. This scheme is clearly unacceptable for this particular problem. It should be mentioned that this is probably the worst type of problem for this scheme. Its worst failing is that the boundary conditions for the auxiliary function χ are changed with each iteration of the solution. In this case the fields have random character that are determined by the motion of the particles. The fluctuations leave \vec{E}_T having a spiky and random character that can change considerably from time step to time step. The iterative procedure has a great deal of difficulty in converging the boundary conditions in those circumstances. This technique is probably suitable in a situation where external conditions primarily determine

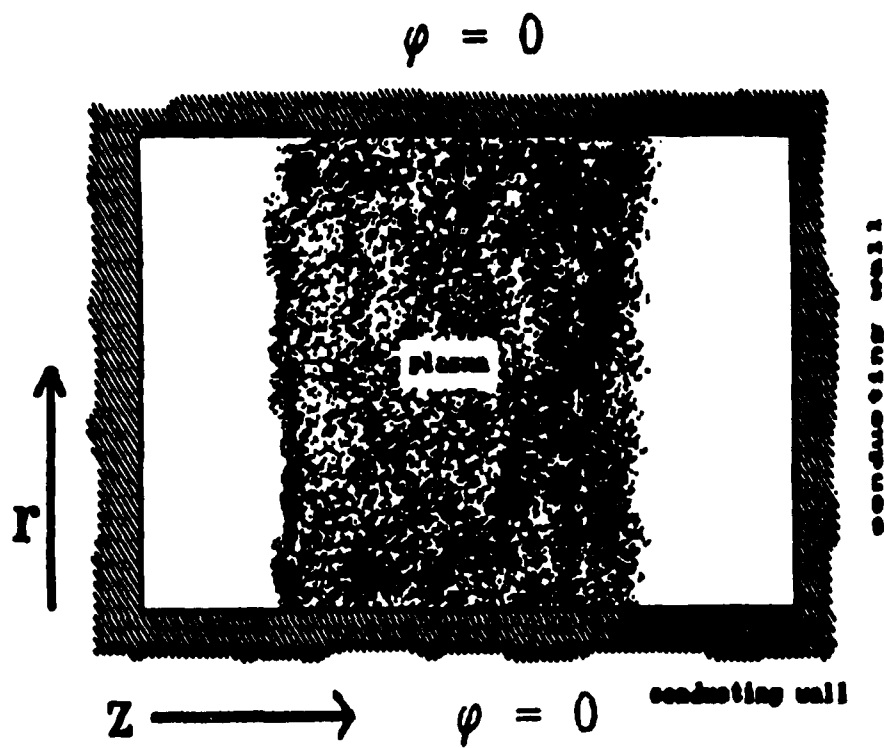


Figure 1. Plasma initially occupies half of a metallic box set to zero potential in an axisymmetric cylindrical geometry.

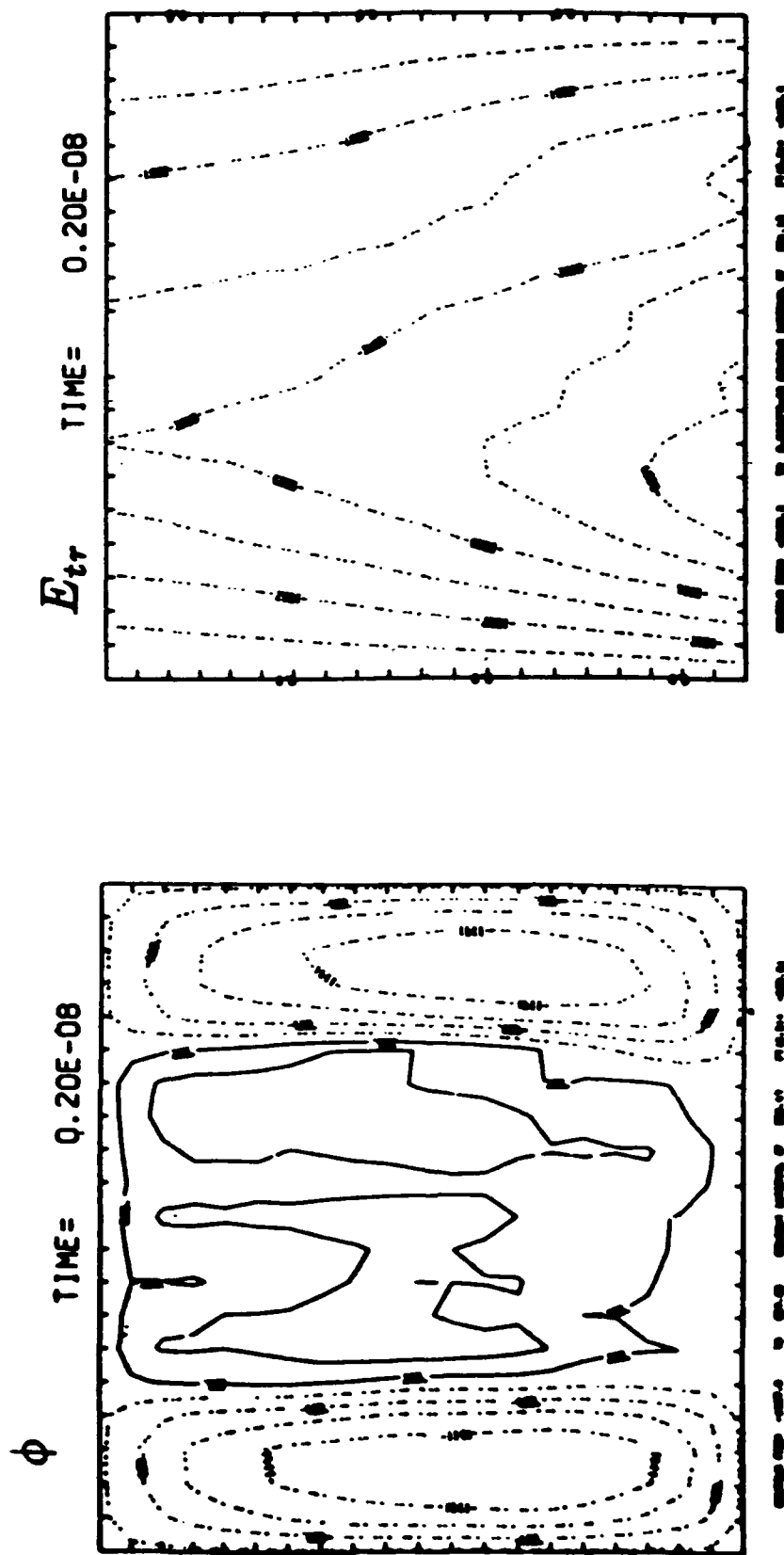


Figure 2. Contours of the electrostatic potential and transverse electric field at 2 ns for the Nielson and Lewis scheme for the configuration shown in Fig. 1. Maximum values are $|\phi|_{max} = 1.5$ kV and $|E_T|_{max} = 7$ kV/M.

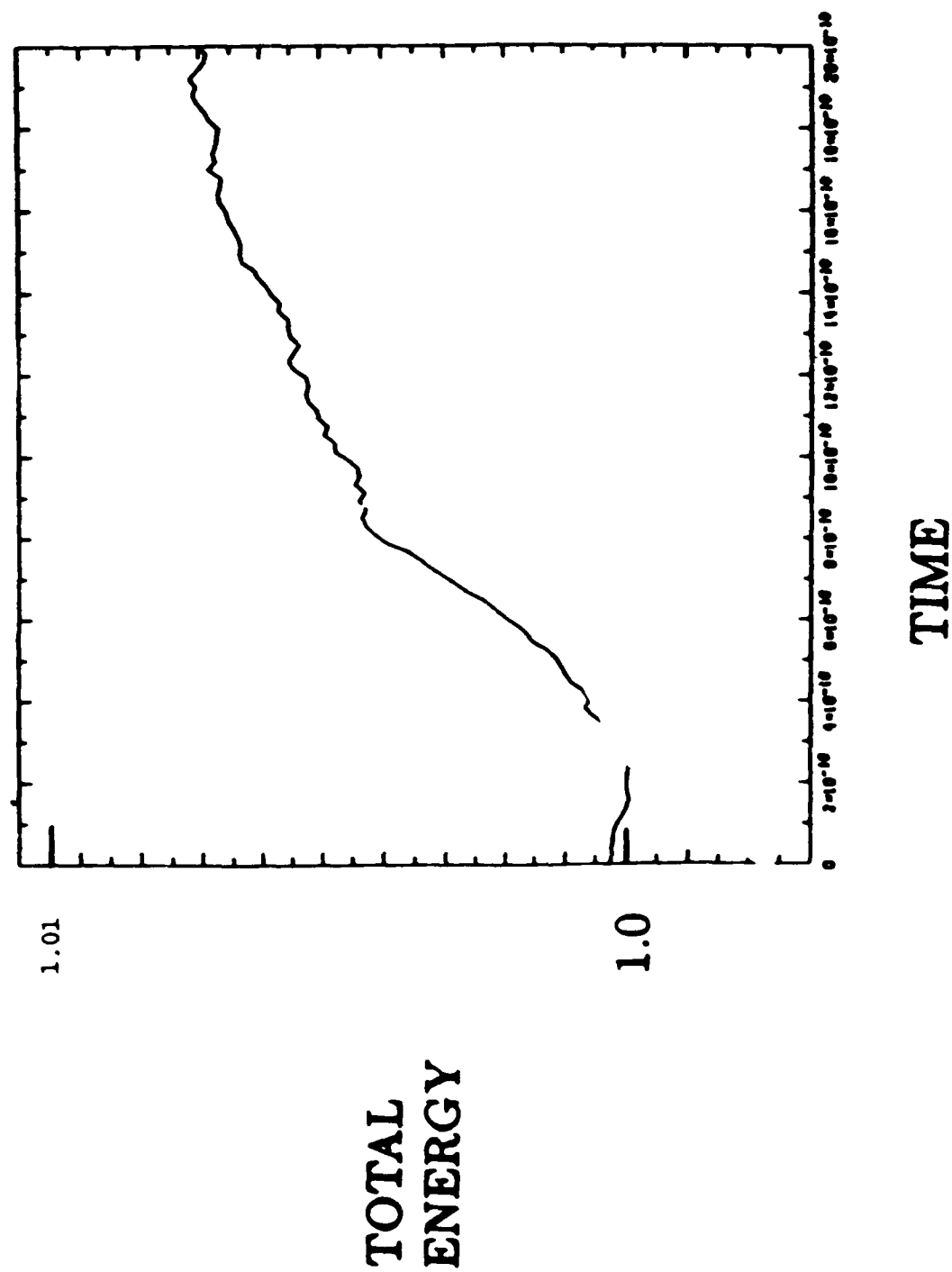


Figure 3 Energy conservation for the Nielson and Lewis scheme for the configuration shown in Fig 1 after evolving for 2 ns. Maximum change is 0.7%.

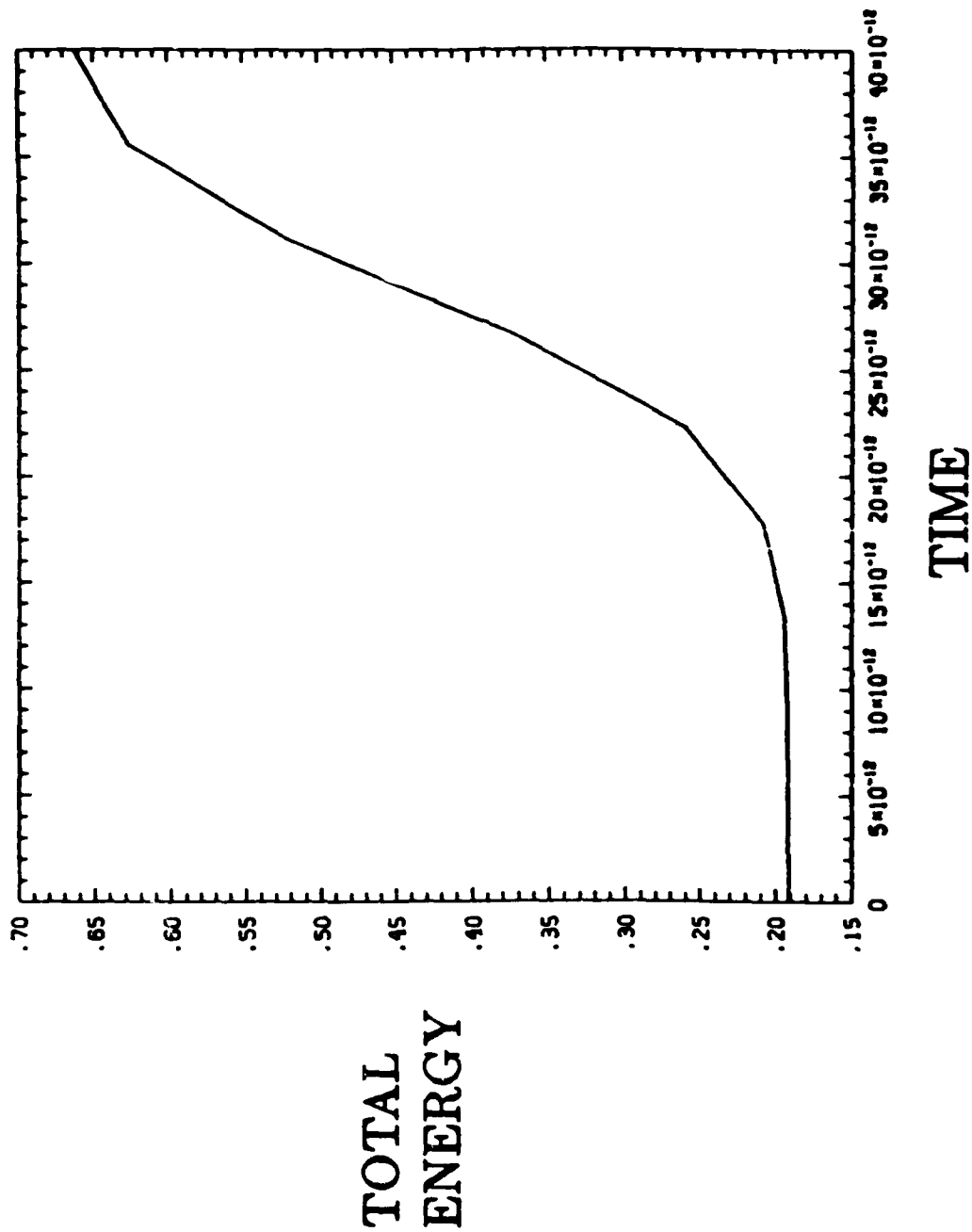


Figure 5. Energy conservation for the Boyd and Hewett scheme for the configuration shown in Fig 1 after evolving for .04 ns. Maximum change is 260%

the boundary conditions on E_z and that these fields are smooth at the boundaries. For many of the applications such as modeling a PEOS, the particles exert a great deal of influence on the structure of the transverse electric field. For this reason, it is expected that this formulation may have too much difficulty converging and most of the effort has been concentrated on the Nielson and Lewis formulation.

Further testing has been performed using the Nielson and Lewis formulation in conditions more likely to be encountered in pulsed power applications. The first tests examined the accuracy of the electric and magnetic field solutions for the magnetoinductive model when the interior of the simulation is a vacuum. Analytic solutions for a cylindrically symmetric transmission line are derived here and compared with the results of the simulation code. The simulation geometry and circuit model are shown in Fig. 6. The solutions given by the magnetoinductive model should correspond to TEM-like modes with infinite wavelengths. The TEM mode has only B_z and E_r components thus we expect only these components for the present case. A resistor is connected at the load $z = z_1$ side of the simulation. The boundary conditions on ϕ , ϕ_r , and ϕ_z are specified as functions of time on the upper and lower surfaces. This is equivalent to specifying the current that flows through the resistor as a function of time. For this case the interior values of the sources ρ and J are zero. Using equation 2 the electrostatic potential satisfies the equation

$$\nabla^2 \phi = 0$$

where the boundary conditions

$$\phi(a, z) = 0, \quad \phi(b, z) = \phi(t)$$

are imposed. The solution for the electrostatic potential is given by

$$\phi(r, z, t) = \frac{\phi(t) \ln(r/a)}{\ln(b/a)} \quad (13)$$

The longitudinal projection of the electric field is found from taking the gradient of ϕ to yield

$$E_{Lr} = \frac{\partial \phi}{\partial r} = \frac{\phi(t)}{r \ln(b/a)} \quad (14)$$

Since the simulation is assumed azimuthally symmetric, the magnetic field has only a nonzero θ -component. From equation 3, Ampere's law by components in cylindrical coordinates is

$$\frac{\partial B_z}{\partial r} = \frac{1}{c} \frac{\partial E_r}{\partial t} \quad (15a)$$

$$\frac{1}{r} \frac{\partial(r B_\theta)}{\partial r} = \mu_0 J_z = I_0 \quad (15b)$$

The integral form of Ampere's law specifies the magnetic field in the vacuum as a function of the current in the lower surface

$$B_\theta(r, z, t) = \frac{\mu_0 I_0}{2\pi} \frac{1}{r} \quad (16)$$

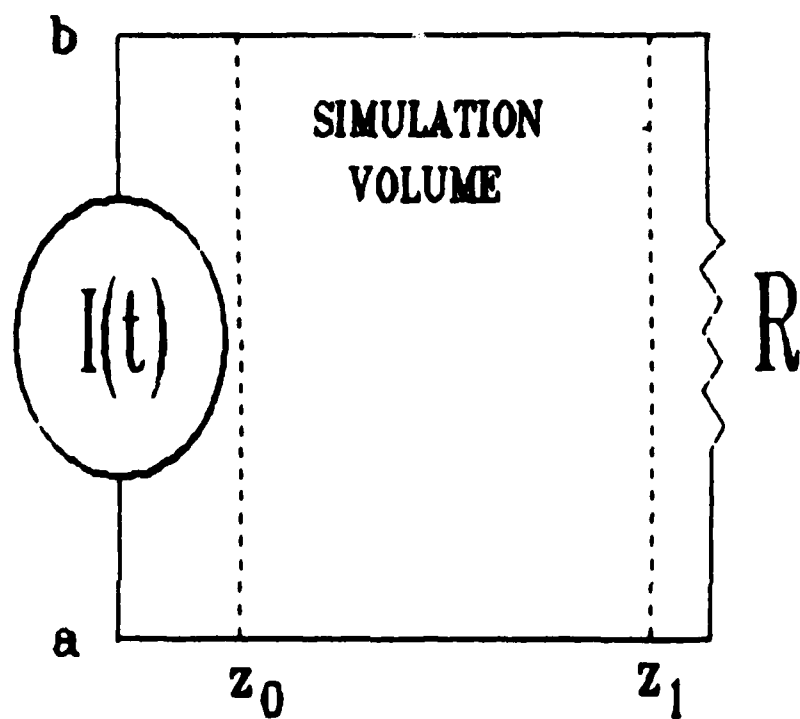


Figure 6. Circuit model for vacuum tests.

The current can be determined by eliminating the magnetic field from Eq's 15a and 16 to get,

$$\frac{\partial I_a(z, t)}{\partial z} = \frac{2 \pi \epsilon_0}{\ln(\frac{b}{a})} \frac{\partial \phi}{\partial t},$$

which has the solution

$$I_a(a, z, t) = -\frac{2 \pi \epsilon_0 (z_1 - z)}{\ln(\frac{b}{a})} \frac{\partial \phi}{\partial t} - I_L, \quad (17)$$

where I_L is the current flowing through the resistor. Thereby B_θ is given by

$$B_\theta = -\frac{\mu_0 I_L}{2 \pi r} - \frac{(z_1 - z)}{r c^2 \ln(\frac{b}{a})} \frac{\partial \phi}{\partial t}. \quad (18)$$

Lastly the solution for the transverse part of the electric field is given by the z-component of Faraday's Law with equation 18:

$$\frac{\partial E_{Tr}}{\partial z} = \frac{\mu_0}{2 \pi r} \frac{\partial I_L}{\partial t} + \frac{(z_1 - z)}{r c^2 \ln(\frac{b}{a})} \frac{\partial^2 \phi}{\partial t^2}.$$

Since the load is assumed to be purely resistive, we have as a boundary condition at the load side

$$E_{Tr}(r, z_1, t) = 0.$$

Integrate once with respect to z with the above boundary condition to get

$$E_{Tr}(r, z, t) = -\frac{\mu_0 (z_1 - z)}{2 \pi r} \frac{\partial I_L}{\partial t} - \frac{(z_1 - z)^2}{2 r c^2 \ln(\frac{b}{a})} \frac{\partial^2 \phi}{\partial t^2}. \quad (19)$$

The agreement between the analytic solutions given by Eq's 18 and 19 and the code results is excellent as can be seen in Fig. 7. The results in Fig. 7 were obtained with a 20×20 grid. This test demonstrates that the routines that solve for the electric and magnetic fields are working quite well.

The next test concentrates on the particle motion and emission. The results from the simulation are compared with the one-dimensional Child-Langmuir diode in an electrostatic, nonrelativistic limit. The geometry for this test is shown in Fig. 8. The magnetic field and the inductive electric field are removed from the simulation. The only field that effects particle motion is the electrostatic electric field. A positive potential is placed on the top plate with respect to the bottom plate. Electrons are emitted from the bottom plate and travel to the top plate where they are absorbed. It should be mentioned that for this test electron emission is radial and the equations presented here for the Child-Langmuir diode in a Cartesian geometry. However if the change in radius from the bottom to the top is small compared to the average radius, the emission should be approximately Cartesian. Electron flow from the bottom plate is presumed to be space-charge limited.

The Child-Langmuir diode finds the stationary solutions when electrons are assumed to be cold, i.e. finite temperature effects are ignored. The voltage $V(t)$ of the top plate with

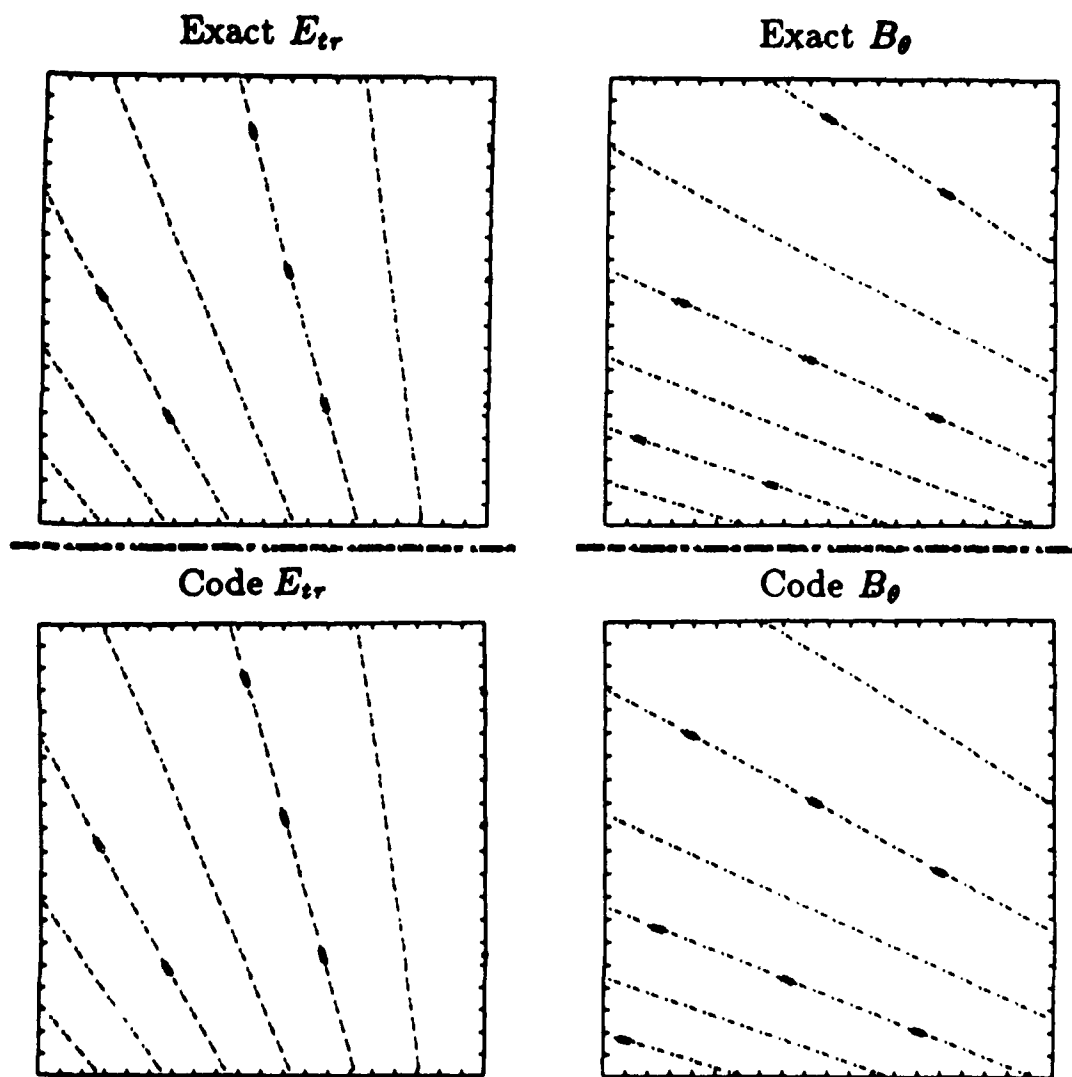


Figure 7. Compares the analytic solutions with the code solutions in a vacuum. Agreement is very good.

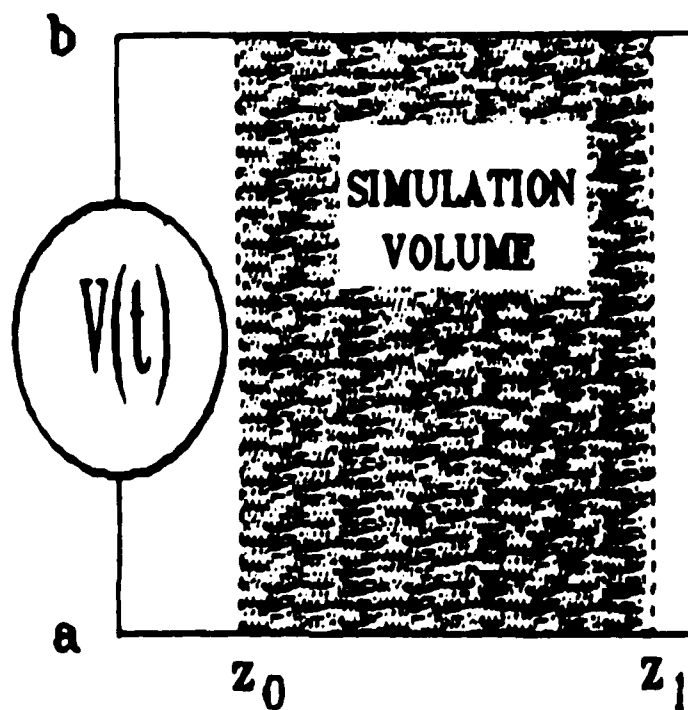


Figure 8. Configuration for testing Child-Langmuir emission.

respect to the bottom plate is increased adiabatically as a function of time allowing the system to become gently adjusted to its final state rather than not adjusting its maximum value. The applied voltage is described by the relation

$$V(t) = V_0(1 + t/\tau)^{1/2}$$

where τ is the risetime. The potential is expected to obey the relationship

$$\phi(r) = V_0 \left(1 - \frac{r^2}{a^2} \right)^{1/2} \quad (20)$$

Various simulation parameters for this run are: $\tau = 2.0 \times 10^{-10}$ sec, $a = 4$ cm, $b = 5$ cm, $V_0 = 100$ kV, time step $\Delta t = 2.0 \times 10^{-12}$ sec, and the simulation evolved forwards in time to 2.4 ns. The simulation results compare reasonably well with the expectations from 1-D Child Langmuir flow as is seen from Fig. 9.

This configuration also exhibited oscillations whose period is correlated with the electron transit time across the diode. These oscillations are seen in the plots of the anode and cathode current in Fig. 10. Child Langmuir theory predicts the current density to be

$$J = 2.34 \times 10^{-5} V^{3/2} d^{-2} \quad \text{Amps/cm}^2$$

where V is the diode voltage in megavolts and d is the gap spacing in centimeters. The total current can be obtained by integrating the surface area. The mean value of the cathode current agrees to about 5% with the stationary current predicted by Child Langmuir flow. Oscillations of this nature are common in diode configurations⁵. The exact mechanism driving the oscillations is not known and is a topic for further investigations. The equations describing these flows are nonlinear and may have different solutions depending on the initial conditions. Thus it is possible that the Child Langmuir flow in radial geometry exhibits these oscillations. Another possibility is that temporal and spatial discretization utilized in the code may be the mechanism behind the oscillations. For example grid instabilities will raise the electron temperature such that thermal effects from the finite temperature of the particles might be important.

The final tests reported here included the magnetic field and the inductive electric field in the same configurations described above. If the current is sufficiently strong, it should be possible for the magnetic field to prevent electrons from crossing the gap and to achieve a magnetically insulated flow. It was discovered however that specifying just the electrostatic voltage instead of the total voltage creates an emission instability. The mechanism proceeds as follows. The applied voltage draws current from the bottom plate. This current increases as the applied voltage increases. This increasing current drives a time changing magnetic flux which in turn drives an induced electric field. The induced electric field serves to enhance the current rather than decrease it. Thus a feedback loop is formed where an increasing current drives an induced electric field which serves to further increase the current. The obvious remedy to this problem is to specify the total voltage rather than just the electrostatic portion. However the boundary conditions require the specification of not only the electrostatic voltage but also its first and second order time derivatives. It is difficult to split the contributions to the total voltage from E_L and E_T . Such a splitting depends on the external circuits that the simulation is connected to. This area is under investigation at this time. Another possibility is to artificially limit in a way

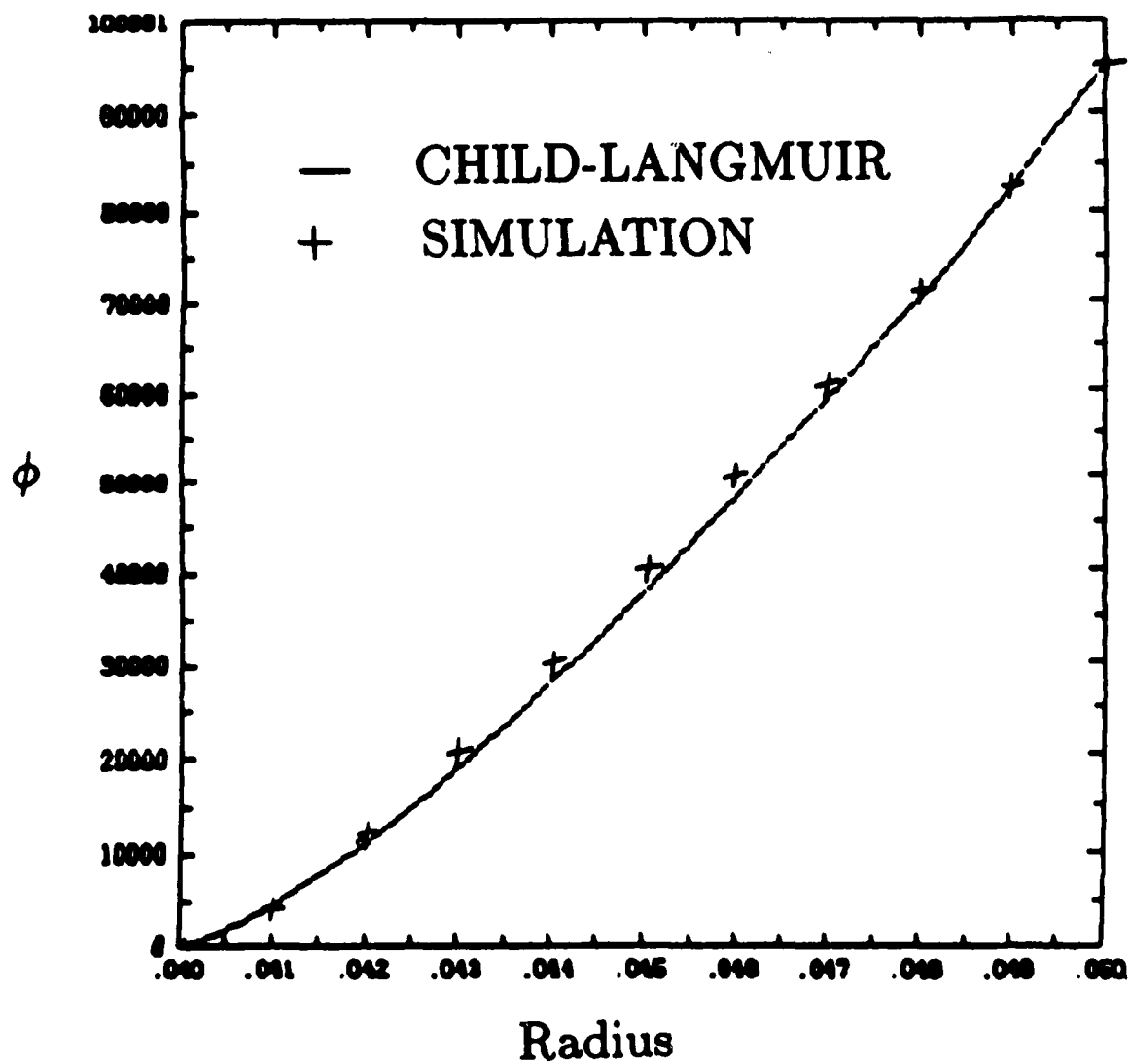


Figure 9. Simulation results favorably reproduces potential expected for Child-Langmuir diode.

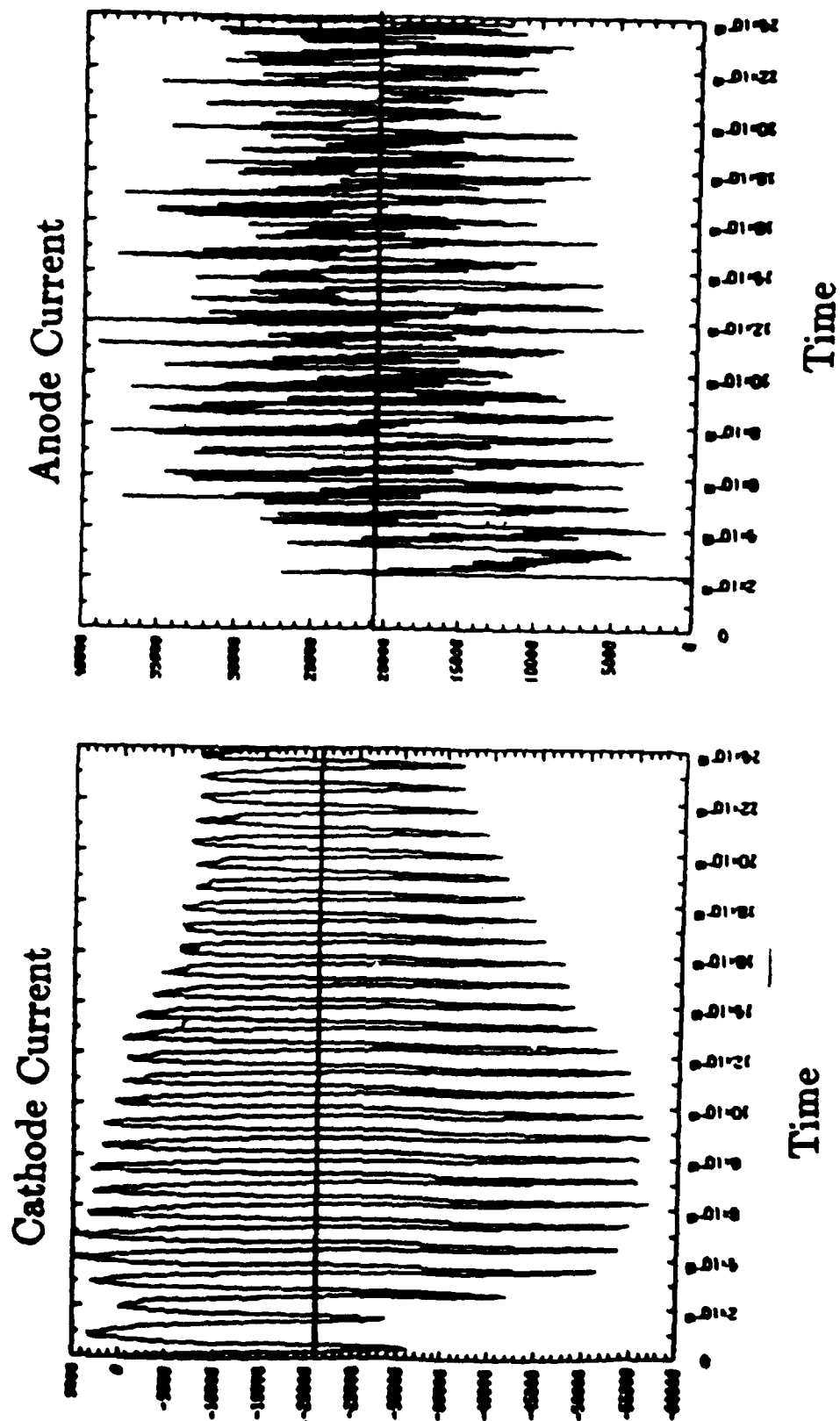


Figure 10. The current from the simulation oscillates but the mean value of the cathode current agrees to around 5% with the analytic model.

that dampens the instability. This approach may be useful in achieving a time stationary solution but would not be realistic enough to follow the time evolution of a problem. The magnetostatic code ELECTRA is probably more suitable for these applications. The next steps are to include more realistic circuit models. These would be added first to an electrostatic code and subsequently implemented in magnetostatic and magnetoinductive codes.

IV. Summary and Expected Applications

The magnetoinductive formulation is promising in the amount of physics that is included while not being restricted to resolving propagation of light waves. Practical implementation has proved to be difficult. All of the various pieces of the code have passed benchmark tests. The primary difficulty lies in trying to specify the boundary conditions. Two different schemes have been examined for performing the iterative solution on the transverse electric field. The Nielson and Lewis scheme is preferred but requires specification of the potential associated with the longitudinal electric field and its first- and second-order time derivatives. This is not an easy task in an arbitrary configuration. The Boyd and Hewett scheme requires less information on the boundaries but has more problems converging when the transverse electric field is not sufficiently smooth at the boundaries. The utility of the magnetoinductive formulation depends on the particular application.

The initial applications of the magnetoinductive codes are aimed towards the fast opening switches crucial to inductive energy storage schemes. These will emphasize looking at important pieces of the problem in a simpler configuration. One such application is to examine the role microinstabilities play in the current conduction phase of PEOS. Another is to implement different models of particle emission and investigate how these different models effect current conduction through the sheath. It may also be used to examine the reflex switch.

References

1. C. G. Darwin, *Phil. Mag.* **39**, 537 (1920)
2. J. D. Jackson, *Classical Electrodynamics*, Wiley, New York, 2nd. ed., (1975).
3. C. W. Nielson and H. R. Lewis in *Methods in Computational Physics*, Vol. 16, (J. Killeen, Ed., Academic Press, New York, 1976)
4. J.K. Boyd and D. W. Hewett, Lawrence Livermore National Laboratory, Report No. UCRL-94349 (1986).
5. C. L. Birdsall and Bridges, *Electron Dynamics of Diode Regions*, New York (1966).

Numerical Models of Bremsstrahlung Diodes

Much effort in collaboration with Berkeley Research Associates during the past year has been aimed at improvements in modeling Bremsstrahlung diodes. Bremsstrahlung diodes are the most common x-ray source in use today. Although their spectrum is somewhat harder than that desired by many users, their simplicity and reliability as a radiation source has made them popular. The trend has been for x-ray source users to demand longer pulses and higher overall dose over a broader area while maintaining acceptable uniformity. This trend has pushed present diode designs to their limits leaving their performance in this regime somewhat uncertain.

The technical issues that arise in this new diode performance regime are similar to those that have arisen in the past. In particular, diode design requires a detailed picture of electron flow from the cathode to the converter as well as global electrical characteristics such as impedance. In addition to these issues, the longer pulse times bring other effects into consideration such as gap closure from plasma formation at the cathode and anode walls.

In cases where theoretical support of diode design has been helpful, the results have come mainly from electromagnetic particle-in-cell (PIC) simulations. Such simulations follow the trajectories of representative electrons while advancing the electromagnetic field equations on a grid of cells in a way that is consistent with the currents created by the electrons themselves. Unfortunately, such techniques have also encountered limitations as pulse times have become longer. Technically to advance the electromagnetic field stably, the timestep must be substantially smaller than the time it takes for a light wave to cross a cell in the calculation. In low-impedance diodes where the gap spacing is a centimeter or less and at least ten or twenty cells are needed to span the gap this would require sub-picosecond timesteps. With pulse times of hundreds of nanoseconds, the number of timesteps for a complete simulation could run into the millions. This kind of numerical difficulty in which timescales that must be resolved are very far apart is known as "stiffness".

Among the aims of our current research is to find useful numerical techniques for diode modeling that will work for these longer pulse-lengths. In similar circumstances where very fast timescales interfere with the slower timescales of interest, two general strategies are used. The first is to try a reduced physical description, viz. a simpler form of the governing equations in which the fast timescale is absent. The magnetoinductive model and the steady state model, Electra, are examples of this approach. The second strategy is to find other numerical formulations of the complete equations in which fast oscillations are stably damped away when the timesteps are too large to resolve them. This approach is being investigated as well.

Steady state diode calculations and development of ELECTRA

The long pulse lengths of interest in many applications often mean that the power flow in the diode has reached a steady state. Even in circumstances where this is not precisely true, the steady state or equilibrium picture of the diode represents the main trend in its behavior and provides insight that can be exploited in future designs. The electromagnetic field equations appropriate to stationary charge distributions and currents are simply:

$$\nabla^2 \phi = -\frac{\rho}{\epsilon_0},$$

Poisson's Equation, and

$$\nabla \times \mathbf{B} = \mu_0 \mathbf{J},$$

Ampere's Law, with

$$\mathbf{E} = -\nabla\phi \text{ and } \nabla \cdot \mathbf{B} = 0.$$

Here \mathbf{E} is the electric field, and \mathbf{B} is the magnetic induction, ϕ is the static potential, \mathbf{J} is the current density and ρ is the charge density. These field equations can be used as the basis of a particle-in-cell simulation in which the particles are moved a timestep and then the charge and current distributions are formed from them and taken as static for the purpose of calculating the fields. Assuming a sufficient number of timesteps and the existence of a steady state, the currents and charge distributions indeed become steady enough for the static field assumption to be valid.

The static field assumption offers two advantages in the present application. Since electromagnetic waves do not exist in the static limit, there is no timestep constraint arising from them. While accuracy demands that the particles themselves not move more than a cell per timestep, this is a milder limitation. Secondly, since the steady state solution is the aim of the calculation and because the specific intermediate states are not critical to the attainment of a solution, any expedient measure taken to speed convergence to equilibrium is allowed. In short, it should be possible to arrive at a steady state solution in far fewer timesteps using the static equations than by using the full set of Maxwell's equations.

Simulations based on static field equations have been used in the past at the Naval Research Laboratory, Sandia National Laboratory and elsewhere. They represent some of the earliest attempts at diode modeling; e.g. the DIODE2D code at NRL. They are not common today for two reasons: the high-impedance, short pulse diodes can be modeled with the more complete electromagnetic simulations; and there is no general purpose easily used static code available to the pulsed power community as is the case with the fully electromagnetic codes (e.g. MAGIC, MASK).

Berkeley Research Associates in collaboration with NRL has revived the equilibrium diode code for long pulse diode applications. ELECTRA is the name of the new code produced under this effort and test versions have been in application over the past six months. ELECTRA has features in common with the old DIODE2D code once used at NRL. It is a two-dimensional simulation in r and z allowing anode and cathode shapes to be represented as internal structures conformal to the grid.

Simple field emission algorithms are based on Gauss' Law. Both ELECTRA and DIODE2D have simple foil converter models for reflex diodes. ELECTRA, however, has many improvements over the older code.

ELECTRA is based on optimized finite difference field-solvers rather than Fourier transform methods. Particle motion is referred to a "grid-based" coordinate system rather than actual physical coordinates. This combination permits nonuniform gridding in either coordinate with arbitrary spacing.

The magnetic field calculation in ELECTRA can be based either on instantaneous or time-averaged current distributions which can speed convergence to steady state.

Improved particle movers are incorporated into ELECTRA. One option allows timesteps much larger than the cyclotron period ($\Omega\Delta t \gg 1$). The method uses a magnetic moment correction which is inoperative when $\Omega\Delta t \ll 1$, but produces the correct $\mathbf{E} \times \mathbf{B}$ drifts when $\Omega\Delta t \gg 1$. This improvement allows simulation of pinch-beam diodes without timestep limitations imposed by the gyrofrequency.

Inverse Reflex Diode application.

The first application of the prototype ELECTRA early this year was to the Inverse Reflex Diode¹. Figure 1 below illustrates a typical design with the electron flow channeled along the axis and then directed outward in radius. This is distinct from the pinch beam diodes in which the power density increases with decreasing radius. The inverse diodes have been suggested as a benign load for pulsed power experiments as well as an advanced converter design for broad area illumination. Simulations with ELECTRA confirmed the tendency of ion emission to complicate and sometimes spoil the diode's performance as was suspected after preliminary experiments. ELECTRA provided the asymptotic state of the diode giving insight into its dynamical behavior. Because of its flexibility over the older static codes, several designs could be simulated in a short time.

Blackjack ring diode simulations

The new demands of pulsed power include higher dose as well as better dose uniformity. One successful diode design in this regard has been the modular ring diodes on the Blackjack simulator at Maxwell Laboratories. A schematic representation of the diode as seen from the back is shown in figure 2. In this design the electric pulse from the generator follows the posts located around the ring through a hole in the anode to the azimuthally symmetric ring cathode. The cathode is notched as shown in cross section (figure 3) producing two electron beams. These beams impinge on the anode and the return paths divide according to the inductance of the transmission line producing current above and below the beams. The magnetic field pressure produced on the sides of the beams forces pinching toward the center of the anode.

The virtue of modular ring diodes lies in the ability to place rings concentrically within other rings to form arrays. Such an array offers higher dose than a single converter. Several technical issues remain before this design can be exploited to the fullest advantage, and simple questions arise for which simulations may give answers. For example, what are the differences between the electron flow in rings at small radii versus those at larger radii? Or put another way, how critical is the ring geometry as a function of radius? For large arrays to work well each ring must perform properly. The basic electrical properties of the rings (e.g. impedance) must also be well understood so that circuit models for the large diode arrays will be accurate. At present the closest packing of ring diodes in radius Δr is about 10 cm. Designers would like to pack diodes closer to provide better uniformity. One needs to know how close the anode can come to the cathode shank before magnetic insulation breaks down. Another question: how thin can the cathode be made (how close can the beams be brought together) without affecting performance?

We have begun to use ELECTRA to answer some of these questions. A preliminary run is shown below in figure 4. Here we see electrons emitted from the ring cathode and pinching at the anode. Such plausible results are encouraging. Encouraging is the small amount of computer time (less than 1 hour on a CDC 785 at NRL) needed to obtain the solution. Berkeley Research Associates is conducting this study in collaboration with Branch 4720 of NRL and Maxwell Laboratories. We hope to be able to piece together both experimental and simulation results to help improve this converter concept.

Reference

1. DNA Pulse Power Review, S100-100, 1977, by R.J. Commisso, and J.M. Nease, Fort Belvoir, N.M.

AD-A184 986

ADVANCED CONCEPTS THEORY ANNUAL REPORT 1986(U) NAVAL
RESEARCH LAB WASHINGTON DC 12 AUG 87 NRL-MR-6051
NIPR-86-570

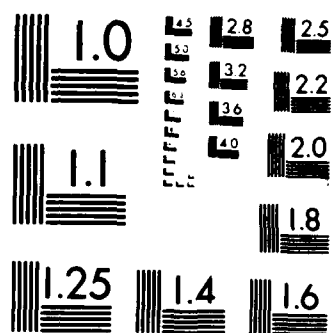
2/2

UNCLASSIFIED

F/G 20/9

NL





MICROCOPY RESOLUTION TEST CHART
NATIONAL BUREAU OF STANDARDS 1963 A

"Generic" BIRD Design

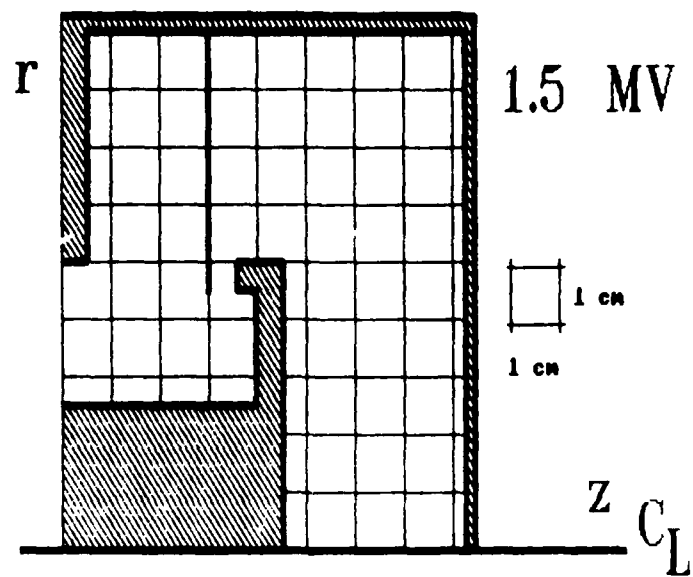


Figure 1

Ring diode with post hole convolutes

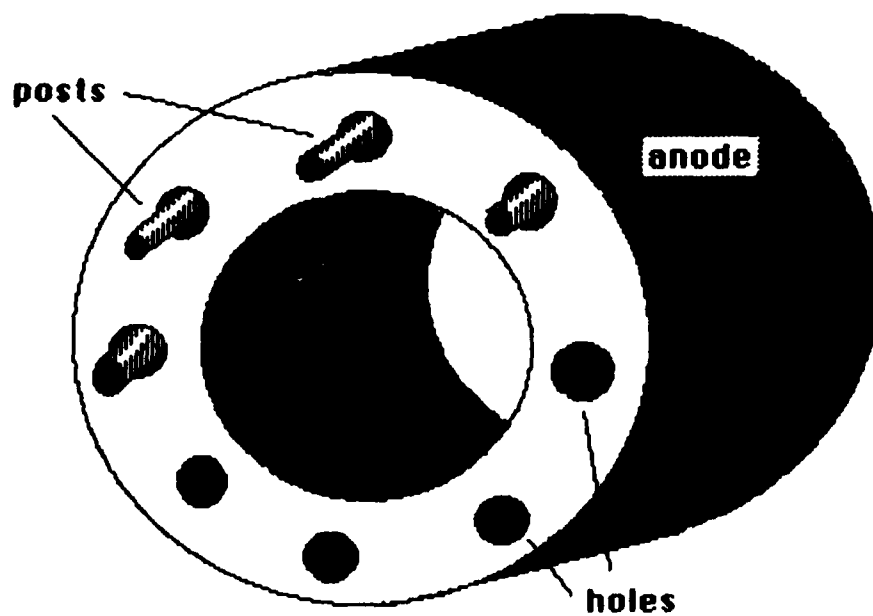


Figure 2

cross section of ring diode

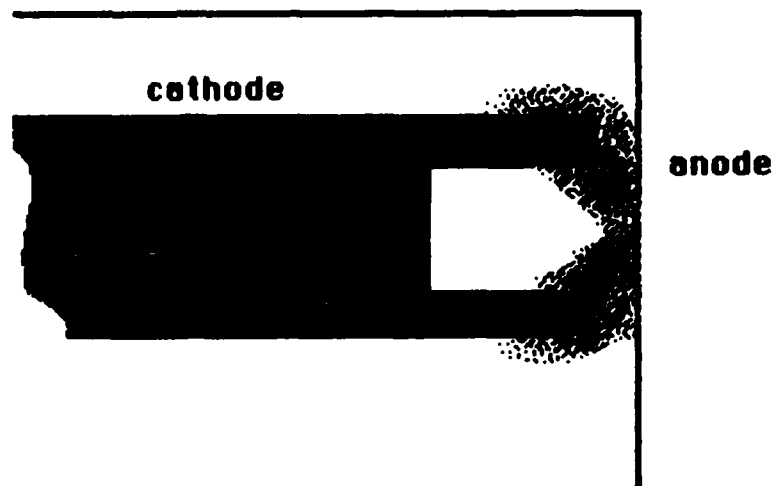
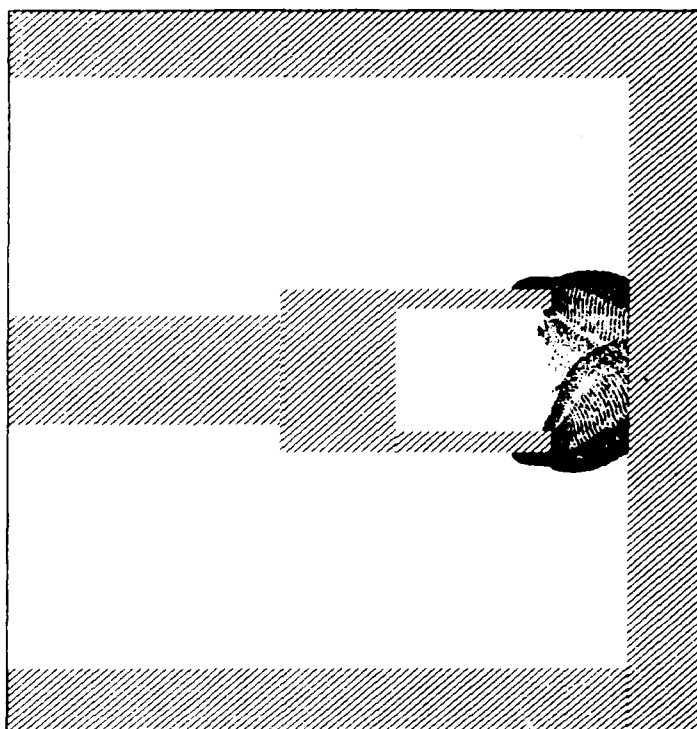


Figure 3

$T=0.12E-08$
PARTICLES



ELECTRA VERSION 2.3

Figure 4

Effect of pulse sharpening on imploding neon Z-pinch plasmas

S. J. Stephanakis, J. P. Apruzese, P. G. Burkhalter, J. Davis, R. A. Meger, S. W. McDonald,^{a)} G. Mehlman,^{b)} P. F. Ottinger, and F. C. Young
Naval Research Laboratory, Washington, DC 20375

(Received 24 October 1985; accepted for publication 4 February 1986)

The radial implosion of hollow, cylindrical neon gas columns, driven by currents of up to 1.45 MA, produces a linear Z pinch with over 70% of the radiation in neon *K* lines. A plasma erosion opening switch (PEOS) is used to eliminate prepulse and to reduce the current rise time from ~60 to ~20 ns. Incorporation of the PEOS improves the uniformity of the Z pinch and increases the radiation yield.

Pulsed power generators have been used since the early 1970's to implode cylindrical plasma columns for the production of hot, dense Z pinches. This research has evolved from the explosion/implosion of a single wire,¹ to the implosion of cylindrical arrays of wires² and annular gas jets.³ In this letter, we present the first published experimental results on the implosion of annular neon gas jets, both with and without the incorporation of a plasma erosion opening switch (PEOS)⁴ to modify the driving current shape.

The Naval Research Laboratory's Gamble II generator can deliver up to 2 TW of electrical power to a 2- Ω load in 60 ns. In the experiments described here, up to 1.45 MA was delivered to a ~50 nH gas-puff load prior to implosion with no PEOS [Fig. 1(a)]. Slightly over 1 MA was delivered to 85-nH load when the PEOS was used [Fig. 1(b)]. An annular gas puff, 2.5 cm in mean diameter, was formed with a gas injection system and supersonic nozzle provided by Physics International Company.⁵ The neon gas was preionized with a UV flashboard source a few μ s before the current pulse. A thin wire mesh anode, 4 cm from the nozzle, allowed the gas to flow into a dump tube. The current returned via metallic posts at a diameter of 7 cm allowing 90° diagnostic viewing. Figure 1(a) shows the current with no PEOS and the resulting neon *K*-shell radiation pulse obtained with a filtered x-ray diode. The delay of the x rays relative to the current onset is 110 ns. The equivalent current and x-ray traces with a PEOS are shown in Fig. 1(b). The rise time of this current is only 20 ns. The delay of the x rays relative to the current is the same as in Fig. 1(a). Thus, the time required to implode the plasma is approximately the same with and without the PEOS.

The PEOS technology utilized is a recent development and is the subject of ongoing research.⁴ Suffice to say that the PEOS initially serves as a short circuit to the generator pulse. When the switch current reaches a predetermined value, it rapidly opens diverting the current to the load.

Absolute x-ray yields were measured with filtered x-ray diodes, tantalum-foil calorimeters, bolometers,⁶ and curved crystal spectrographs. Total yields of neon *K*-shell radiation (near 1 keV) measured with these diagnostics were consistent among themselves to within $\pm 15\%$. These yields were

measured as a function of plenum pressure for five driving current levels with no PEOS [Fig. 2(a)]. The curves are upper bounds of the data scatter for each current indicated. Typically a +0%, -20% uncertainty applies to each curve due to shot-to-shot variations in the peak current and for gas-puff variations due to nozzle degradation in repeated shots. For each driving current, the yield peaked at a mass per unit length (m) estimated by thin shell calculations⁷ to vary between ~15 and 45 μ g/cm at the lowest and highest currents, respectively. On some shots, an unfiltered bolometer⁶ was employed simultaneously with the filtered diagnostics. These measurements indicate a production efficiency of *K*-shell radiation which exceeds 70% of the total radiated energy. Figure 2(b) shows a plot of the five peak yields from Fig. 2(a) as a function of mass and peak current (I). The strong scaling ($Y \propto I^4 \propto m^2$) indicated, is consistent with 1-D slug model calculations⁷ and results from other laboratories.⁸

X-ray yield measurements versus pressure are more difficult with the PEOS since both the shape and magnitude of the current depend critically on the injected PEOS plasma flux and on the timing of plasma injection relative to current arrival. Shot-to-shot variations in these quantities lead to load currents of different shapes and amplitudes, thus inhibiting the systematic variation of gas-puff pressure at a nearly constant load current. This problem is particularly acute due to the strong dependence of *K*-shell radiation on current and mass. Nevertheless, *K*-shell yields have been measured with the PEOS for a range of current values and the results are shown in Fig. 3. Each solid dot represents a shot with the PEOS ignoring the mass or the exact shape of the current. For all these shots, the current rose in 10–30 ns, significantly less than the 60-ns rise time without the PEOS. These data are compared to the optimum results without the PEOS, represented by the solid curve. In general, yields with the PEOS are higher than the optimum yields without the PEOS at a given current. Some shots show an increase in yield of as much as a factor of 2.5 (dashed line).

Images of total *K*-shell emission, obtained with time-integrated pinhole photography and with spatially resolved x-ray spectroscopy,⁹ show qualitative differences with versus without the PEOS (Fig. 4). They show the Z pinch to be more uniform axially and tighter radially when the PEOS is used. For example, the image is partially obscured by one of

^{a)} Permanent address: University of Maryland, College Park, MD 20742

^{b)} Permanent address: Sachs/Freeman Associates, Inc., Landover, MD 20785

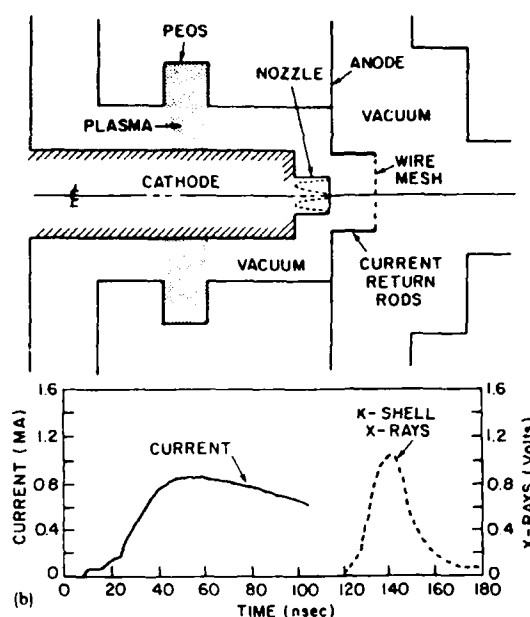
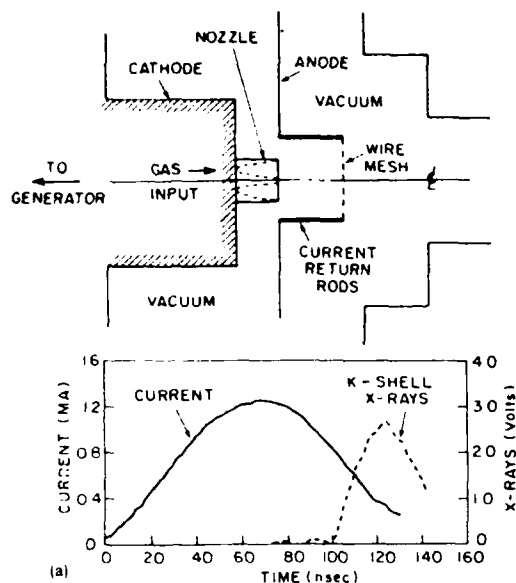


FIG. 1 Arrangement of the gas puff on Gamble II (a) without the PEOS and (b) with the PEOS. Load current and *K* shell x-ray traces are shown for each case.

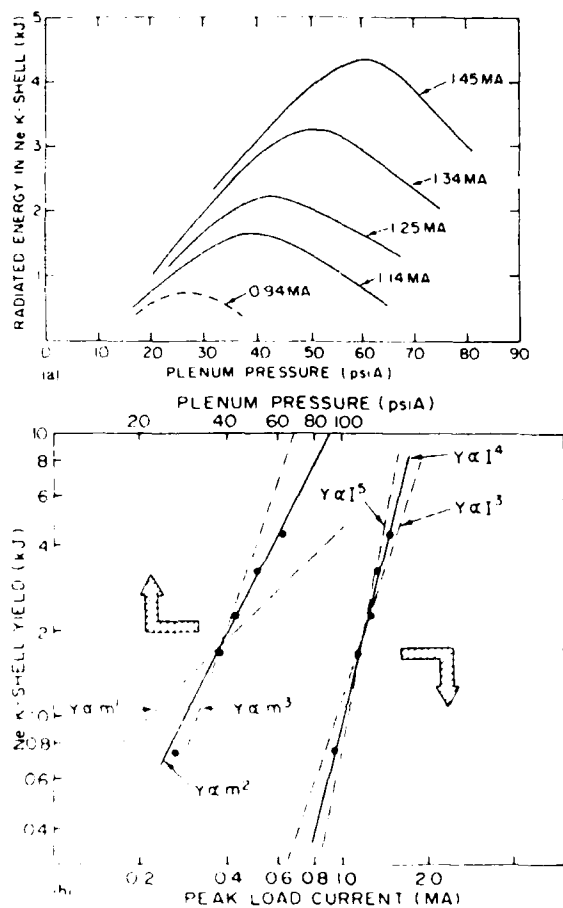


FIG. 2 Neon *K*-shell yields measured without the PEOS. (a) Yield vs gas-puff plenum pressure for different peak load currents and (b) peak yield scaling with peak load current and plenum pressure

the return-current rods without the PEOS, while it is fully visible with the PEOS. Although the sausage-like character of the pinch is still evident in the latter, plasma flaring is less severe and is superimposed on an intense core < 4 mm in diameter which is reasonably constant along the *z* axis. The axial uniformity of the pinch cannot be easily judged in these photographs due to overexposure. However, spectral lines, spatially resolved along the pinch axis, clearly show a decrease in intensity from the cathode to the anode in the non-PEOS case. In addition, the line intensity ratio varies noticeably along the axis. The $\text{Ly-}\alpha/\text{He-}\alpha$ ratio decreases from ~ 0.9 at the cathode to ~ 0.2 , 2 cm from the cathode. In contrast, for the PEOS case, the line intensities are nearly constant along the pinch axis and the ratio, $\text{Ly-}\alpha/\text{He-}\alpha$, is ≈ 1.1 along the length of the pinch. A collisional radiative equilibrium (CRE) model¹⁰ was used to estimate the plasma parameters consistently with the experimental results. The model matched the average $\text{Ly-}\alpha/\text{He-}\alpha$ ratios, radiation times, and total yields observed experimentally but failed to

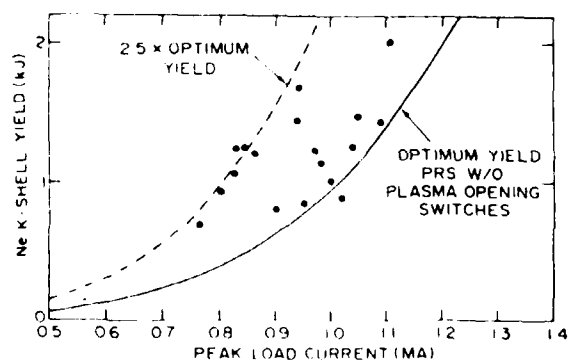


FIG. 3 Neon *K*-shell yields with the PEOS as a function of peak load current. The solid curve is the optimum yield without the PEOS scaled as I^4 . The dashed curve is 2.5 times the solid curve

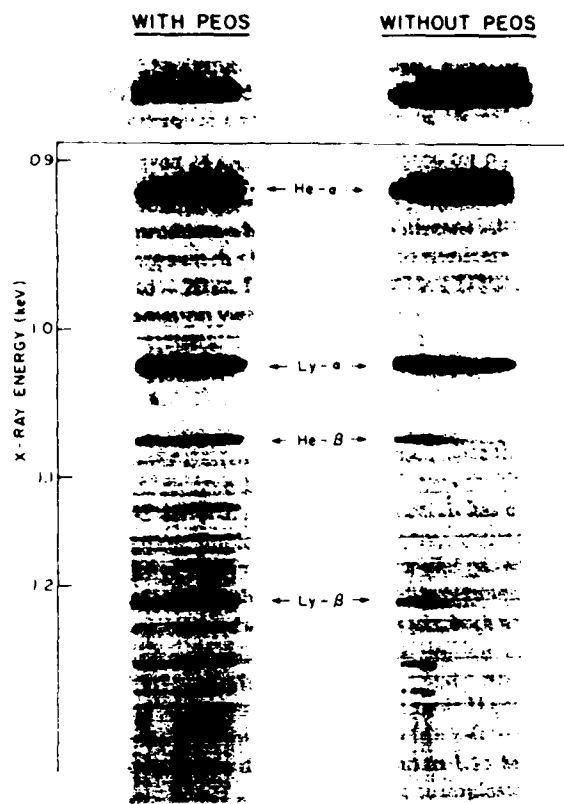


FIG. 4. *K*-shell x-ray pinhole photographs (top) and spatially resolved *K*-line spectra (bottom) for neon implosions without and with the PEOS. The cathode nozzle is on the left and the wire mesh anode is on the right.

match the higher order line ratios ($Ly-\alpha/Ly-\beta$, $He-\alpha/He-\beta$, etc.). This inconsistency is not presently understood and is under investigation. The $Ly-\alpha$ and $He-\alpha$ lines are dominant, with $\sim 90\%$ of the total radiated line energy, making this plasma a nearly monochromatic intense x-ray source near 1 keV. Based on the axially averaged $Ly-\alpha/He-\alpha$ ratios we estimate a plasma temperature of 150 eV without the PEOS and 185 eV with the PEOS. These numbers are consistent with loadings of 34 and 29 $\mu\text{g}/\text{cm}$, respectively, and a 1.8-mm-diam radiating core for both. We conclude that both a hotter and longer radiating plasma contribute to the observed increase in *K*-shell radiation with the PEOS.

In summary, neon gas puffs driven with 1.25 MA from the NRL Gamble II generator emit more than 70% of the total radiated energy in the *K* shell. This yield scales as the fourth power of the current with ~ 4 kJ being radiated at optimized mass and 1.45 MA of current. For a given peak current, the *K* shell yield can be increased by as much as 2.5

by reducing the current rise time with a PEOS. Use of a PEOS also improves pinch quality in the radial direction and its axial uniformity. We speculate that the elimination of the early part of the current with the PEOS, limits the growth time of instabilities resulting in a more orderly collapse of the cylindrical plasma on axis.

We must acknowledge S. L. Wong, P. Sincerny, and T. Sheridan of Physics International Co. for the design, building, and installation of a working gas-puff system for Gamble II. R. Spielman and R. R. Williams of Sandia Labs were instrumental in fielding and interpreting the bolometer data. D. J. Nagel of NRL was instrumental in fielding the spectroscopic diagnostics. We express appreciation to J. R. Bolter, P. Kepple, and R. F. Terry of NRL for many useful discussions. Finally the technician crew of J. W. Snider, J. Miller, A. Robinson, and J. Negri are acknowledged for their assistance in fielding the experiments. This work was supported by the Defense Nuclear Agency.

¹S. J. Stephanakis, L. S. Levine, D. Mosher, I. M. Vitkovitsky, and F. C. Young, *Phys. Rev. Lett.* **29**, 568 (1972); F. C. Young, S. J. Stephanakis, I. M. Vitkovitsky, and D. Mosher, *IEEE Trans. Nucl. Sci.* **NS-20**, 439 (1973); D. Mosher, S. J. Stephanakis, I. M. Vitkovitsky, C. M. Dozier, L. S. Levine, and D. J. Nagel, *Appl. Phys. Lett.* **23**, 419 (1973).

²C. Stallings, K. Nielson, and R. Schneider, *Appl. Phys. Lett.* **29**, 404 (1976); P. G. Burkhalter, J. Davis, J. Rauch, W. Clark, G. Dahlbacka, and R. Schneider, *J. Appl. Phys.* **50**, 705 (1979); W. Clark, M. Gersten, J. Katzenstein, J. Rauch, R. Richardson, and M. Wilkinson, *J. Appl. Phys.* **53**, 4099 (1982).

³J. Shiloh, A. Fisher, and N. Rostoker, *Phys. Rev. Lett.* **40**, 515 (1978); C. Stallings, K. Childers, I. Roth, and R. Schneider, *Appl. Phys. Lett.* **35**, 524 (1979); W. Clark, R. Richardson, J. Brannon, M. Wilkinson, and J. Katzenstein, *J. Appl. Phys.* **53**, 5552 (1982); R. E. Marrs, D. D. Dietrich, R. J. Fortner, M. A. Levine, D. F. Price, R. F. Steward, and B. K. F. Young, *Appl. Phys. Lett.* **42**, 946 (1983); C. D. Challis, A. E. Dangor, E. S. Wyndham, D. Mosher, W. G. Beasell, and D. J. Bond, in *Proc. 11th European Conf. Controlled Fusion and Plasma Physics*, Aachen, Federal Republic of Germany, 1983; D. R. Kania and L. A. Jones, *Phys. Rev. Lett.* **53**, 166 (1984); S. Maxon and T. Wainwright, *Phys. Fluids* **27**, 2535 (1984); R. B. Spielman, D. L. Hanson, M. A. Palmer, M. K. Matzen, T. W. Hussey, and J. M. Peek, *J. Appl. Phys.* **57**, 830 (1985).

⁴R. A. Meger, R. J. Comisso, G. Cooperstein, and Shyke A. Goldstein, *Appl. Phys. Lett.* **42**, 943 (1983); P. F. Ottinger, S. A. Goldstein, and R. A. Meger, *J. Appl. Phys.* **56**, 774 (1984).

⁵R. S. Smith, W. O. Doggett, I. Roth, and C. Stallings, *Appl. Phys. Lett.* **41**, 572 (1982); G. Dahlbacka, R. Dukart, R. Fortner, D. Dietrich, and R. Stewart, in *Record, 1983 IEEE Inter. Conf. Plasma Sci.*, Ottawa, 1983, p. 39.

⁶D. L. Hanson, R. B. Spielman, and J. P. Anthes, *Bull. Am. Phys. Soc.* **26**, 910 (1981).

⁷J. U. Guillory and R. E. Terry, JAYCOR Report No. J800-83-003, 1984 (unpublished); J. P. Apruzese and J. Davis, NRL Memorandum Report No. 5406, 1984 (unpublished); S. W. McDonald, P. F. Ottinger, R. E. Terry, and S. J. Stephanakis, *Bull. Am. Phys. Soc.* **29**, 1329 (1984).

⁸S. Wong, C. Gilman, P. Sincerny, and T. Young, in *Record 1982 IEEE Inter. Conf. Plasma Sci.*, Ottawa, 1982, p. 37.

⁹P. G. Burkhalter, J. Shiloh, A. Fisher, and R. D. Cowan, *J. Appl. Phys.* **50**, 4532 (1979).

¹⁰J. P. Apruzese, P. C. Kepple, K. G. Whitney, J. Davis, and D. Duston, *Phys. Rev. A* **24**, 1001 (1981).

DISTRIBUTION LIST

Assistant to the Secretary of Defense Atomic Energy Washington, D.C. 20301 ATTN: Executive Assistant	1 Copy
Director Defense Intelligence Agency Washington, D.C. 20301 ATTN: DT-1B R. Rubenstein	1 Copy
Director Defense Nuclear Agency Washington, D.C. 20305 ATTN: DDST ATTN: TITL ATTN: RAEV ATTN: STVI	1 copy 4 copies 1 copy 1 copy
Commander Field Command Defense Nuclear Agency Kirtland AFB, New Mexico 87115 ATTN: FCPR	1 Copy
Chief Field Command Livermore Division Department of Defense P.O. Box 808 Livermore, CA 94550 ATTN: FCPRL	1 Copy
Director Joint Strat TGT Planning Staff Offutt AFB Omaha, Nebraska 68113 ATTN: JLKS	1 Copy
Undersecretary of Defense for RSCH and ENGRG Department of Defense Washington, D.C. 20301 ATTN: Strategic and Space Systems (OS)	1 Copy
Deputy Chief of Staff for RSCH DEV and ACQ Department of the Army Washington, D.C. 20301 ATTN: DAMA-CSS-N	1 Copy

Commander
Harry Diamond Laboratories
Department of the Army
2800 Powder Mill Road
Adelphi, MD 20783
ATTN: DELHD-N-NP
ATTN: DELHD-R J. Rosado
ATTN: DELHD-TA-L (Tech. Lib.)

1 copy each

U.S. Army Missile Command
Redstone Scientific Information Center
Attn: DRSMI-RPRD (Documents)
Redstone Arsenal, Alabama 35809

3 Copies

Commander
U.S. Army Missile Command
Redstone Arsenal, Alabama 35898
ATTN: DRCPM-PE-EA

1 copy

Commander
U.S. Army Nuclear and Chemical Agency
7500 Backlick Road
Building 2073
Springfield, VA 22150
ATTN: Library

1 copy

Commander
Naval Intelligence Support Center
4301 Suitland Road, Bldg. 5
Washington, D.C. 20390
ATTN: NISC-45

1 Copy

Commander
Naval Weapons Center
China Lake, California 93555
ATTN: Code 233 (Tech. Lib.)

1 Copy

Officer in Charge
White Oak Laboratory
Naval Surface Weapons Center
Silver Spring, Md. 20910
ATTN: Code R40
ATTN: Code F31

1 Copy each

Air Force Weapons Laboratory
Kirtland AFB, New Mexico 87117
ATTN: SUL
ATTN: CA
ATTN: APL
ATTN: Lt. Col Generosa

1 Copy each

Deputy Chief of Staff Research, Development and Accounting Department of the Air Force Washington, D. C. 20330 ATTN: AFRDQSM	1 Copy
Commander U.S. Army Test and Evaluation Command Aberdeen Proving Ground, MD 21005 ATTN: DRSTE-EL	1 Copy
AVCO Research and Systems Group 201 Lowell Street Wilmington, MA 01887 ATTN: Library A830	1 Copy
BDM Corporation 7915 Jones Branch Drive McLean, Virginia 22101 ATTN: Corporate Library	1 Copy
Berkeley Research Associates P.O. Box 983 Berkeley, CA 94701 ATTN: Dr. Joseph Workman	1 Copy
Berkeley Research Associates P.O. Box 852 5532 Hempstead Way Springfield, VA 22151 ATTN: Dr. Joseph Orens	1 Copy each
Boeing Company P. O. Box 3707 Seattle, WA 98134 ATTN: Aerospace Library	1 Copy
The Dikewood Corporation 1613 University Bldv., N.E. Albuquerque, New Mexico 87110 ATTN: L. Wayne Davis	1 Copy
General Electric Company Space Division Valley Forge Space Center P. O. Box 8555 Philadelphia, PA 19101 ATTN: J. Peden	1 Copy
General Electric Company - Tempo Center for Advanced Studies 816 State Street P.O. Drawer QQ Santa Barbara, CA 93102 ATTN: DASIAC	1 Copy

Institute for Defense Analyses 1801 N. Beauregard St. Alexandria, VA 22311 ATTN: Classified Library	1 Copy
IRT Corporation P.O. Box 81087 San Diego, CA 92138 ATTN: Dr. W. Dennis Swift Dr. Jaco Wilkenfeld	1 Copy each
JAYCOR 11011 Forreyane Rd. P.O. Box 85154 San Diego, CA 92138 ATTN: E. Wenaas F. Felbar	1 Copy
JAYCOR 205 S. Whiting Street, Suite 500 Alexandria, VA 22304 ATTN: R. Sullivan	1 Copy
KAMAN Sciences Corp. P. O. Box 7463 Colorado Springs, CO 80933 ATTN: Library	1 copy each
Lawrence Livermore National Laboratory University of California P.O. Box 808 Livermore, California 94550 ATTN: DOC CDN for L-153 DOC CDN for L-47 L. Wouters DOC CDN for Tech. Infor. Dept. Lib.	1 copy
Lockheed Missiles and Space Co., Inc. P. O. Box 504 Sunnyvale, CA 94086 Attn: S. Taimlty Attn: J.D. Weisner	1 copy each
Lockheed Missiles and Space Co., Inc. 3251 Hanover Street Palo Alto, CA 94304 Attn: J. Perez	1 Copy
Maxwell Laboratory, Inc. 9244 Balboa Avenue San Diego, CA 92123 ATTN: A. Kolb ATTN: M. Montgomery ATTN: J. Shannon	1 Copy each

McDonnell Douglas Corp. 5301 Bolsa Avenue Huntington Beach, CA 92647 ATTN: S. Schneider	1 Copy
Mission Research Corp. P. O. Drawer 719 Santa Barbara, CA 93102 ATTN: C. Longmire ATTN: W. Hart	1 Copy each
Mission Research Corp.-San Diego 5434 Ruffin Rd. San Diego, California 92123 ATTN: Victor J. Van Lint	1 Copy
Northrop Corporation Northrop Research and Technology Center 1 Research Park Palos Verdes Peninsula, CA 90274 ATTN: Library	1 Copy
Physics International Company 2700 Merced Street San Leandro, CA 94577 ATTN: M. Krishnan ATTN: C. Gilman ATTN: S. Wong	1 Copy each
R and D Associates P.O. Box 9695 Marina Del Rey, CA 90291 ATTN: W. Graham, Jr. ATTN: P. Haas	1 Copy each
Sandia National Laboratories P.O. box 5800 Albuquerque, New Mexico 87115 ATTN: DOC CON FOR 3141 ATTN: D. MCDANIEL	1 copy each
Science Applications, Inc. P. O. Box 2351 La Jolla, CA 92038 ATTN: R. Beyster	1 copy
Spectra Technol, Inc., Attn: Alan Hoffman 2755 Northup Way Bellevue, Washington 98004	1 copy
Spire Corporation P. O. Box D Bedford, MA 01730 ATTN: R. Little	1 copy

SRI International 333 Ravenswood Avenue Menlo Park, CA 94025 ATTN: S. Dairiki	1 copy
S-CUBED P. O. Box 1620 La Jolla, CA 92038 ATTN: A. Wilson	1 copy
Director Strategic Defense Initiative Organization 1717 H Street Pentagon 20301-7100 ATTN: DE Lt. Col Richard Gullickson/DEO IST Dr. Dwight Duston ATTN: IST Dr. J. Ionson	1 copy each
Texas Tech University P.O. Box 5404 North College Station Lubbock, TX 79417 ATTN: T. Simpson	1 copy
TRW Defense and Space Systems Group One Space Park Redondo Beach, CA 90278 ATTN: Technical Information Center	1 Copy
University of Buffalo Attn: Professor W. J. Sarjeant Dept. of Electrical Engineering High Voltage and Power 312 Bonner Hall Buffalo, New York 14260	1 Copy
Naval Research Laboratory Plasma Radiation Branch Washington, D.C. 20375	50 copies
Code 4700 Code 2628 Code 1220 Records	26 copies 22 copies 1 copy 1 copy
Director of Research U.S. Naval Academy Annapolis, MD 21402	2 copies

END

10-87

DTIC